



Development of cooling systems for nuclear fusion components

Ricardo Tavares Rego

Thesis to obtain the Master of Science Degree in

Mechanical Engineering

Supervisors: Dr. Hugo Filipe Diniz Policarpo

Eng. Paulo Ricardo Braga Moniz Quental

Examination Committee

Chairperson: Prof. Carlos Frederico Neves Bettencourt da Silva

Supervisor: Dr. Hugo Filipe Diniz Policarpo

Member of the Committee: Prof. Viriato Sérgio de Almeida Semião

November 2017

Agradecimentos

Quero expressar os meus sinceros agradecimentos:

Aos meus orientadores, Hugo Filipe Diniz Policarpo e Paulo Ricardo Braga Moniz Quental pela orientação, disponibilidade, auxílio e incentivo prestado durante a elaboração desta dissertação.

Aos membros do IPFN, mais especificamente ao Ricardo Ferreira, ao Ruben Moutinho, à Barbara Pereira e ao Nicolau Velez, por todo os dados técnicos providenciados e conhecimento partilhado.

Aos meus pais por todo o apoio emocional e financeiro, ao meu primo Daniel Rego Oliveira por viver esta aventura em Lisboa comigo, aos meus irmãos Rodrigo e Miguel, ao Gonçalo Feio, ao Filipe Andrade, ao Eduardo Araújo, ao Ricardo Maia, à Catarina Cordeiro e a todos os meus outros amigos e colegas que foram importantes durante este processo e contribuíram e tornaram este trabalho possível.

A todos os meus professores que partilharam o seu conhecimento e ajudaram-me a desenvolver um pensamento ágil e inteligente, merecendo reconhecimento o Professor Luís Pedro Pereira Marques Paz, o Professor Nuno Sá, o Professor Viriato Sérgio Almeida Semião e o Professor José Manuel da Silva Chaves Ribeiro Pereira. Um especial agradecimento a estes dois últimos, Professor Viriato Sérgio Almeida Semião e o Professor José Manuel da Silva Chaves Ribeiro Pereira, que estiveram sempre disponíveis para me ajudarem nesta dissertação.

Acknowledgments

I want to express my sincere acknowledgments:

To my supervisors, Hugo Filipe Diniz Policarpo and Paulo Ricardo Braga Moniz Quental for the orientation, availability, support and incentive provided during this dissertation.

To all the IPFN staff and more specifically to Ricardo Ferreira, Ruben Moutinho, Bárbara Pereira and Nicolau Velez for all the technical data provided and knowledge transmitted.

To my parents for all the emotional and financial support, my cousin Daniel Rego Oliveira for living this adventure in Lisbon with me, to my brothers Rodrigo and Miguel, to Gonçalo Feio, to Filipe Andrade, to Eduardo Araújo, to Ricardo Maia, to Catarina Cordeiro and to all my other friends and colleagues whom were important during this process and contributed to making this work possible.

To all the professors that shared their knowledge and helped me develop an agile and intelligent thinking, deserving mention Professor Luís Pedro Pereira Marques Paz, Professor Nuno Sá, Professor Viriato Sérgio Almeida Semião and Professor José Manuel da Silva Chaves Ribeiro Pereira. A special acknowledgment to the last two, Professor Viriato Sérgio Almeida Semião and Professor José Manuel da Silva Chaves Ribeiro Pereira, that were always available to help me in this dissertation.

Resumo

Esta dissertação apresenta um estudo sobre o desenvolvimento de um sistema de arrefecimento para os espelhos de emissão e receção presentes no sistema de diagnóstico do sistema Collective Thomson Scattering (CTS) do International Thermonuclear Experimental Reactor (ITER).

Este estudo é motivado pelo facto destes espelhos, feitos de aço inoxidável 316L(N)-IG, estarem sujeitos a cargas térmicas elevadas ficando os espelhos com uma temperatura máxima superior à temperatura de operação do material (450°C). Consequentemente, é necessário o desenvolvimento de um sistema de arrefecimento capaz de manter os espelhos a temperaturas inferiores à mencionada e que cumpra com os requisitos nucleares do ITER.

Para tal, nesta dissertação, são desenvolvidos modelos de Desenho Assistido por Computador (CAD) dos espelhos com diferentes geometrias de canais de arrefecimento. Para além do aço mencionado, tungsténio e cobre são também considerados como possíveis materiais para os espelhos. São realizadas análises térmicas em elementos finitos (FEA) nos regimes estacionário e transiente.

Os resultados obtidos são conclusivos, i.e., é verificado que é necessário um sistema de arrefecimento e com uma das geometrias propostas é possível baixar as temperaturas dos espelhos de aço 316L(N)-IG em aproximadamente 80% ficando os espelhos na gama de temperatura de operação.

Palavras chave: ITER, Sistema CTS, Fusão Nuclear, Elementos Finitos, Análise Térmica

Abstract

This dissertation presents a study on the development of a cooling system for the launcher and receiver mirrors of the International Thermonuclear Experimental Reactor (ITER) Collective Thomson Scattering (CTS) system that is used for plasma diagnostics.

It is motivated by the fact that these stainless steel 316L(N)-IG mirrors are subjected to high thermal loads that lead to maximum temperatures of the mirrors above the required operational temperature 450°C . Hence, it is necessary to develop a cooling system capable of maintaining the temperatures of the mirrors below 450°C , while complying with the CTS and nuclear fusion requirements.

For it, in this dissertation, Computer Aided Design (CAD) models of the mirrors with different cooling channel geometries are developed. Besides stainless steel 316L(N)-IG, tungsten and copper are also considered for the mirrors. Steady state and transient thermal Finite Element Analysis (FEA) are conducted for the assessment of the feasible solutions.

The results obtained are conclusive, i.e., cooling requirement is verified and with one of the proposed configurations it is possible to lower the maximum temperatures of the 316L(N)-IG mirrors by approximately $\sim 83.5\%$ putting it in the operating temperature range.

Keywords: ITER, CTS System, Nuclear Fusion, Finite Elements, Thermal Analysis

Table of Contents

Agradecimientos	i
Acknowledgments	ii
Resumo	iii
Abstract	iv
List of Figures.....	viii
List of Tables.....	xi
Publications	xiii
Nomenclature.....	xiv
1. Introduction.....	1
1.1. Nuclear Fusion.....	1
1.2. Diagnostics Systems	4
1.3. Mechanical Engineering Framework.....	7
1.3.1. Brief Heat Transfer Background	7
1.3.2. Brief Fluid Mechanics Background	8
1.4. Problem statement.....	8
2. Fundamentals.....	11
2.1. Heat Transfer.....	11
2.1.1. Conduction	11
2.1.2. Convection.....	13
2.1.3. Radiation	15
2.1.4. Internal Heat Generation	20
2.2. Finite Elements Method	21
2.2.1. FEM Applied to Heat Transfer	22
2.2.2. Finite Elements in ANSYS®	24
2.3. Fluid Flow	26
2.3.1. Governing Equations	26
2.3.2. Turbulence Models.....	27
2.3.3. Pressure Drop in Channels	30
3. Methodology.....	31
3.1. Verification Models	31
3.1.1. Convection Model	31
3.1.1. Thermal Radiation Model.....	31
3.2. Launcher Mirror	32
3.2.1. Microwaves Radiation Beam Power Distribution	32

3.2.2.	CAD Model Design.....	33
3.2.3.	Steady State Thermal FEA	34
3.2.3.1.	Mesh Convergence.....	34
3.2.3.2.	Mirror Made of SS 316 L(N)-IG.....	35
3.2.3.3.	Other Materials Considered for the Mirror.....	37
3.2.4.	Transient Thermal FEA	38
3.3.	Receiver Mirror	39
3.4.	Steady State Fluid Flow Thermal Analysis.....	39
4.	Results and Discussions.....	41
4.1.	Verification Models	41
4.1.1.	Convection Model	41
4.1.2.	Thermal Radiation Model.....	42
4.2.	Launcher Mirror	44
4.2.1.	Microwaves Radiation Beam Power Distribution	44
4.2.2.	Steady State Thermal FEA	45
4.2.2.1.	FE Mesh Convergence	46
4.2.2.2.	Pressure Drop.....	47
4.2.2.3.	Mirror Made of SS 316 L(N)-IG.....	47
4.2.2.4.	Other Materials Considered for the Mirror.....	55
4.2.3.	Transient Thermal FEA	58
4.3.	Receiver Mirror	60
4.3.1.	Mesh Convergence.....	61
4.3.2.	Pressure Drop.....	62
4.3.3.	Steady State Thermal FEA	63
4.3.4.	Transient Thermal FEA	65
4.4.	Steady State Fluid Flow Thermal Analysis.....	68
5.	Conclusions and Future Works.....	72
	References.....	74
	Appendixes.....	77
A.1.	MATLAB® Routine A1	77
A.2.	Data for Microwave Power Absorbed Fraction Calculation.....	78
A.3.	SS316 L(N)-IG Properties	79
A.4.	Copper Properties	80
A.5.	Tungsten Properties	81
A.6.	Launcher cooling channel geometries	82
A.7.	Receiver cooling channel geometries	83

A.8.	SS316 L(N)-IG Launcher Mirror Results	84
A.9.	Copper Launcher Mirror Results	87
A.10.	Tungsten Launcher Mirror Results	90
A.11.	SS316 L(N)-IG Receiver Mirror Results	93

List of Figures

Figure 1 - Primary energy sources (2014), being “others” geothermal, wind, etc. [2].	2
Figure 2 - Deuterium and tritium fusion reaction [4].	2
Figure 3 - Operation principle and main constituents of a tokamak [4].	3
Figure 4 - Divertor localization in the tokamak.	5
Figure 5 - Beam scattering geometry. Left figure taken from [11] and right figure from [9].	5
Figure 6 - ECE schematic representation [11].	6
Figure 7 - ITER CTS [9].	6
Figure 8 - ITER CTS system configurations: (left) old; (right) actual. Mirror 1 is related to the incident beam and mirror 2 to the scattering radiation.	7
Figure 9 - Laminar flow boundary layer development in a circular tube [14].	14
Figure 10 - Thermal boundary layer development in a circular cross-section tube [14].	15
Figure 11 - View factor between the element dA_i and dA_j [14].	18
Figure 12 - View factor for parallel rectangular plates [14].	18
Figure 13 - Electric analogue representation for a heat transfer radiation problem [14].	19
Figure 14 - Hemicube method geometric representation [18].	20
Figure 15 - Outline of a FEA implementation, [21].	22
Figure 16 - SOLID90 element geometry [23].	24
Figure 17 - SHELL131 element geometry [23].	25
Figure 18 - SURF152 element geometry [23].	25
Figure 19 - SURF252 element geometry [23].	25
Figure 20 - FLUID116 element geometry [23].	26
Figure 21 - CAD model of a parallelepiped of length L with center hole of diameter D .	31
Figure 22 - CAD model of two irradiating surfaces considered for the radiation problem.	32
Figure 23 - Input data panel for the isolines estimation.	32
Figure 24 - Some steps used in the CAD modeling of a cooling channel.	33
Figure 25 - CAD models of the launcher mirror and enclosure.	34
Figure 26 - CAD model of the launcher mirror without cooling channels.	34
Figure 27 - CAD model and localization of the radiation surface (in red) used to model the plasma radiation and stray radiation emission.	35
Figure 28 - Emissivity as a function of the temperature for unpolished (Blankets) and polished (Antenna) components made of SS 316L(N)-IG [30].	36
Figure 29 - Step controls for the transient FEA in ANSYS®Mechanical.	38
Figure 30 - CAD model and localization of the receiver mirror and of the surface (in red) used to model the plasma radiation and stray radiation emission.	39
Figure 31 - Numerical results for the heat transfer by convection verification model: left) the tube bore surface temperature distribution and; right) the fluid temperature distribution. Temperature in °C.	42
Figure 32 - Second verification model mesh, in ANSYS®MODEL.	43
Figure 33 - MATLAB® user input interface to estimate the microwave radiation power distribution in the mirror.	44

Figure 34 - Isolines representation in 2D and 3D.....	44
Figure 35 - Surface defined by equation (40).....	45
Figure 36 - Values of parameters "a" and "b" that define the representative ellipses isolines and the value of the power (beam intensity) between each isoline.....	45
Figure 37 - FE mesh refinement for the cooling channel geometry 7_D_14MM.	46
Figure 38 - FE mesh convergence result for the cooling channel geometry 7_D_14MM.	46
Figure 39 - Convective coefficient for the different cooling channel geometries and total mass flow rates considered.	50
Figure 40 - Convection area A_c and water volume V_{water} values for the cooling channel geometries.	51
Figure 41 - Maximum mirror temperature vs total mass flow rate used for SPIRAL_D_10MM and SPIRAL_D_14MM.	52
Figure 42 - Maximum mirror temperature vs total mass flow rate used for ZIGZAG_D_10MM, ZIGZAG_D_10MM_CURTO and ZIGZAG_D_14MM.	52
Figure 43 - Maximum mirror temperature vs total mass flow rate used for 7_D_14MM, 7_14x14 and 13_14x5.....	53
Figure 44 - Maximum mirror temperature vs total mass flow rate used for 1_RETAN_120x10 and 1_RETAN_120x14.....	54
Figure 45 - Maximum mirror temperature vs total mass flow rate used for 1_RETAN_120x14, ZIZAG_D_14MM and 7_14x14.	54
Figure 46 - Temperature distribution for cooling channel geometry SPIRAL_D_14MM with a mass flow rate of 1.5 Kg/s, element size of 0.0025 mm and copper as the mirror material: left) temperature of the mirror and; right) temperature of the reflective surface of the mirror.....	55
Figure 47 - Maximum reflective mirror surface temperature vs total used mass flow rate for copper. .	56
Figure 48 - Maximum reflective mirror surface temperature vs total used mass flow rate for tungsten.	56
Figure 49 - Thermal diffusivity vs temperature for SS316L(N)-IG, Tungsten and Copper.....	57
Figure 50 - Maximum surface temperature vs the total mass flow rate for ZIGZAG_D_10MM, ZIGZGA_D_10MM_CURTO and 13_14x5 for Tungsten.	57
Figure 51 - Representation, for the transient thermal FE analysis, of internal heat generation, microwave beam power (1054.6 W).....	58
Figure 52 - Representation, for the transient thermal analysis, of the boundary conditions used to model the plasma.	58
Figure 53 - Maximum mirror temperature considering a mass flow rate of 1.5 Kg/s (in series) with flow on during the dwell time phase.....	59
Figure 54 - Maximum mirror temperature considering a mass flow rate of 1.5 Kg/s (in series) with flow off during the dwell time phase.....	59
Figure 55 - Maximum mirror temperature considering a mass flow rate of 0.25 Kg/s (in parallel) with flow on during the dwell time.....	60

Figure 56 - Maximum mirror temperature considering a mass flow rate of 0.25 Kg/s (in parallel) with flow off during the dwell time.....	60
Figure 57 - Mesh convergence of the maximum temperature for channel 1_RETAN_240x14.	61
Figure 58 - Graphical representation of the convection coefficient for each channel geometry.	64
Figure 59 - Graphical representation of the convection area and the water volume for each channel geometry.....	64
Figure 60 - Maximum mirror temperature vs total mass flow rate for different channel geometries.	65
Figure 61 - Maximum mirror temperature considering a mass flow rate of 1.5 Kg/s with flow on during the dwell time.....	66
Figure 62 - Maximum mirror temperature considering a mass flow rate of 1.5 Kg/s with flow off during the dwell time phase.	66
Figure 63 - Maximum mirror temperature considering a mass flow rate of 0.25 Kg/s with flow off during the dwell time.....	67
Figure 64 - Maximum mirror temperature considering a mass flow rate of 0.25 Kg/s with flow off during the dwell time phase.	67
Figure 65 - Launcher mirror1_RETAN_120x14 cooling channel geometry: a) Local convection coefficient and; b) Pressure values.	69
Figure 66 - Receiver mirror with 1_RETAN_240x14 cooling channel geometry: a) Local convection coefficient and; b) Pressure values.	70
Figure 67 - Launcher mirror cooling channel geometries: a) SPIRAL_D_10MM; b) SPIRAL_D_14MM; c) ZIGZAG_D_10MM; d) ZIGZAG_D_10MM_CURTO; e) ZIGZAG_D_14MM; f) 7_D_14MM; g) 7_14X14; h) 13_14X5; i) 1_RETAN_120X10 and; j) 1_RETAN_120X14.	82
Figure 68 - Receiver mirror cooling channel geometries: a) ZIGZAG_D_10MM; b) ZIGZAG_D_14MM; c) 13_14X5 and; d) 1_RETAN_240X14.	83

List of Tables

Table 1 - Tokamaks in operation [1].	3
Table 2 - Boundary conditions for the heat diffusion equation on a surface ($x=0$), [14].	12
Table 3 - CAD models of the launcher mirror with different cooling channel geometries.	36
Table 4 - Input data used for the heat transfer by convection verification model.	41
Table 5 - Input data used for the heat transfer by thermal radiation verification model.	42
Table 6 - Analytical results for the heat transfer by thermal radiation verification model.	43
Table 7 - Numerical results (ANSYS®) for the heat transfer by thermal radiation verification model.	43
Table 8 - Deviation between analytical and ANSYS® results for the heat transfer by thermal radiation verification model.	43
Table 9 - Pressure drop results for ZIGZAG_D_10MM.	47
Table 10 - Implementation of the heat flux and stray radiation from plasma.	48
Table 11 - T_{max} [°C] results for the launcher mirror achieved with different combinations of thermal loads.	49
Table 12 - Convective coefficient for different cooling channel geometries and mass flow rates.	49
Table 13 - Water properties for $T=77.5$ [°C].	50
Table 14 - Values of Ac and V_{water} for each cooling channel geometry.	51
Table 15 - Chosen cooling channel geometries, respective areas, and water volume.	61
Table 16 - Pressure drop for cooling channel geometry ZIGZAG_D_10MM.	62
Table 17 - Pressure drop for cooling channel geometry ZIGZAG_D_14MM.	62
Table 18 - Convective coefficient for the different cooling channel geometries and mass flow rates.	63
Table 19 - Outgoing net radiation from the launcher and receiver mirrors surfaces.	68
Table 20 - Analytical results and FLUENT results for the ZIGZAG_D_10MM and 1_RETAN_120x14, launcher mirror.	69
Table 21 - Analytical results and FLUENT results for the ZIGZAG_D_14MM and 1_RETAN_240x14, receiver mirror.	70
Table 22 - Data for equation (41).	78
Table 23 - Electrical Resistivity for SS316L(N)-IG.	78
Table 24- Electrical Resistivity for tungsten.	78
Table 25 - Electrical Resistivity for copper.	78
Table 26 - Values of thermal conductivity, specific heat, density and thermal conductivity and diffusivity from room temperature to 800 °C for type 316L(N)-IG stainless steel.	79
Table 27 - Values of thermal conductivity, specific heat, density and thermal conductivity and diffusivity from room temperature to 800 °C for pure copper.	80
Table 28 - Values of thermal conductivity, specific heat, density and thermal conductivity and diffusivity from room temperature to 800 °C for tungsten.	81
Table 29 - Emissivity values for tungsten.	81
Table 30 - Mesh convergence for SS316L(N)-IG.	84
Table 31- Flow variation results for SS316L(N)-IG.	85

Table 32- Flow variation results for SS316L(N)-IG (continuation).	86
Table 33 - Mesh convergence for copper.....	87
Table 34 - Flow variation results for copper.	88
Table 35 - Flow variation results for copper (continuation).	89
Table 36 - Mesh convergence for tungsten.....	90
Table 37 - Flow variation results for tungsten.	91
Table 38 - Flow variation results for tungsten (continuation).	92
Table 39 - Convergence and Flow Variation results for SS316 L(N)-IG receiver mirror.....	93

Publications

In the following are listed the publications of the author, in scientific journals and conference proceedings that are directly related with the research work developed in this dissertation.

Scientific journals

➤ 2017

- Rego R., Quental P.B., Policarpo H. and Moutinho R., Preliminary Design of Cooling Systems for the Launcher and Receiver Mirrors of the ITER LFS-CTS diagnostic, Fusion Engineering and Design, 2017.

Conference Proceedings

➤ 2017

- Ferreira R., Pereira B., Rego R., Gonçalves B., and Korsholm S. B., Thermal structural analysis of ITER's Collective Thomson Scattering, International Conference on Structural Integrity, Funchal, Portugal, September 4-7 (2017).

Nomenclature

<i>CAD</i>	Computer Aided Design
<i>CFD</i>	Computational Fluid Dynamics
<i>CTS</i>	Collective Thomson Scattering
<i>DNS</i>	Direct Numerical Simulation
<i>FDM</i>	Finite Difference Method
<i>FE</i>	Finite Elements
<i>FEA</i>	Finite Element Analysis
<i>FEM</i>	Finite Element Method
<i>IPFN</i>	Instituto de Plasmas e Fusão Nuclear
<i>ITER</i>	International Thermonuclear Experimental Reactor
<i>LFS-CTS</i>	Low Field Side Collective Thomson Scattering
<i>MCNP</i>	Monte Carlo N-Particle Code
<i>SIMPLE</i>	Semi-Implicit Method for Pressure Linked Equations
SS 316L(N)-IG	Stainless Steel 316L(N)-IG

Greek symbols

α	Thermal diffusivity
α_{abs}	Absorbance
Δ	Variation of a parameter
ε	Emissivity
ε_{diss}	Dissipation ratio
θ_i, θ_j	Angles between the surfaces normal vectors and the dashed line uniting the areas centroids in view factor
λ	Wavelength
μ	Fluid viscosity
μ_0	Space permeability
μ_{eff}	Effective viscosity
μ_t	Turbulent viscosity or Eddy viscosity

ν_t	Turbulent kinematic viscosity
ρ	Density
ρ_a	Atomic density
ρ_{ref}	Reflectivity
ρ_{res}	Electrical resistivity
σ	Stefan-Boltzmann constant
τ	Transmissivity
$\bar{\tau}$	Stress tensor
τ_0	Wall friction
φ	Particle flow

Roman symbols

A	Area
A_{abs}	Power absorbed
A_i, A_j	Area of element i or j
c_p	Specific heat at constant pressure
D	Diameter
D_h	Characteristic hydraulic diameter
E	Emissive power
E_b	Emissive power of a blackbody
E_{par}	Particle energy
E_{tot}	Total energy
f	Darcy coefficient
f_{Hz}	Gyrotron frequency
F_{ij}, F_{ji}	View factors between surfaces i and j
g	Gravitational acceleration
G	Irradiation
h	Convection coefficient

h_{en}	Sensible enthalpy
h_f	Head loss
h_{tot}	Total losses
$H(E_{par})$	Heating response
H_{conv}	Global convection
H_{rad}	Global radiation
$I_{\lambda,e}$	Radiation spectral intensity
J	Radiosity
J_i, J_j	Radiosity of elements i and j
k	Thermal conductivity
k^i	Incident radiation wave
k^s	Scattered radiation wave
k^δ	Wave fluctuation vector
k_{eff}	Effective conductivity
k_{sw}	Big swirls kinetic energy
k_t	Conductivity due to turbulent transport
K_i	Local loss coefficient for elbows, bends, etc.
K_T	Global thermal conductivity
l_m	Characteristic length of the turbulent field
L	Tube length
\dot{m}	Mass flow rate
n_x, n_y, n_z	Uni vectors of the axes x, y, z
N_i	Global shape function
Nu_D	Nusselt number for internal flows
p	Static pressure
p_1, p_2	Static pressure at point 1 and 2
P	Perimeter

P_{beam}	Beam power
Pr	Prandtl number
q	Power (heat per unit of time)
q''	Heat flux
\dot{q}	Internal heat generation
R	Thermal resistance
R_{ij}	Direct length between the centroid points of two surfaces
Re_D	Reynolds number for internal flows
$Re_{D,c}$	Reynolds critical number for internal flows
t	Time
T	Temperature
T_∞	Temperature of the evolving medium
T_1, T_2	Temperature of element 1 and 2
T_m	Mean temperature
T_{mi}, T_{mo}	Mean inlet and outlet temperature
T_{ref}	Reference temperature
T_s	Surface temperature
T_{sur}	Surroundings temperature
u_m	Mean flow velocity
u_i	Instantaneous velocity
\bar{u}_i	Mean instantaneous velocity
u'_i	Velocity fluctuations
v_1, v_2	Flow velocity at points 1 and 2
v_t	Characteristic velocity of the turbulent field
V	Volume
$x_{fd,h}$	Hydrodynamic entry region length
$x_{fd,t}$	Thermal entry region length

z_1, z_2 Height of point 1 and 2

Z_0 Space impedance

Subscripts

i, j, k Computational indexes

n Normal component

x, y, z Cartesian components

1. Introduction

This dissertation presents a study on the development of a cooling system for the launcher and receiver mirrors of the ITER CTS system that is used for plasma diagnostics.

This work is motivated by the fact that these stainless steel 316L(N)-IG (SS 316L(N)-IG) mirrors, which are in a vacuum environment and subjected to thermal loads that arise from: direct plasma thermal radiation; neutron fluxes from the nuclear fusion reaction; stray radiation from the surroundings and; the microwave launcher and receiver beams, do not survive operation as the maximum temperatures exceed the operational temperature $\sim 450^{\circ}\text{C}$.

Hence, it is necessary to develop a cooling system that is capable of maintaining the temperatures of the mirrors at an operational temperature $< 450^{\circ}\text{C}$ while complying with the CTS system requirements, e.g., inlet cooling fluid pressure (water), and nuclear fusion requirements.

The first part of this study consists of the development of the CAD models of the two mirrors and for each mirror are developed different cooling channel geometries.

The second part of this study consists on the FE discretization and thermal FEA of the different mirror cooling configurations. FEAs of the cooling channels geometries, implemented in the launcher and receiver mirrors are conducted. It is considered that, if necessary, these mirrors can be made of one of three different materials namely, SS 316L(N)-IG, tungsten and copper. Afterwards, a transient thermal FEA of the best combination material/cooling channel geometry for each mirror is conducted considering that ITER is expected to work in 400 second pulses, with a dwell time phase of 1400 seconds between pulses. To conclude, a steady state fluid flow thermal analysis is performed to verify the pressure drop and the convection coefficient used in the previous analysis.

The results obtained are conclusive, i.e., cooling is required and with one of the proposed configurations it is possible to lower the maximum temperatures of the mirrors by approximately 80% putting it in the operating temperature range.

Next, a brief background revision that supports the development of this study follows.

1.1. Nuclear Fusion

Nowadays, energy harvesting management is an important and transversal topic among many areas as there are finite resources from which energy can be obtained. As stated in [1], "Energy is the life line of modern civilization and economic growth".

In 2014, 81.1% of total primary world energy was obtained through fossil fuels (coal, natural gas and oil) which are the most requested energy sources [2], see Figure 1. Considering that 50% of those sources will be extracted within 150 years, and taking into account the annual energy demand [3], it is anticipated that: in 30 years it will be more difficult and expensive to extract oil; coal will last approximately 200 years and; natural gas will extinguish itself in 45-60 years. Additionally, and taking into account the negative impact of emissions from the use of non-

renewable sources, urgency is expected in studying new ways of obtaining energy.

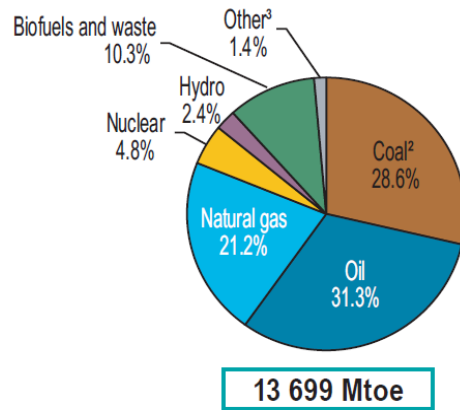


Figure 1 - Primary energy sources (2014), being "others" geothermal, wind, etc. [2].

In this context, nuclear energy presents itself as a source of energy with great potential, not only because of the sustainability, but also for its economic characteristics and the fact that it is a source of clean energy. Briefly, nuclear energy can be seen as a solution for the improvement of the ecological environment, which meets the principles of a circular economy, and has the capacity to be a long term resource [1].

This type of energy can be obtained in two ways: by fission of large nuclei, obtaining smaller ones (nuclear fission) and; by fusion of nuclei that has the inverse process of fission (nuclear fusion). In comparison to nuclear fission, fusion may be seen as a safer process that spends less fuel, [1]. One of the most promising fusion reactions is that of deuterium nucleus 2_1H with tritium nucleus 3_1H , thus producing non-radioactive isotopes of the element helium 4_2He , releasing neutrons 1_0n , and 17.59 MeV of energy [4] see Figure 2 and equation (1).



The tokamak is one of the most promising configuration for a fusion reaction to occur [1].

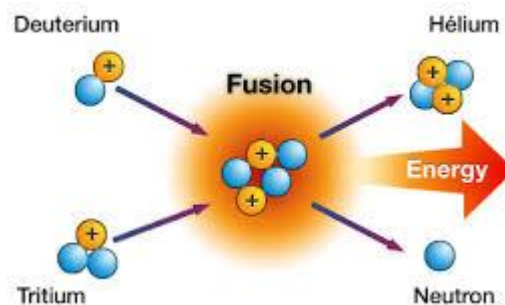


Figure 2 - Deuterium and tritium fusion reaction [4].

Currently there are approximately twenty tokamaks in operation distributed worldwide, see Table 1.

Table 1 - Tokamaks in operation [1].

Name	Country	Data from
T-10	Russia	1975
TEXTOR	Germany	1978
TEXT	USA	1980
JET	UK	1983
CASTOR	Czech Republic	1983
JT-60	Japan	1985
STOR-M	Canada	1987
Tore Supra	France	1988
Aditya	India	1989
DIII-D	USA	1986
FTU	Italy	1990
Tokamak ISTTOK	Portugal	1991
ASDEX-U	Germany	1991
Alcator C-Mod	USA	1992
TCV	Switzerland	1992
TCABR	Brazil	1994
MAST	UK	1999
NSTX	USA	1999
EAST	China	2006
KSTAR	Korea	2008

The tokamak is a system that confines plasma (ionized gas resulting from the high temperatures required for fusion to occur) in a toroidal form, using magnetic fields see Figure 3. The main magnetic field is the toroidal, which is horizontal and has the main function of confining the plasma. However, a vertical magnetic field (known as the poloidal magnetic field) is necessary, so that the plasma pressures are balanced. The poloidal magnetic field is created by inducing a current in the plasma (using a central solenoid) and by using poloidal coils. The combination of these two magnetic fields results in a magnetic field whose lines have an elliptical shape see Figure 3.

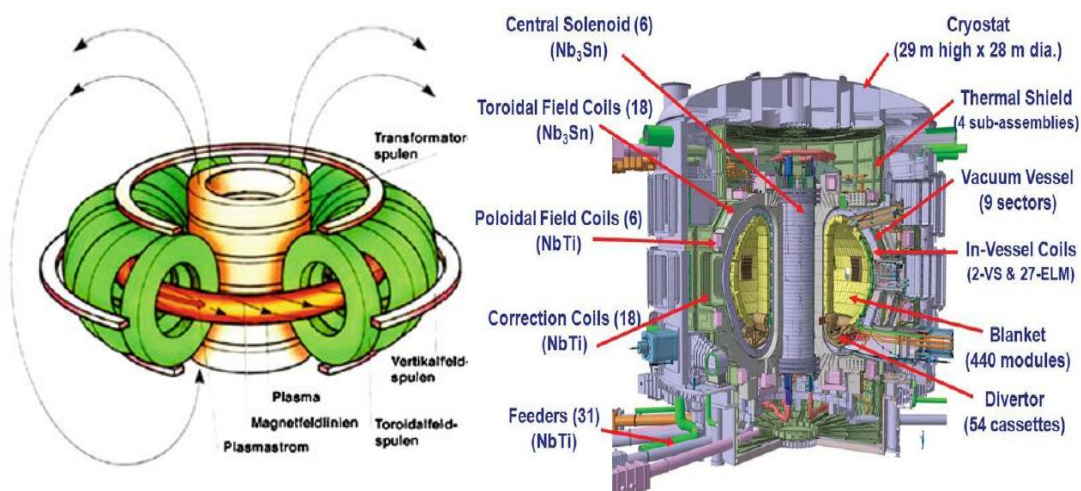


Figure 3 - Operation principle and main constituents of a tokamak [4].

The ITER organization is an international fusion energy organization. Members of ITER

organization include: The People's Republic of China; the European Atomic Energy Community (Euratom); the Republic of India; Japan; the Republic of Korea; the Russian Federation; and the United States of America. Its purpose is to promote cooperation among the members of the organization to benefit the ITER project, [5].

The ITER project aims at building the largest tokamak, ever built, in Cadarache in the south of France. ITER's tokamak is expected to be the first capable of producing energy in a quantity high enough to overcome the energy needed to supply the machine components, i.e., efficiency > 1 .

ITER will be used to test technologies, materials and the required physics regimes for the commercial production of electricity based on nuclear fusion energy. Compared to JET tokamak from the United Kingdom, which has the world record of power produced (with an input of 24 MW it produced an output of 16 MW in 1997), ITER is designed to produce 500 MW with an input of 50 MW, [6].

1.2. Diagnostics Systems

ITER will have a total of approximately fifty individual measurement systems. These systems will be essential not only to obtain diagnostic data, but also to aid in the control, evaluation and optimization of plasma performance. With all these data, it will be possible to acquire a great knowledge of the physics that surrounds the plasma [7].

The sets of ITER data collection systems available are composed of magnetic diagnostics, neutron diagnostics, microwave diagnostics, operation and plasma-based diagnostics, optical systems, bolometric systems as well as spectroscopic instruments [7].

Magnetic diagnostics provide information on magnetic balance, currents in plasma and structures, energy stored in plasma such as plasma shape and position. The measurement of the plasma position is also performed by the microwave diagnostics. The neutron diagnostics are responsible for providing information about the power obtained with the fusion reaction. Operational and plasma-based diagnostics monitor the conditions inside the main chamber and in the divertor (temperature, pressure, residual gas and tritium and dust monitoring) see Figure 4.

The range of wavelengths between visible and x-rays is analyzed by spectroscopic instruments, thus providing information on plasma impurities, plasma density, particle flow, ion temperature, helium density, plasma spin and current density. The bolometric systems are responsible for the distribution of radiation power in the plasma zones and in the divertor. Finally, optical systems (Thomson scattering systems and interferometers) have the function of measuring temperature profiles and plasma density. The CTS system is an optical diagnostics system and, as already mentioned, the main function of those is to measure temperature profiles and plasma density. This is achieved by characterizing the speed of the fast ions (*"(...) elusive particles that are a natural consequence of the fusion process and plasma heating techniques,*

and which carry energies some two orders of magnitude higher than the 'bulk' ions and electrons in the plasma.", [8]). CTS is also used as a supplementary system in obtaining data regarding ion temperature, plasma rotation and possibly the fuel-ion ratio, [9].

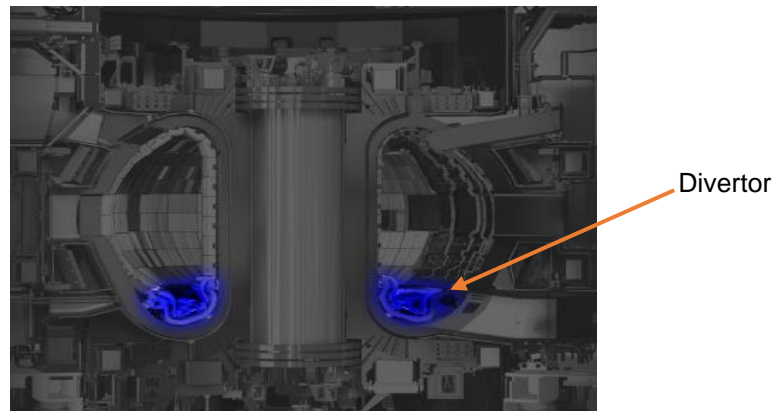


Figure 4 - Divertor localization in the tokamak.

The basic principle of the CTS system is the Thomson scattering, which uses electromagnetic waves. Thomson scattering is an elastic dispersion of radiation by photons of uncharged particles and is basically the minimum energy limit of Compton scattering. There are two types of Thomson scattering in the field of fusion research, the Incoherent Thomson Scattering and the CTS, the latter being used in ITER Low Field Side (LFS) CTS, [10]. Diagnostics systems that use electromagnetic waves play an important role in diagnostics as the plasma actively interacts with them.

The radiation dispersion geometry is defined by two wave vectors representing two types of electromagnetic waves, the incident radiation wave (k^i) and the scattered radiation wave (k^s). As illustrated in Figure 5, is possible to get the fluctuation vector defined by equation (2), [11]:

$$k^\delta = k^s - k^i. \quad (2)$$

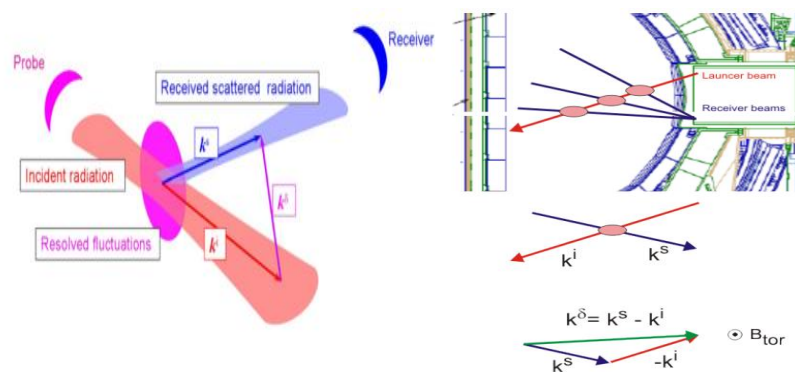


Figure 5 - Beam scattering geometry. Left figure taken from [11] and right figure from [9].

In order to reduce the dispersion angle limit (angle between the incident and scattered wave vector), the incident radiation is produced by a gyrotron, which is the necessary tool to produce electromagnetic radiation with a sufficiently high frequency to simulate the cyclotron resonance of the electrons moving in a strong magnetic field.

This electron motion, schematized in Figure 6, is also the source of ECE (Electron Cyclotron Emission) that acts as noise for the CTS signal. Thus, to filter the ECE, the gyrotron operates in the form of pulses (ON/OFF), so that, when it is ON the reading obtained has the CTS signal plus the ECE and, when it is turned OFF, only the ECE. This way, it is possible to subtract one reading from the other to obtain the CTS signal [11].

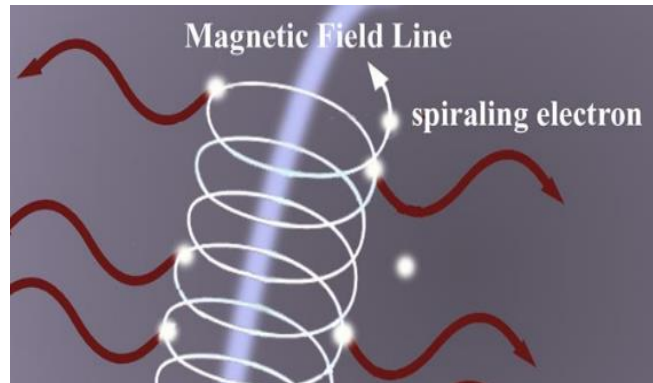


Figure 6 - ECE schematic representation [11].

The ITER's tokamak CTS system (ITER CTS) is illustrated in Figure 7. Although there are already CTS systems in some tokamaks, such as in TEXTOR and ASDEX Upgrade, the system that will be applied in ITER has some unique aspects, e.g., the sight lines are narrowed, due to the higher neutron flux and the higher densities that may lead to greater refraction.

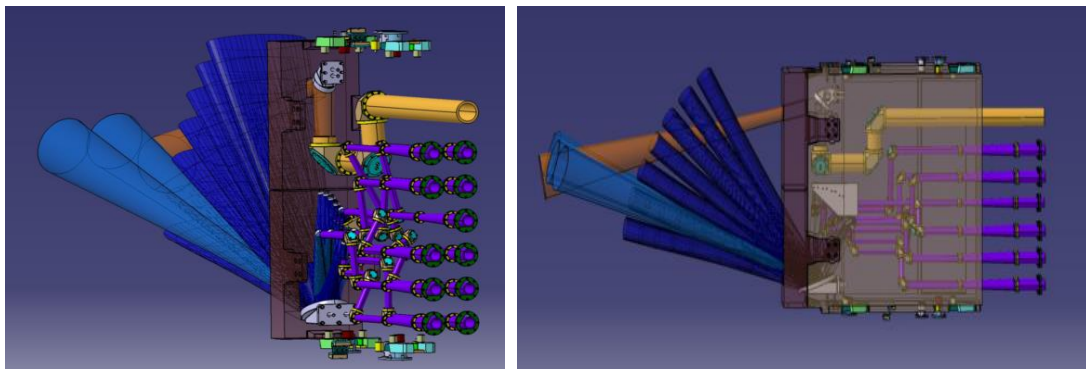


Figure 7 - ITER CTS [9].

The ITER CTS location will be in drawer three of the tokamak equatorial port 12. The diagnostic system is equipped with a microwave source (60 GHz, 1.0 MW gyrotron), transmission lines, mirrors to reflect the incident beam in X-mode for plasma, waveguides, a mm-wave detector system and electronic data acquisition and processing components [9].

As the ITER CTS system is still under development, constant design changes are being made. As an example, consider the number of mirrors illustrated in Figure 8, that has been reduced from four to two [9].

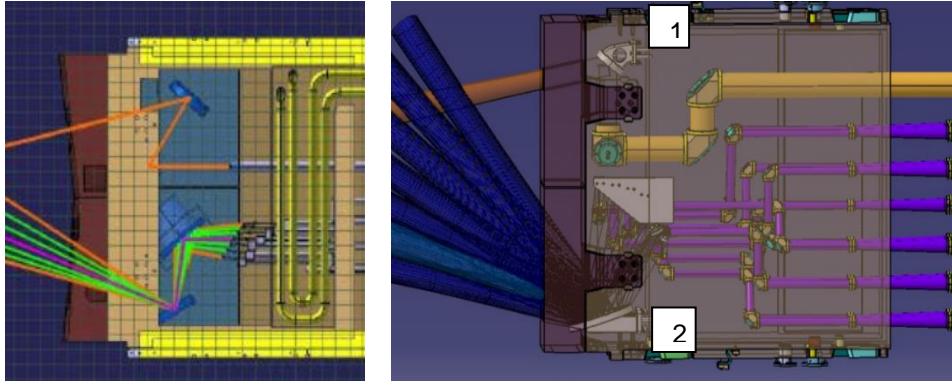


Figure 8 - ITER CTS system configurations: (left) old; (right) actual. Mirror 1 is related to the incident beam and mirror 2 to the scattering radiation.

The focus of this dissertation is the launcher and the receiver mirrors, i.e., the one that reflects the microwave beam into the plasma and the one that receives and guides the CTS signal into the waveguides, respectively. It is necessary to consider that these mirrors are heated by means of thermal radiation from the plasma, stray radiation that comes from the other systems present in the tokamak, the neutron flux resulting from the fusion reaction and the electromagnetic beams. Hence, it is necessary to conduct thermal analyses to establish the requirements to cool down these mirrors.

1.3. Mechanical Engineering Framework

Since the emergence of machines, with greater emphasis during the industrial revolution, in the eighteenth century, when there was a transition from production by handmade methods to production by machines, that cooling systems are required for some components of the machinery in question.

Various types of heat removal equipments have been developed by mechanical engineers and are used in various fields, such as in industry (electricity production, refineries, etc.), in transportation and electronic components. For this purpose, various fluids such as air and water are used.

As previously mentioned, the two mirrors present in the ITER CTS require a cooling system. Therefore, to perform a study of these mirrors it is necessary to make recourse to some mechanical engineering fields like heat transfer and fluid mechanics.

1.3.1. Brief Heat Transfer Background

In a historical context, during the period between 1700 and 1920, lived six of the greatest heat transfer pioneers: Newton; Black; Fourier; Carnot; Planck; and Nusselt. According to [12], in 1701 Isaac Newton published, in Latin and anonymously, "*Scala Graduum Caloris*" ("A Scale of the Degrees of Heat"), where he presented the first empirical equation of heat flow, commonly known as Newton's law of cooling. However, it was only discussed in scientific publications between 1800 and 1950.

Nevertheless, according to [13], only between 1768 and 1830 did Jean Baptiste Joseph

Fourier formulate the differential equation that describes the transient process of conduction and also the empirical relationship between conduction in a body and the gradient of temperature in the direction of the heat flow (Fourier's law).

Regarding thermal radiation, among the greatest exponents of history are three names: Planck, with the analysis of the radiation spectrum of a black body; Wien, with the displacement law and; Stefan-Boltzmann, with studies on the radiation intensity [14].

1.3.2. Brief Fluid Mechanics Background

Sailing ships with oars and irrigation systems were probably the first flow problems dealt in the prehistoric times. The earlier quantitative information on fluid mechanics was provided by Archimedes and Hero of Alexandria with the parallelogram law for addition of vector and in the third-century the laws of buoyancy.

Other relevant developments were the equation of mass conservation, initiated by Leonardo da Vinci, the laws of motion and the law of viscosity of the linear fluids, now called Newtonian by Isaac Newton during the eighteenth century. The differential equation of motion and their integral form, called the Bernoulli equation developed by Euler, the addition of the viscous terms to the equation of motion by Navier and Stokes at the end of the nineteenth century and the boundary layer theory by Ludwig Prandtl in 1904 [15].

Fluid flow requires a great deal of theoretical treatment, and consequently, is often applied to idealized situations. The two main obstacles in fluid mechanics are geometry and viscosity. In order to treat complex problems, it is possible to apply numerical computer techniques, e.g., Computational Fluid Dynamics (CFD) that was developed during the second half of the twentieth century [15].

Due to the viscosity, there is an increase of difficulty to handle the basic equations. However, as previously mentioned, Prandtl developed the boundary layer approximation which contemplates simplified viscous-flow analyses.

Viscosity has a destabilizing effect on fluids giving rise to a phenomenon called turbulence. This phenomenon was first reported by the German engineer G.H.L Hagen in 1839, establishing that there were two viscous-flow regimes, i.e., turbulent and laminar [15].

The theory of turbulent flow is influenced by experimental results. Nevertheless, apart from the standard experimental correlation for turbulent time-mean flow, were developed advanced texts on time-mean turbulence, turbulence modeling and, due to computational advances, computer-intensive Direct Numerical Simulation (DNS) of fluctuating turbulence have been developed.

1.4. Problem statement

As previously mentioned, this dissertation consists of the development of a cooling system for the launcher and receiver mirrors of the ITER CTS system. For this purpose, it is

necessary to assess the surrounding environment of the mirrors: the thermal loads to which they are subjected to and the material and design constraints that apply.

The mirrors will be subjected to heat sources, such as thermal radiation coming from the plasma, stray radiation, microwave radiation coming from the gyrotron and heat due to the neutron flux that will be accounted as internal heat generation, [16].

SS 316L(N)-IG is the material specified by ITER for the two mirrors. However, some other materials (tungsten and copper) are studied in this dissertation to provide alternatives to some of the problems that this steel may endorse.

During this dissertation, it is verified that a cooling system is indeed required, being the cooling fluid water (ITER requirement). Hence, in order to select feasible cooling channel geometries for the cooling system, it is tested ten cooling channel geometries, each one with different features that influence the performance of the cooling system.

According to [16], the maximum mass flow rate of water available for the ITER CTS system is 1.5 Kg/s , and it can be utilized in a series or parallel cooling system, meaning that the same cooling fluid can be used in all the cooling systems implemented in this CTS system or it can be divided by each cooling system, respectively.

The methodology adopted consists of a steady state thermal FEA of the ten cooling channels geometries, implemented in the launcher and receiver mirrors. Note that three different materials are studied for the mirrors. Then, a transient state thermal FEA of the best combination material/cooling channel geometry for each mirror is conducted. To conclude, a steady state fluid flow thermal analysis is performed to verify the convection coefficient used in the previous analysis.

Following the implementation of this methodology, the chosen configurations for the SS 316L(N)-IG are:

- A cooling channel geometry (1_RETAN_120x14) if the mass flow rate is larger (or equal) than $0,5 \text{ Kg/s}$;
- A cooling channel geometry (ZIGZAG_D_14MM) if the mass flow rate is smaller than $0,5 \text{ Kg/s}$ and;
- A cooling channel geometry (1_RETAN_240x14) for the receiver mirror.

The results obtained are conclusive making the methodology recommendable to be used in future studies of similar components.

As a result of this dissertation, it is worth mentioning the following original contributions:

- The methodology developed and used to study the CTS mirrors may applied to other be components of the ITER project under similar conditions;
- The MATLAB routine developed and used to compute the power distribution on the surface of the launcher mirror;

- Cooling channel geometries for the launcher and receiver mirrors that can effectively decrease the maximum temperatures by ~80.5% and ~93.5% respectively, putting it in the operating temperature range.

This document is composed of five main chapters. The first is an introductory chapter where the theme and motivation are introduced, justifying this study in terms of mechanical engineering and particularly in the heat transfer field. The second chapter introduces some of the most relevant fundamentals regarding physical laws and/or mathematical concepts that support the study developed in this dissertation. The third chapter regards the methodology developed to solve the problem. In the fourth chapter, are presented the main results and respective discussion. In the fifth and final chapter, are presented the main original contributions and conclusions of this dissertation as well as some suggestions for future works.

2. Fundamentals

In this chapter the most relevant fundamentals and equations here used from the heat transfer and fluid flow fields are presented, as well a brief description of the FE used and respective equations.

2.1. Heat Transfer

Considering the first law of thermodynamics, heat transfer occurs due to a peculiar feature of matter, called temperature. Regarding the migration of this energy, the second law of thermodynamics shows that the direction is always from the body of higher temperature to that of lower temperature. Thus, there are three forms of heat transfer:

1. Conduction - Occurs by the influence of elastic impacts between molecules in gases, as well as due to longitudinal oscillations in non-electrically conductive solids. It should also be noted that this phenomenon occurs due to the movement of electrons in metallic materials;
2. Convection - Refers to the transport and transmission of heat imposed by the movement of distinct parts of a fluid in the presence of a temperature gradient;
3. Radiation - Phenomenon that occurs due to the propagation of electromagnetic waves, being the only one that does not need a material medium to propagate.

Within the tokamak, the environment between components is considered to be vacuum. Consequently, the most relevant heat transfer process between components will be in the form of radiation. Nevertheless, there is conduction inside each component, as well as convection in all elements with a cooling system.

2.1.1. Conduction

Conduction may be defined as the energy transfer on the form of heat in the same medium, from one point to another.

Consider a plane wall with thickness $[m]$ and with both surfaces at different but constant temperatures, $(T_1$ and $T_2)$. The amount of heat transmitted through the cross-section area of the plane wall $(A [m^2])$, per unit of time, is called heat rate $(q [W])$ and it can be computed using the following equation:

$$q = \frac{k}{b} A (T_1 - T_2), \quad (3)$$

being k , in $\left[\frac{W}{mK}\right]$, the plane wall material thermal conductivity and $T_1 > T_2$, [17].

As presented in [14], on the form of a differential equation and per unit of cross-section area, equation (3) can be expressed as follows:

$$q'' = -k \frac{dT}{dx}, \quad (4)$$

being this equation known as Fourier's law.

Alternatively, a conduction problem can be approached using the electric analogue, where the flux is considered to be analogous to the current intensity, the temperature to the electrical voltage and the thermal resistance to the electric resistance R . This last parameter, R , can be computed as follows:

$$R = \frac{L}{kA}, \quad (5)$$

with L representing the length traveled by the heat in [m].

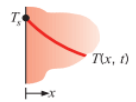
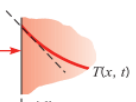
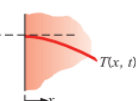
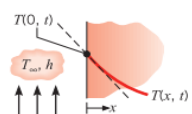
As not all materials are considered isotropic, this implies a variation of the k value with the direction. Hence, the transient heat diffusion equation can be expressed as follows:

$$\frac{\partial}{\partial x} \left(k \frac{\partial T}{\partial x} \right) + \frac{\partial}{\partial y} \left(k \frac{\partial T}{\partial y} \right) + \frac{\partial}{\partial z} \left(k \frac{\partial T}{\partial z} \right) + \dot{q} = \rho c_p \frac{\partial T}{\partial t}, \quad (6)$$

where \dot{q} is the amount of internal energy generation per unit of time and volume, [$\frac{W}{m^3}$], and ρ and c_p are the density ($[\frac{Kg}{m^3}]$) and specific heat at constant pressure ($[\frac{KJ}{KgK}]$), respectively. Equation (6) is here expressed in Cartesian coordinates, but can also be expressed in cylindrical and spherical coordinates, as presented in [14].

Regarding the boundary conditions in a conduction problem, one can highlight those presented in Table 2.

Table 2 - Boundary conditions for the heat diffusion equation on a surface ($x=0$), [14].

1. Constant surface temperature		
$T(0, t) = T_s$	(2.31)	
2. Constant surface heat flux		
(a) Finite heat flux		
$-k \frac{\partial T}{\partial x} \Big _{x=0} = q_s''$	(2.32)	
(b) Adiabatic or insulated surface		
$\frac{\partial T}{\partial x} \Big _{x=0} = 0$	(2.33)	
3. Convection surface condition		
$-k \frac{\partial T}{\partial x} \Big _{x=0} = h[T_\infty - T(0, t)]$	(2.34)	

One of the important properties, regarding the heat transfer on the form of conduction, is the thermal diffusivity (α [$\frac{m^2}{s}$]), expressed as

$$\alpha = \frac{k}{\rho c_p}. \quad (7)$$

This property, according to [14], consists of the measurement of the capacity that a

material has to conduct thermal energy relatively to its capacity to store it, in other words, it is the ability to transfer information from the boundary to the interior, as can be concluded with the analysis of the constituent terms of equation (7).

2.1.2. Convection

Convection occurs between different fluids, between fluids and surfaces or even between parts of the same fluid, provided that a temperature gradient exists.

Assuming that a surface is at temperature T_s , in contact with a fluid at temperature T_∞ and with a given convection coefficient $h \left[\frac{W}{m^2 K} \right]$, the heat flux present in this situation may be, according to [14], obtained through Newton's law of cooling:

$$q''_s = h(T_s - T_\infty). \quad (8)$$

Convection can be characterized as forced convection (in external flow or internal flow) or as natural convection.

For the purpose of the work carried throughout this dissertation, forced convection in internal flow will be the most relevant. Therefore, some notions of internal flow inside channels are presented.

The Reynolds' number, for internal flows, can be obtained as follows:

$$Re_D = \frac{\rho u_m D_h}{\mu} = \frac{\dot{m} D_h}{A \mu}; \quad (9)$$

$$D_h = \frac{4 * A}{P}; \quad (10)$$

where u_m is the mean flow velocity ($\left[\frac{m}{s} \right]$), D_h is the characteristic hydraulic diameter of the cross-section in $[m]$ (which may be calculated using equation (10)), A and P are the cross section area and perimeter in m^2 and m , respectively, μ is the viscosity of the fluid $\left[\frac{N s}{m^2} \right]$ and \dot{m} the mass flow rate in $\left[\frac{Kg}{s} \right]$.

Considering Re_D , a flow can be characterized as being laminar or turbulent. For this purpose, it will be considered, as in [14], that the Re_D critical value (i.e., the value above which the flow leaves the laminar regime) is the one presented in equation (11).

$$Re_{D,c} \approx 2300. \quad (11)$$

In the inner flow, one has two regions that are important to define: the hydrodynamic entry region and the fully develop region. These two regions are illustrated in Figure 9.

For laminar flow ($Re_{D,c} \leq 2300$), the length of the hydrodynamic entry region is obtained by:

$$\left(\frac{x_{fd,h}}{D} \right)_{lam} \approx 0,05 Re_D, \quad (12)$$

where $x_{fd,h}$ is the length in m .

For the value of $x_{fd,h}$ in turbulent regime, the same value will be assumed as in [14] which is obtained using the following inequation:

$$\left(\frac{x_{fd,h}}{D}\right)_{turb} > 10. \quad (13)$$

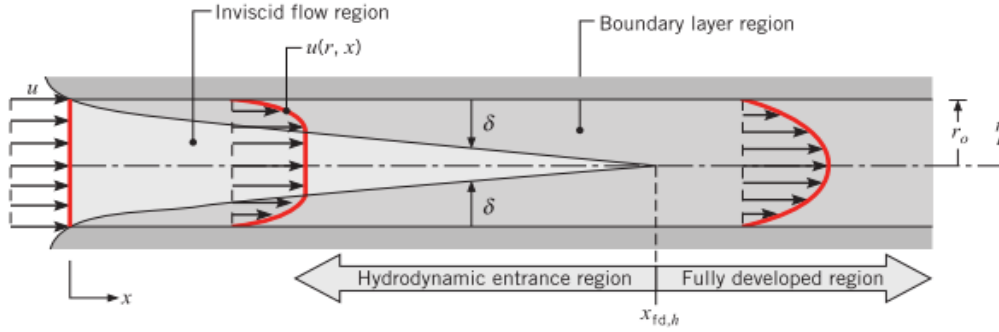


Figure 9 - Laminar flow boundary layer development in a circular tube [14].

As previously mentioned, knowing the development of the flow is an essential part of the problem. For the flow, the value of $x_{fd,h}$ differs when the thermal boundary layer is considered simultaneously. Hence, the procedure for calculating the length of the thermal input region, both for laminar flow and for turbulent flow, is given in equations(14) and (15), taking into account [14]:

$$\left(\frac{x_{fd,t}}{D}\right)_{lam} \approx 0,05 Re_D Pr; \quad (14)$$

$$\left(\frac{x_{fd,t}}{D}\right)_{turb} = 10. \quad (15)$$

Noticing the dependence of the number of Prandtl (Pr) on the laminar regime, and considering the approximation carried out for the turbulent regime, the flow conditions are almost independent of Pr . Thus, Pr is obtained considering fluid properties through the following equation:

$$Pr = \frac{\mu c_p}{k} \quad (16)$$

In Figure 10, one can observe schematically the thermal boundary layer, as well as its development.

Considering the flow of a fluid in a tube having a surface temperature T_s , the power removed to the tube by the fluid may be obtained performing an energy balance to the latter. Knowing the average inlet and outlet temperatures, the mass flow rate and the specific heat, the power q_{conv} can be obtained using equation (17):

$$q_{conv} = \dot{m}c_p(T_{m,o} - T_{m,i}). \quad (17)$$

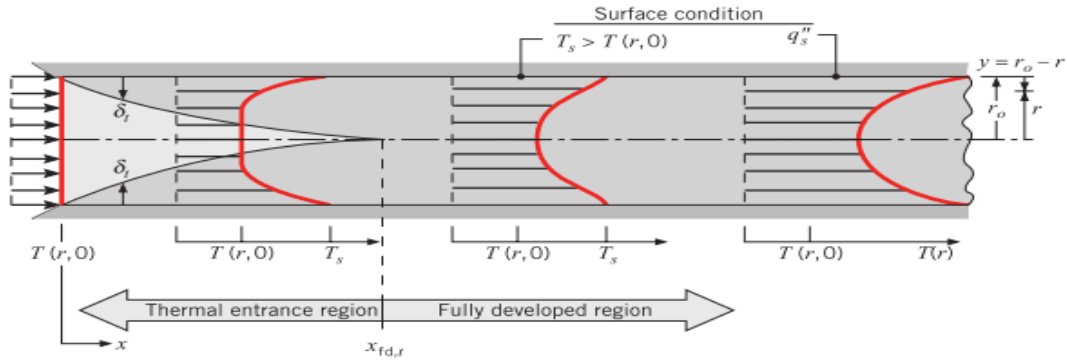


Figure 10 - Thermal boundary layer development in a circular cross-section tube [14].

According to [14], in internal flow two approaches may be considered as far as the boundary condition is concerned (i.e., constant heat flux and constant surface temperature approaches) and for the resolution of convection problems that implies considering that the flux or the surface temperature is constant. The constant heat flux approach is performed whenever an electric resistance heats the tube, or if it is being irradiated uniformly. In contrast, the approach to constant surface temperature is only applied if there are changes in phase of the fluid.

In this dissertation, for the problem that is being addressed (see chapter 1), the approach considered is constant heat flux. As such, the flow of heat exiting the surface of a tube into the fluid flowing in the interior is obtained according to equation (18):

$$q_s'' = \frac{q_{conv}}{P L}, \quad (18)$$

where P is the internal perimeter of the tube in [m] and L the length of the tube in [m]. The product of the two parameters allows obtaining the tube's inner surface area in contact with the fluid.

The Nusselt number, according to [14], is for the thermal boundary layer as the friction coefficient is for the hydrodynamic boundary layer. A second definition allows to define such a parameter as the quotient between the heat transferred by convection and by conduction in a fluid. For internal flows, it can be expressed as:

$$Nu_D = \frac{h D_h}{k}, \quad (19)$$

being its value dependent of some conditions.

If the flow is considered turbulent and fully developed, where $Re_D \geq 10000$ and Pr between 0.6 and 160, then:

$$Nu_D = 0,023 Re_D^{4/5} Pr^n, \quad (20)$$

where n is 0.4 if $T_s > T_m$ and 0.3 if $T_s < T_m$. T_m is the mean fluid temperature, considering the inlet and outlet temperatures of the fluid, and is used to define properties of the fluid, e.g., viscosity.

2.1.3. Radiation

Heat transfer by radiation, as previously mentioned, is the only form that does not require

a material medium to propagate. Hence, it is considered to be the most predominant in the universe.

The various radiative fluxes that interfere with a radiation problem are presented below. Thus, the emissive power of a body may be given by the following equation, extracted from [14]:

$$E = \varepsilon \sigma T_s^4, \quad (21)$$

where E is the emissive power in $\left[\frac{W}{m^2}\right]$, ε the emissivity of the surface of the body, σ the Stefan-Boltzmann with the value of $5,670E - 8 \left[\frac{W}{m^2K^4}\right]$ and T_s the surface temperature in K .

Irradiation ($G \left[\frac{W}{m^2}\right]$) is the power per unit area that falls on a surface and can be absorbed, transmitted (if the body is not opaque) or reflected. Considering energy conservation, it is possible to establish a relation between the absorbance (α_{abs}), the reflectivity (ρ_{ref}) and the transmissibility (τ), as presented in the following equation:

$$\alpha_{abs} + \rho_{ref} + \tau = 1. \quad (22)$$

If the surface is opaque ($\tau = 0$) and equation (22) simplifies to:

$$\alpha_{abs} + \rho_{ref} = 1. \quad (23)$$

The radiosity ($J \left[\frac{W}{m^2}\right]$) represents the radiation per unit area that leaves a surface and may be expressed as:

$$J = E + \rho_{ref}G. \quad (24)$$

The radiative net flux ($q''_{rad} \left[\frac{W}{m^2}\right]$) can be obtained as follows:

$$q''_{rad} = J - G, \quad (25)$$

If the medium is opaque ($\tau = 0$), the radiative net flux ($q''_{rad} \left[\frac{W}{m^2}\right]$) may be expressed as:

$$q''_{rad} = \varepsilon \sigma T_s^4 - \alpha_{abs}G. \quad (26)$$

Knowing that radiation can propagate in all directions, it can affect a surface with dissimilar angles of incidence. Thus, this effect has to be accounted in the radiative fluxes, computed previously, as it influences the spectral intensity calculation of the radiation $I_{\lambda,e}$. The radiation intensity can be defined as the rate at which radiative energy is emitted at a wavelength λ in the θ and ϕ directions.

The influence of the value of $I_{\lambda,e}$ can be verified in the equations presented in chapter 12 of [14]. If the radiation is considered diffuse, the radiative rates computations can be simplified since the intensity becomes independent of the direction ($I_{\lambda,e}(\lambda, \theta, \phi) = I_{\lambda,e}(\lambda)$).

This is the case of a blackbody that has the following characteristics:

- Absorbs all incoming radiation independently of λ or direction, $\alpha(\lambda, T) = 1$;
- For a given temperature T , no body emits more radiation than a black body, $\varepsilon(\lambda, T) =$

1;

- Although the radiation of a blackbody depends on the λ and T , it is independent of the direction, thus being a diffuse emitter.

Considering that the emissivity of a blackbody is 1 ($\varepsilon(\lambda, T) = 1$) and making use of equation (21), its emissive power may be expressed by:

$$E_b = \sigma T^4. \quad (27)$$

However, not all bodies can be considered as a blackbody and, therefore, their emissivity is different from the unit value, being computed using equation (28).

$$\varepsilon(T) = \frac{E(T)}{E_b(T)}. \quad (28)$$

Considering a closed enclosure in which, the walls are black, being verified the presence of a body in its interior and that under steady state conditions the thermal equilibrium is reached, taking an energy balance, one obtains the following relation, denominated Kirchhoff's law:

$$\frac{E_{body}(T_s)}{\alpha_{body}} = E_b(T). \quad (29)$$

In this way and taking into account [14], one obtains equation (30).

$$\frac{\varepsilon}{\alpha_{body}} = 1, \quad (30)$$

This result ensures that the emissivity and the absorptivity are identical for all surfaces of the bodies under the mentioned conditions, i.e.,

$$\varepsilon = \alpha_{abs} \quad (31)$$

However, it should be noted that this is only valid as the parameter G refers to irradiation coming from a blackbody. Furthermore, the spectral values of the quantities presented in equation (31) follow the same relationship. Hence, it is necessary to introduce the definition of a gray surface, which is classified as a surface with values of emissivity and spectral absorbance independent of λ .

Thus, considering equation (22) and an opaque, diffuse, gray surface with incident radiation coming from a black body, the reflectivity ρ_{ref} expressed by equation (32) is derived.

$$\rho_{ref} = 1 - \alpha_{abs} = 1 - \varepsilon \quad (32)$$

To analyze the radiative exchange between two or more surfaces it is necessary to calculate view factors. Considering two surfaces as illustrated in Figure 11, it is inferable that not all the emitted radiation by a surface reaches its homonymous. Thus, the concept of view factor arises, F_{ij} .

The view factor can then assume a value between 0 and 1, being the general expression to calculate its value, between two surfaces, given by equation (33).

$$F_{ij} = \frac{1}{A_i} \int_{A_i} \int_{A_j} \frac{\cos(\theta_i) \cos(\theta_j)}{\pi R_{ij}^2} dA_i dA_j, \quad (33)$$

where θ represents the angle [rad] between the normal and imaginary line joining the centers of each surface, and R_{ij} the length [m] of this imaginary line, [14].

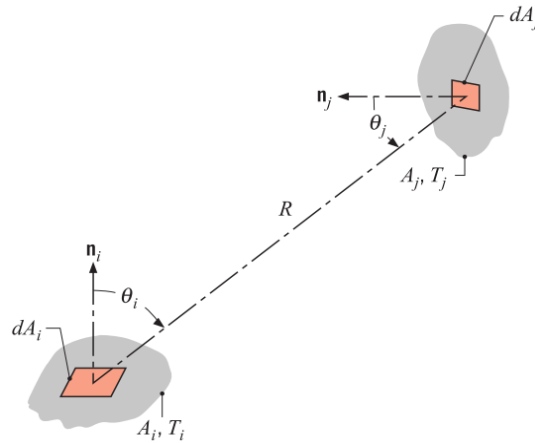


Figure 11 - View factor between the element dA_i and dA_j [14].

Some of the most important relations of the view factors are expressed below:

$$A_i F_{ij} = A_j F_{ji}; \quad (34)$$

$$\sum_{j=1}^N F_{ij} = 1, N \text{ enclosure surfaces}; \quad (35)$$

Note that certain view factors can be estimated, for specific cases, through tables and plots, as illustrated in Figure 12.

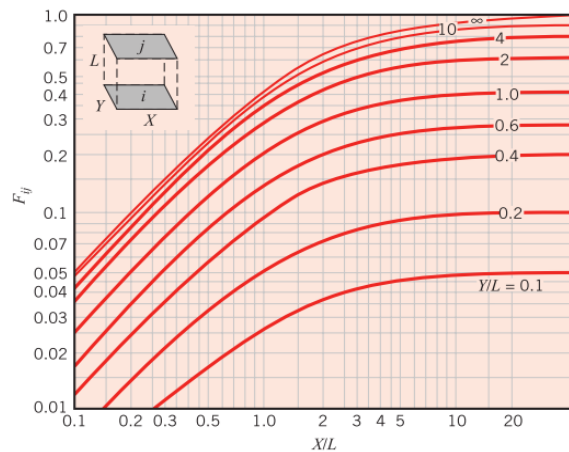


Figure 12 - View factor for parallel rectangular plates [14].

The power exchanged between a surface i and all surfaces present in an enclosure, $q_{rad\ i}$, can be calculated using equation (36).

$$q_{rad\ i} = \sum_{j=1}^N A_i F_{ij} (J_i - J_j). \quad (36)$$

On the other hand, the radiation that impinges on one surface, coming from all the others (irradiation in [W]) can be obtained through equation (37).

$$G_i = \sum_{j=1}^N A_i F_{ij} J_j. \quad (37)$$

It should be mentioned that the electric analogue can be considered as a method for solving radiation problems, the analogy is schematically illustrated in the Figure 13.

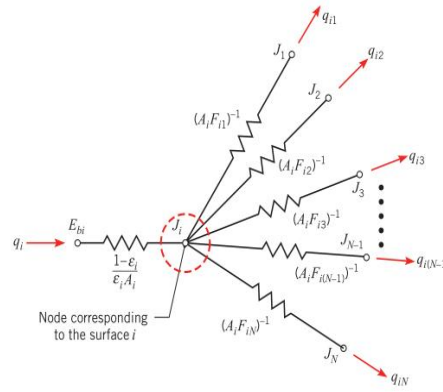


Figure 13 - Electric analogue representation for a heat transfer radiation problem [14].

In the context of this dissertation, it is relevant to refer a specific case that involves radiation exchanges between a small surface at T_s and a much larger isothermal surface that surrounds the smaller one. The surroundings, for example, may be the walls of a room whose temperature T_{sur} differs from that of an enclosed surface. If the surface is assumed to be a gray surface, the net rate of radiation heat transfer flux from the surface is, according to [14]:

$$q''_{rad} = \epsilon\sigma(T_s^4 - T_{sur}^4). \quad (38)$$

When solving radiation problems recurring to computational methods, the estimation of the view factors may be performed using the hemicube method illustrated in Figure 14.

According to the hemicube method, if a surface of a 3D body emits radiation, it is divided into N smaller 2D elements, called pixels. Hence, the accuracy of the results depends on the resolution of the hemicube (hence, increasing the number of divisions implies an increase of the accuracy) [18].

According to [18], the view factor may be calculated as follows:

$$F_{ij} = \sum_{n=1}^N \Delta F_n = \frac{\cos(\theta_i) \cos(\theta_j)}{\pi R_{ij}^2} \Delta A_j. \quad (39)$$

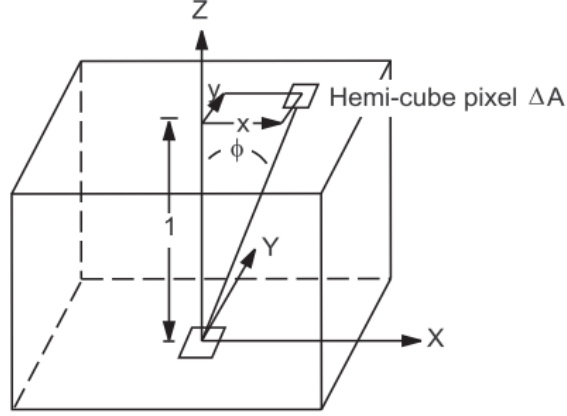


Figure 14 - Hemicube method geometric representation [18].

Knowing that the microwaves present in the ITER CTS system have a density distribution on the launcher mirror in $\left[\frac{W}{m^2}\right]$, the equation that allows to describe this parameter may be expressed, in Cartesian coordinates as:

$$P_{beam}(x, y) = P_{tot} \frac{2}{\pi w_x w_y} \exp\left(-2\left(\frac{x^2}{w_x^2} + \frac{y^2}{w_y^2}\right)\right), \quad (40)$$

where w_x and w_y are the characteristic dimensions of the microwave beam with a Gaussian distribution and P_{tot} [W] the total power of the beam [16].

For metals, the fraction of power absorbed due to a normal incidence of radiation (A), assuming that the transmitted fraction is negligible, may be calculated using:

$$A_{abs} = \left(\frac{4}{Z_0}\right) \sqrt{\pi f_{Hz} \mu_0 \rho_{res}}, \quad (41)$$

being Z_0 [Ω] the empty space impedance, f_{Hz} [GHz] the gyrotron frequency, μ_0 $\left[\frac{\Omega s}{m}\right]$ the empty space permeability and ρ_{res} [$\mu\Omega * m$] the electrical resistivity.

2.1.4. Internal Heat Generation

In this dissertation, internal heat generation is considered as the collision of neutrons with the atoms of a body is responsible for the generation of internal heat. This process consists of converting the kinetic energy of the neutrons into heat at the time of the collision with the atomic particles.

The internal heat generation can be represented by equation (42).

$$F_6 = \frac{\rho_a}{V\rho} \int_V \int_t \int_E \sigma_t(E_{par}) H(E_{par}) \varphi(r_s, E_{par}, t) dE_{par} dt dV, \quad (42)$$

being t [s] the discharge time, V [cm^3] the volume of material, ρ_a $\left[\frac{atoms}{cm^3}\right]$ the atomic density, ρ $\left[\frac{g}{cm^3}\right]$ the density of material, $\varphi(r_s, E, t)$ the particle flow, $H(E_{par})$ $\left[\frac{MeV}{collision}\right]$ the heating response, $\sigma_t(E_{par})$ [cm^2] the microscopic total cross section, [19]. The unit of F_6 is [MeV] per [g] of material

per particle. In order to obtain the internal heat load in $\left[\frac{W}{cm^3}\right]$ one must multiply F_6 by the intensity of the source of particles (source of neutrons) and by the density of the material.

It should be noted that in this dissertation, these quantities are estimated using the Monte Carlo N-Particle (MCNP) code [20].

2.2. Finite Elements Method

With the technological revolution, there was a significant progress in the field of mathematical models. This led to the development of numerical methods, responsible for the ability to obtain solutions close to the reality, which may have translated into considerable benefits for the engineering world. Until then, the problems analyzed in the field in question had complex boundary conditions and geometries, which implied the use of gross and erroneous approaches. These benefits are relevant since the engineering products have high dependence on the analysis' sophistication elaborated at the design phase.

According to [17], two of the most popular numerical methods stand out:

- Finite difference method (FDM);
- Finite element method (FEM).

The FDM may be considered relatively easy to implement and can be applied directly to differential equations. However, this method has limitations regarding the field of boundaries. This constraint translates into a more frequent use of the FEM, characterized by its higher performance in this field, allowing the use of curved or linear boundaries.

Another advantage of FEM is the possibility of discretizing the domain into as many elements (of variable sizes) as necessary, as well as allowing to vary the elements' degree of interpolation.

To solve a practical problem using the FEM it is necessary to formulate it adequately, [21]. This implies the previous obtaining of a properly prepared and discretized mathematical model.

For its use, it is recommended to follow the next steps:

1. Discretization of the solution zone, dividing it into Finite Elements (FEs), that is, to create a mesh;
2. Select interpolation functions, where the polynomials degree is usually defined by the number of nodes of each element;
3. Finding the elements properties, thus establishing the equations for each FE (Galerkin method or Rayleigh-Ritz are presented as hypotheses to be considered);
4. Perform the assembly of the FEs equations to obtain the global equations of the system;
5. Solve the global system equation using direct or iterative methods;

6. Carry out additional calculations, since in addition to temperature, the heat rates and power are also relevant data when analyzing a thermal problem.

These steps are considered in the scheme presented in Figure 15.

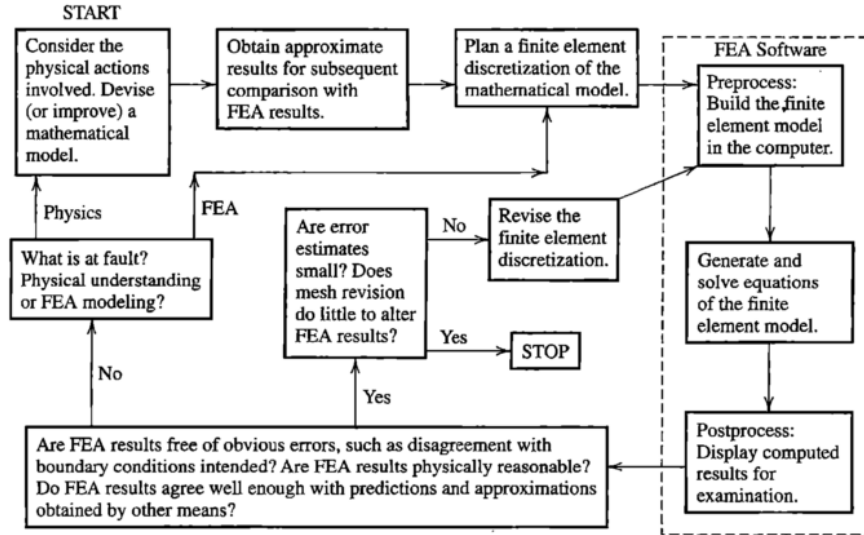


Figure 15 - Outline of a FEA implementation, [21].

It is important to note that the precision of the results, using FEM, is directly proportional to the number of nodes established during the discretization.

2.2.1. FEM Applied to Heat Transfer

The heat diffusion equation (6) combined with the boundary conditions of Table 2, see § 2.1.1, represent the strong formulation of a heat transfer problem.

Accordingly, and taking into account [22], the boundary conditions considered in this dissertation are presented as:

- Specific temperature:

$$T_s = T(x, y, z, t); \quad (43)$$

- Specific heat flux:

$$q''_x n_x + q''_y n_y + q''_z n_z = -q''_s; \quad (44)$$

- Convection:

$$q''_x n_x + q''_y n_y + q''_z n_z = h(T_s - T_e); \quad (45)$$

- Radiation:

$$q''_x n_x + q''_y n_y + q''_z n_z = \sigma \varepsilon T_s^4; \quad (46)$$

being q'' (see equation (4)) and the remaining parameters previously defined.

The FEM starts with the definition of the solution zone, i.e., the domain V is divided into FEs connected by nodes. Then the interpolation functions for each FE are determined [22]. Since

in the present case it is intended to interpolate the temperature, it is necessary to use shape functions N_i :

$$T = [N]\{T\}; \quad (47)$$

$$[N] = [N_1 \ N_2 \ \dots]; \quad (48)$$

$$\{T\} = \{T_1 \ T_2 \ \dots\}; \quad (49)$$

where $[N]$ and $\{T\}$ are the matrix of the shape functions and the temperature vector at each node, respectively.

Differentiating the temperature interpolation equations, the following relations for the temperature gradients are obtained:

$$\begin{Bmatrix} \partial T / \partial x \\ \partial T / \partial y \\ \partial T / \partial z \end{Bmatrix} = \begin{bmatrix} \partial N_1 / \partial x & \partial N_2 / \partial x & \dots \\ \partial N_1 / \partial y & \partial N_2 / \partial y & \dots \\ \partial N_1 / \partial z & \partial N_2 / \partial z & \dots \end{bmatrix} \{T\} = [B]\{T\}. \quad (50)$$

The chosen computational software for the FE implementation (ANSYS®) uses Galerkin's method. Therefore, taking into account [22] and applying the Galerkin's method to equation (6), combined with equation (4), the following equation may be obtained:

$$\int_V \left(\frac{\partial q''_x}{\partial x} + \frac{\partial q''_y}{\partial y} + \frac{\partial q''_z}{\partial z} - \dot{q} + \rho c_p \frac{\partial T}{\partial t} \right) N_i dV = 0 \quad (51)$$

From the application of the divergence theorem to the expression given above, one obtains equation (52).

$$\int_V \rho c \frac{\partial T}{\partial t} N_i dV - \int_V \left[\frac{\partial N_i}{\partial x} \frac{\partial N_i}{\partial y} \frac{\partial N_i}{\partial z} \right] \{q''\} dV = \int_V \dot{q} N_i dV - \int_S \{q''\}^T \{n\} N_i dS, \quad (52)$$

where $\{n\}$ (vector of the body surface normal) and $\{q''\}$ are given by:

$$\{q''\}^T = \{q''_x \ q''_y \ q''_z\}; \quad (53)$$

$$\{n\}^T = \{n_x \ n_y \ n_z\}. \quad (54)$$

Applying the boundary conditions to equation (52) leads to the desired discretized equation:

$$\begin{aligned} & \int_V \rho c \frac{\partial T}{\partial t} N_i dV - \int_V \left[\frac{\partial N_i}{\partial x} \frac{\partial N_i}{\partial y} \frac{\partial N_i}{\partial z} \right] \{q''\} dV \\ &= \int_V \dot{q} N_i dV - \int_{S_1} \{q''\}^T \{n\} N_i dS + \int_{S_2} q''_s N_i dS \\ & \quad - \int_{S_3} h(T - T_e) N_i dS - \int_{S_4} (\sigma \varepsilon T^4 - \alpha q''_r) N_i dS, \end{aligned} \quad (55)$$

being $\{q''\}$ calculated by equation (56).

$$\{q''\} = -k[B]\{T\}. \quad (56)$$

According to [21] and [22], equation (55) can be expressed as follows:

$$[C]\{\dot{T}\} + [K_T]\{T\} = \{R_T\}, \quad (57)$$

where $[C]$ is the global specific heat matrix, $[K_T]$ the global thermal conductivity matrix and $\{R_T\}$, $\{T\}$ and $\{\dot{T}\}$ the vectors of thermal loads, temperature and first temperature derivative, respectively.

The matrix $[K_T]$, taking into account [22], can also be written as follows:

$$[K_T] = [K_k] + [H_{conv}] + [H_{rad}], \quad (58)$$

where $[K_k]$, $[H_{conv}]$ and $[H_{rad}]$ are the global matrices of conduction, convection, and radiation.

The vector $\{R_T\}$ is, according to [21], composed by:

$$\{R_T\} = \{R_B\} + \{R_{conv}\} + \{R_{h_{rad}}\} + \{R_{\dot{q}}\}, \quad (59)$$

In equation (59), $\{R_B\}$, $\{R_{conv}\}$, $\{R_{h_{rad}}\}$ and $\{R_{\dot{q}}\}$ represent the global vectors of heat flow, convection, radiation and heat generation, respectively.

Note that in this dissertation the FEAs are nonlinear, which results from the non-negligence of the radiation (between bodies and the enclosure) as well as from considering that the properties of the material are a function of temperature. It will also consider the conduction (inside the material) and convection (in the water of the refrigeration system).

2.2.2. Finite Elements in ANSYS®

In ANSYS®, the computational software used in this dissertation for the FEA, are available numerous types of FEs, from 1D to 3D, as well as the number of nodes and degrees of freedom associated to each of these. Hence, the various FEs used in this dissertation presented below are partially extracted from [23].

SOLID90 is a 3D element with 20 nodes in which each of these nodes have only one degree of freedom corresponding to the temperature, as shown in Figure 16. It should be noted that this is an element commonly known for its utility and flexibility in curved boundary modeling.

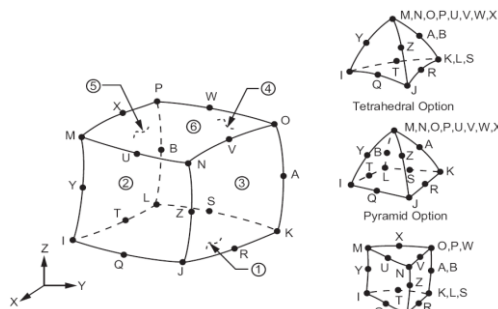


Figure 16 - SOLID90 element geometry [23].

SHELL131 is a 3D shell element with 4 nodes, each of which can be provided with a maximum of 32 degrees of freedom one of which is the temperature. This element may also be divided into layers as shown in Figure 17.

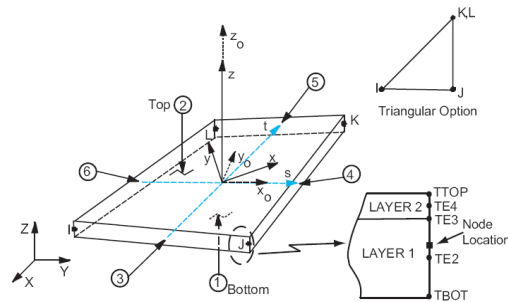


Figure 17 - SHELL131 element geometry [23].

With respect to SURF152, illustrated in Figure 18, its use focuses on the various types of loads applied to a surface, such as convection. Any face of a 3D thermal element can be overlaid with it, which makes it an element widely used in thermal analysis.

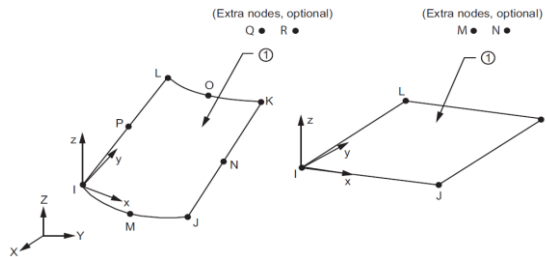


Figure 18 - SURF152 element geometry [23].

For the case of radiation, the element used is SURF252 and it is shown in Figure 19. This element may only be used with the radiosity solver method and can overlap any solid 3D thermal element, or even shell, allowing the use of temperature as degree of freedom.

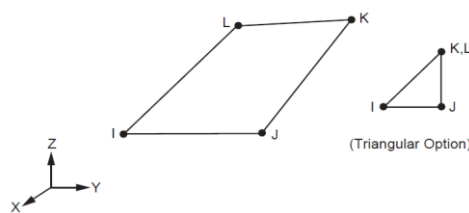


Figure 19 - SURF252 element geometry

Finally, FLUID116, see Figure 20, is a 3D element that can conduct heat and transfer fluid between two nodes. This element has a heat flow associated due to the convection induced and the mass transport of the fluid.

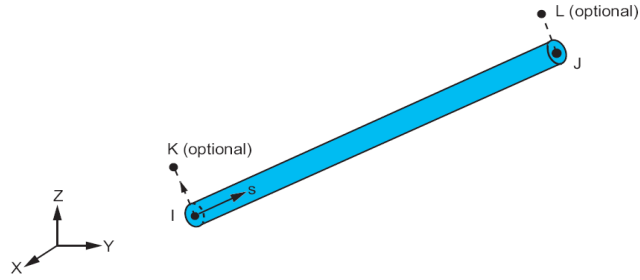


Figure 20 - FLUID116 element geometry [23].

The simultaneous use of FLUID116 with SURF152, allows accounting and analyzing the effects of convection. Note that SURF152 can have two types of degrees of freedom, namely temperature and pressure.

2.3. Fluid Flow

In this dissertation, for the numerical analyses of the fluid flow, ANSYS®Fluent CFD software is used. It solves partial differential equations, in a control volume, based on the finite volume method and uses the SIMPLE algorithm [25].

2.3.1. Governing Equations

The governing equations that follow are written for a Newtonian fluid and are extracted from [25] and [26].

The mass conservation equation may be expressed as:

$$\frac{\partial \rho}{\partial t} + \nabla \cdot (\rho \vec{U}) = 0, \quad (60)$$

where \vec{U} is the velocity and ρ the fluid density.

For incompressible fluid ($\frac{\partial \rho}{\partial t} = 0$), the mass conservation equation is reduced to:

$$\nabla \cdot \vec{U} = 0. \quad (61)$$

The transport of momentum or Navier-Stokes equation may be expressed as:

$$\frac{\partial \vec{U}}{\partial t} + \vec{U} \cdot \nabla (\rho \vec{U}) = -\nabla p + \nabla \cdot \bar{\tau} + \rho \vec{g} + \vec{F}, \quad (62)$$

being p the static pressure, $\bar{\tau}$ the stress tensor, $\rho \vec{g}$ the gravitational body force and \vec{F} the other source terms that may arise from resistance and sources. If p is related to the relative local hydrostatic pressure, the gravitational body force term does not appear in the equation (62).

The stress tensor ($\bar{\tau}$), presented in the previous equation may be expressed as:

$$\bar{\tau} = \mu [(\nabla \vec{U} + \nabla \vec{U}^T) - \frac{2}{3} \nabla \cdot \vec{U} I], \quad (63)$$

where μ is the molecular viscosity in $\left[\frac{Kg}{s \cdot m}\right]$ and I is the unit tensor.

For incompressible fluid and considering equation (61), equation (63) may be rewritten as:

$$\bar{\tau} = \mu(\nabla\vec{U} + \nabla\vec{U}^T), \quad (64)$$

as an incompressible fluid is not bound to volume dilation.

The last of the governing equations is the energy equation (considering that viscous dissipation is neglectable):

$$\frac{\partial}{\partial t}(\rho h_{en}) + \nabla \cdot (\rho h_{en} \vec{U}) = \nabla \cdot [(k + k_t)\nabla T] + S_h, \quad (65)$$

where k is the molecular conductivity, k_t is the conductivity due to turbulent transport ($k_t = c_p \mu_t / Pr_t$), in $\left[\frac{W}{mK}\right]$, and the source term S_h includes any volumetric heat sources, in $\left[\frac{W}{m^3}\right]$.

The aforementioned energy equation is written in terms of sensible enthalpy for a defined reference temperature ($T_{ref} = 298.15 K$), h_{en} $\left[\frac{J}{Kg}\right]$ as:

$$h_{en} = \int_{T_{ref}}^T c_p dT. \quad (66)$$

For problems under steady state conditions, the time dependent parameters, in the equations above shall not be considered.

2.3.2. Turbulence Models

Turbulence models in ANSYS®Fluent are based on Reynolds averages of the governing equations. The variables like velocity, pressure and other scalar quantities are decomposed into the mean (ensemble-averaged or time-averaged) and fluctuating components:

$$u_i = \bar{u}_i + u'_i, \quad (67)$$

$$\varphi = \bar{\varphi} + \varphi'. \quad (68)$$

In the previous equations u_i , \bar{u}_i and u'_i represent the instantaneous velocity, mean velocity and the fluctuations, respectively, and φ represents the pressure or other scalar quantities.

This decomposition is implemented in the governing equations after which, the resulting equations are submitted to a temporal average leading to the appearance of new terms, especially in the transport of momentum and energy equations. The continuity equation is linear hence, it is satisfied by the use of mean components as well as the fluctuations, so it does not change.

It is important to notice that during the implementation of the time average, the fluctuation average is null. For the transport of momentum equations, the new term represents the Reynolds Stresses:

$$-\rho \overline{u'_i u'_j}. \quad (69)$$

After analyzing all the equations, it is found that the number of variables is greater than the number of equations. Hence, additional studies were necessary to model turbulence which lead to the development of turbulence models.

The focus of the turbulence models is on the proper modelling of the Reynolds stresses. Knowing that, the first turbulence model was proposed by Boussinesq in 1877, [25] in which was concluded that the Reynolds stresses could be written in relation to a fictitious viscosity, the turbulent viscosity, also called eddy viscosity (μ_t) which is a characteristic of the flow and not of the fluid. Therefore, for incompressible flow the Reynolds' stresses can be expressed as follows:

$$-\rho \overline{u'_i u'_j} = \mu_t \left(\frac{\partial \bar{u}_i}{\partial x_j} + \frac{\partial \bar{u}_j}{\partial x_i} \right). \quad (70)$$

In 1925, Prandtl presented an equation for μ_t inspired in the kinetic gas theory. This equation describes the Eddy viscosity as a function of two scales, velocity (v_t) and characteristic length of the turbulent field, being these two related to the mixing length (l_m):

$$\mu_t = \rho v_t l_m. \quad (71)$$

Years later, the velocity scale changed to the square of the turbulent kinetic energy and with one more partial differential equation, the one equation turbulence models was presented and now the system has no longer more variables than equations. After the single equation turbulence models, appeared the two equation models and one of the most successful was the Launder k_ϵ model, [25].

The difference is that in the k_ϵ model the length scale gives way to a time scale that multiplied by the velocity scale produces a length unit quantity, therefore, the two scales are determined independently. This time scale, characteristic of the big swirls, is reproduced by the ratio $\frac{k_{sw}}{\epsilon_{diss}}$, being ϵ_{diss} the dissipation ratio. With this, the eddy viscosity may be computed by:

$$v_t = \frac{\mu_t}{\rho} = C_\mu \frac{k_{sw}^2}{\epsilon_{diss}}, \quad (72)$$

where C_μ is a constant with the value of 0.09.

Based in the Launder k_ϵ model, two more k_ϵ turbulence models appeared namely, the RNG k_ϵ model and the Realizable k_ϵ model.

The RNG k_ϵ model is derived from the instantaneous Navier-Stokes equations using a mathematical technique called renormalization group methods. According to [24] it is similar to the standard k_ϵ model, including one additional term in the ϵ_{diss} equation for the interaction between turbulence dissipation and mean shear, the effect of swirl on turbulence, analytical formula for turbulent Prandtl number. Hence, this model has improved predictions for high streamline curvature and strain rate, transitional flows, separated flows and wall heat and mass transfer. This last improvement is one of the reasons why the RNG k_ϵ model is chosen for this dissertation which is reinforced by the fact that it is a commonly used approach in similar works,

e.g., [27], [28].

Note that, according to [26], k_ε models are valid only for turbulent flows and requires wall function implementation. More information about the transport equations and the turbulent viscosity for the RNG k_ε model is presented in [26]. The convective heat transfer in the k_ε models, in ANSYS®Fluent [24], is modeled using the concept of Reynold's analogy to turbulent momentum transfer. Hence, it can be written as follows:

$$\frac{\partial}{\partial t}(\rho E_{tot}) + \frac{\partial}{\partial x_i}[u_i(\rho E_{tot} + p)] = \frac{\partial}{\partial x_i}\left(k_{eff} \frac{\partial T}{\partial x_i}\right) + S_h, \quad (73)$$

where E_{tot} in $\left[\frac{J}{kg}\right]$ is the total energy and k_{eff} is the effective conductivity.

Note that k_{eff} calculation differs between k_ε models. For the standard k_ε this value is calculated using equation (74) and for the RNG it is calculated using equation (75):

$$k_{eff} = k + \frac{c_p \mu_t}{Pr_t} \quad (74)$$

$$k_{eff} = \alpha c_p \mu_{eff} \quad (75)$$

being $Pr_t = 0.85$, α the inverse effective Prandtl number and μ_{eff} the effective viscosity.

The effective viscosity and the inverse Prandtl number may be expresses as:

$$\mu_{eff} = \mu + \mu_t, \quad (76)$$

$$\left| \frac{\alpha - 1.3929}{\alpha_0 - 1.3929} \right|^{0.6321} \left| \frac{\alpha + 2.3929}{\alpha_0 + 2.3929} \right|^{0.3679} = \frac{\mu}{\mu_{eff}}, \quad (77)$$

where $\alpha_0 = 1/Pr_t$.

Close to the wall, viscous damping reduces the tangential velocity fluctuations while, kinematic blocking reduces the normal fluctuations. Toward the outer part of the near-wall region, the turbulence is rapidly augmented by the production of turbulent kinetic energy due to large gradients in the mean velocity.

The near-wall region (inner layer) can be subdivided into three layers. In the innermost layer (viscous sublayer) the flow is laminar and the molecular viscosity plays a dominant role in the momentum and heat or mass transfer. However, in the outer layer (fully-turbulent layer or log-law region), turbulence plays a major role. In the interim region, between the previous layers, the effects of molecular viscosity and turbulence are equally important.

To more accurately treat the flow near the wall the enhanced two-equation models that combine enhanced wall treatment with the k_ε models is used. Enhanced wall treatment is a near-wall modeling method that combines a two-layer model with enhanced wall functions.

In the two-layer model, the viscosity-affected near-wall region is completely resolved until the viscous sublayer. The two-layer approach is an integral part of the enhanced wall treatment and is used to specify both ε_{diss} and the turbulent viscosity in the near-wall cells. Hence the whole domain is subdivided into a viscosity-affected region and a fully-turbulent region, [24].

2.3.3. Pressure Drop in Channels

In addition to what was previously mentioned in § 2.1.2 about internal flow, it is relevant to quantify the existing head losses due to the importance of determining the pressure drop necessary to maintain the flow.

The pressure-drop in channels is obtained using the energy equation and the first law of thermodynamics applied between the channel inlet and outlet. Considering the same volumetric flow and flow velocity through all the channel, no pumps, no turbines and incompressible flow, the energy equation reduces to:

$$\frac{p_1}{\rho g} + \frac{v_1^2}{2g} + z_1 = \frac{p_2}{\rho g} + \frac{v_2^2}{2g} + z_2 + h_f \quad [m], \quad (78)$$

where p_i is the pressure in $[Pa]$, v_i is the flow velocity in $\left[\frac{m}{s}\right]$, g is the gravitational acceleration in $\left[\frac{m}{s^2}\right]$, z_i is the height of the inlet and outlet in $[m]$ and h_f the head loss in $[m]$, [29].

Also, considering that the flow velocity is the same through all the channels ($v_1 = v_2$) and using the Navier-Stokes equation [15], it is possible to relate h_f with the wall friction (τ_0) which is the source of the pressure drop. From this relation is obtained the Dracy-Weibach law:

$$h_f = f \frac{\Delta L}{D} \frac{v^2}{2g}, \quad (79)$$

being f the Darcy coefficient or the friction factor, ΔL the channel length in $[m]$ and D the channel characteristic diameter in $[m]$, [29].

The Darcy coefficient can be obtained using the Moody diagram, knowing the Re_D and the roughness of the channel wall in $[m]$, which for commercial stainless steel can be approximately $0.005 m$, [15].

Apart from the head losses due to friction on the walls, there are other factors that contribute to the pressure drop, the local losses. Local losses can occur in channel entrance, bends, elbows and others. Knowing this, the total losses may be expressed as:

$$h_{tot} = \frac{v^2}{2g} \left(f \frac{\Delta L}{D} + \sum_i K_i \right), \quad (80)$$

where K_i is the dimensionless local loss coefficient that may be obtained using empirical and/or numerical expressions or even plots, as those present in the chapter 6 of [15].

Hence, considering all the assumptions and equations previously presented, the following equation for the pressure drop is obtained:

$$\Delta p = p_1 - p_2 = \rho g (\Delta z + h_{tot}) \quad [Pa]. \quad (81)$$

With this, a brief introduction to the fundamentals needed for this dissertation has been presented. Next, the methodologies developed and used to address the problem considered in this dissertation are described.

3. Methodology

In this chapter are described the methodologies developed and used are described. It initially includes two simple verification models, followed by a description of the steady state and transient thermal FEA methodologies applied to the launcher and receiver ITER CTS mirrors. Additionally, a CFD steady state analysis, using ANSYS®Fluent, is conducted to verify the used convection coefficients and the pressure drop inside of the cooling channels.

3.1. Verification Models

Before proceeding to the FEA of the mirrors, two verification models are introduced to verify the implementation of the fundamental concepts, e.g., radiosity solver. The verification is conducted by comparing the numerical and analytical solutions obtained.

3.1.1. Convection Model

The first verification model regards the study of heat transfer by convection. For that, it is considered a parallelepiped, of length L , with a center hole of diameter D , as shown in Figure

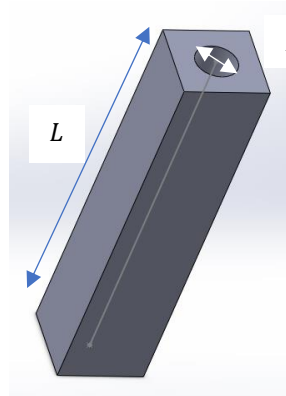


Figure 21 - CAD model of a parallelepiped of length L with center hole of diameter D .

21.

The center hole allows the flow of water, with an initial temperature of $T_{m,i}$ and a specific pressure, p . On one side of the parallelepiped (lateral wall) is imposed a heat power of P while the other sides are considered adiabatic.

The resolution of the problem in question consists of the calculation of the water outlet temperature, $T_{m,o}$, as well as the average hole surface temperature T_s of the parallelepiped, using equations (17) and (8).

3.1.1. Thermal Radiation Model

The second verification model focuses on heat transfer by thermal radiation. The goal is to assess the accuracy of ANSYS® shape factor and radiosity solver calculations.

For it, two irradiating surfaces with temperatures, T_1 and T_2 , spaced by a distance L are considered, at an environment temperature T_{amb} , as illustrated by Figure 22. In addition, each of

the surfaces has a distinct emissivity, ε_1 and ε_2 .

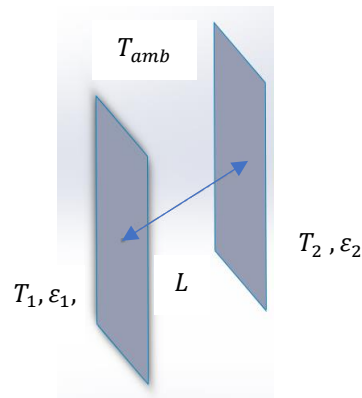


Figure 22 - CAD model of two irradiating surfaces considered for the radiation problem.

The resolution of this problem consists of calculating the net flux, the emissive and the irradiation power for each surface, using equations (26), (21) and (37) respectively, as well as the respective view factors.

3.2. Launcher Mirror

3.2.1. Microwaves Radiation Beam Power Distribution

The microwave radiation from the gyrotron is incident on the launcher mirror with a distribution expressed by equation (40). As it represents a Gaussian power distribution on the face of the launcher mirror, the calculations of the shape of the isolines and the power between each one are performed using a software developed, in this dissertation, using MATLAB®¹.

In Figure 23 the input panel with the required input data so that the specifications of the isolines can be computed.

Valor de Potência Total (Ptot) em MW:	1
Valor da largura do feixe incidente (wx) em mm:	62.9
Valor da largura do feixe incidente (wy) em mm:	50
Valor máximo de x em mm:	100.7
Valor máximo de y em mm:	80
Nº de isolinhas pretendidas:	6

Figure 23 - Input data panel for the isolines estimation.

The field “Valor de Potência Total (Ptot) em MW” is where it is inserted the value of P_{tot} . In the field “Valor da largura do feixe incidente (wx) em mm” is where the value of the width w_x of

¹ The routine is presented in the appendix A.1.

the incident beam is inserted and in the “*Valor da largura do feixe incidente (w_y) em mm*” is where the other dimension (w_y) of the beam is inserted. In the field “*Valor máximo de x em mm*” is where the maximum radius of the ellipse that defines the outer part of the mirror, is inputted and in “*Valor máximo de y em mm*” is where to insert the minimum radius of the ellipse. Finally, in the field “*Nº de isolinhas pretendidas*” is where the required number of isolines is inserted. To better understand these data values, see equation (40).

With this software, it is possible to define the isolines and improve the cooling system imposed on the launcher mirror.

3.2.2. CAD Model Design

The CAD model of the launcher mirror is developed in CATIA®. All the dimensions as well as the position of the mirror (located in drawer 3 of equatorial port 12 [9]) are accessed using ENOVIA® (CAD data base).

The first step consists of modelling the launcher mirror using surfaces and then the CATIA command “Close Surface” is used to create the solid geometry in which, the cooling channel geometries are designed.

To model the cooling channel geometries, the CATIA command “Sweep” is used to produce the surface of the cooling channel recurring to a center curve that defines its shape. Next, it is used the command “Close Surface” to create a solid that represents the cooling channel which, is then followed by the command “Remove” to subtract the solid channel components from the mirror. In Figure 24 is illustrated, in a simplified manner, some steps of this process.

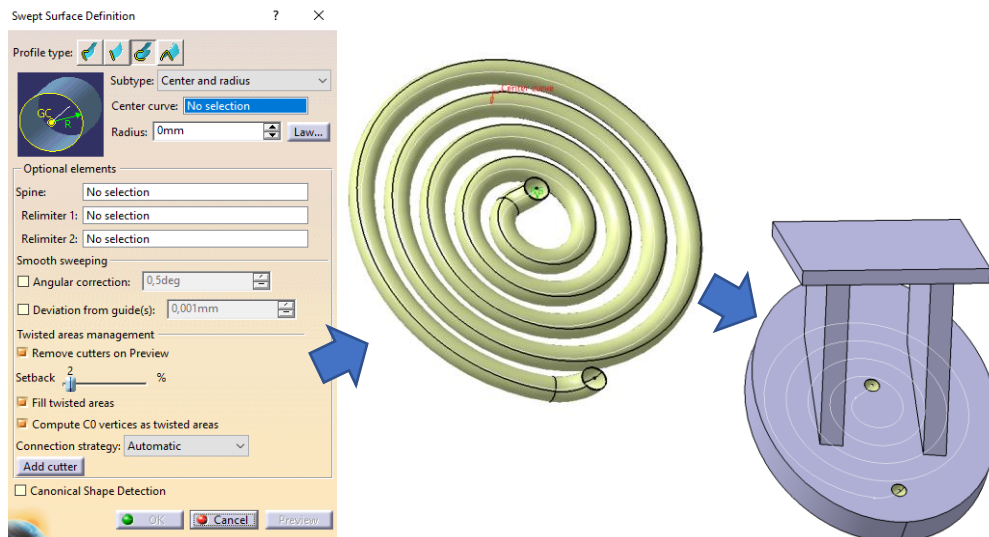


Figure 24 - Some steps used in the CAD modeling of a cooling channel.

As the supports of the mirror do not exist in ENOVIA®, they are here designed in a very simplified manner and without any structural assessment considerations. However, the location (drawer 3 of equatorial port 12 [9]) and enclosure (see simplified model in Figure 25) of the launcher mirror are known.

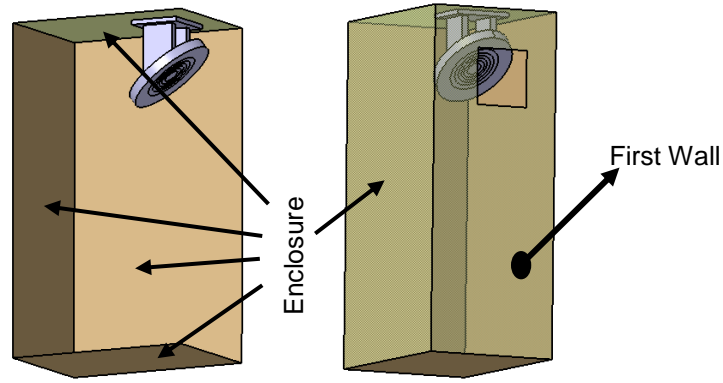


Figure 25 - CAD models of the launcher mirror and enclosure.

With respect to the launcher mirror design, note that the reflective surface is divided in areas, as shown in the Figure 26. These areas are necessary to enable the radiation beam power distribution implementation in ANSYS®Mechanical. Moreover, those surfaces are limited by the isolines that are computed using the methodology described in § 3.2.1. To incorporate the isolines into the mirror, the CATIA command “*Projection*” is used.

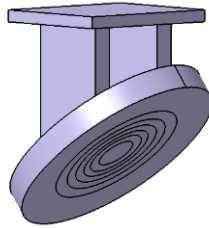


Figure 26 - CAD model of the launcher mirror without cooling channels.

For the launcher mirror, the dimensions considered are the thickness at the reflective surface lowest point (being this surface concave), that has the value of 20 mm and the mirror outline defined by an ellipse with the largest and smallest radius equal to 100.7 mm and 80 mm, respectively.

3.2.3. Steady State Thermal FEA

Although the fusion reaction inside the tokamak is expected to last for 400 seconds, in a first approach, a steady state thermal FEA is performed in which, the maximum and minimum mirror and water (cooling fluid) temperatures achieved are estimated.

3.2.3.1. Mesh Convergence

Initially, a mesh convergence analysis is conducted for the steady state thermal FEA. It consists of a parametric analysis in which, the parameter considered is the FE size used in the mesh which, may assume four of the following values per each parametric analysis: 5 mm; 4 mm; 3 mm; 2.5 mm and; 2 mm.

In this dissertation, only meshes with a convergence deviation below 1% are considered.

3.2.3.2. Mirror Made of SS 316 L(N)-IG

The material for the launcher mirror required by ITER is SS 316 L(N)-IG. Thus, it is the first material to be considered and only then, two other materials (copper and tungsten) are contemplated.

Initially, a study on how to model, the plasma heat flux of $q''_{plasma} \left[\frac{kW}{m^2} \right]$, according to [30], and the heat flux due to stray radiation ($q''_{stray} \left[\frac{kW}{m^2} \right]$), as mentioned in [31], using ANSYS® Mechanical is conducted. This will assist in deciding if the corresponded heat fluxes may be approximated by a surface, at a certain temperature, emitting the correspondent thermal radiation heat flux which, minimizes the computational effort required for the analyses.

Assuming that the plasma is surrounded by the first wall of the tokamak, see Figure 25, which has an approximate temperature of 450 °C, and that the radiation surface is part of the first wall, the surface temperature may be computed using equation (38). In addition, the radiation surface is considered a black surface. The radiation surface considered is illustrated in the Figure 27 and is related to the existing opening (illustrated in red) that enables the emission of the microwave beam to the plasma.

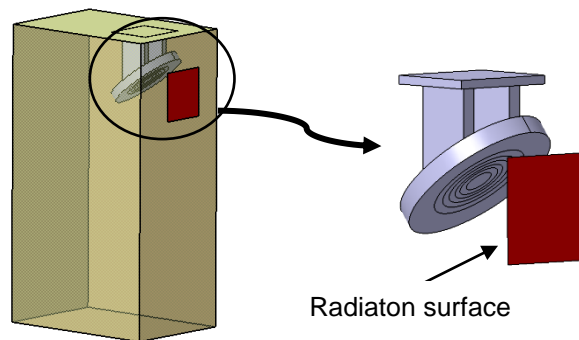


Figure 27 - CAD model and localization of the radiation surface (in red) used to model the plasma radiation and stray radiation emission.

Afterwards, an initial thermal FEA of the mirror without a cooling system is conducted to verify that cooling is required as the maximum temperature exceeds the corresponding operation temperature (~450°C), as indicated in [32].

To identify the most significant thermal load, it is simulated, in ANSYS®Workbench, the thermal response of the mirror to the thermal loads separately, i.e., just radiation from the plasma and then just the power absorbed due to the microwave beam. Note that the nuclear heat load distribution induced by the neutrons coming from plasma and surrounding materials, is taken into account as internal heat generation. These nuclear heat loads are estimated using the Monte Carlo simulation program MCNP6 and reference neutronics models provided by ITER Organization, according to [33]. Only then, the different thermal loads are implemented simultaneously to simulate the combined load cases.

The data required for this analysis is the microwave radiation beam power distribution, the temperature values of the intervenient surfaces as well as the emissivity values of each of the surfaces. The emissivity values for SS 316L(N)-IG, withdrawn from [30], are illustrated in Figure 28. The fraction of power absorbed by the mirror, due to the microwave beam, is estimated by equation (41), using the values from the tables presented in the appendix A.2 Except for the plasma surface (that is considered as a black surface, as previously mentioned) the emissivity and absorption values of all other intervenient surfaces are expressed by equation (31) as they are considered gray surfaces.

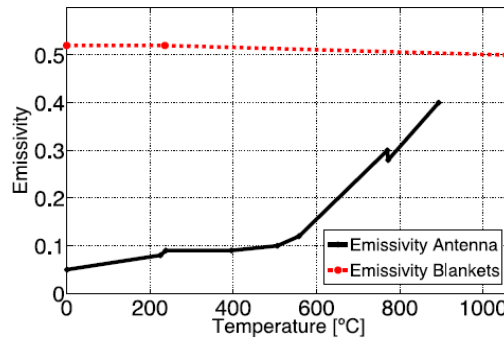

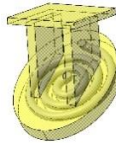
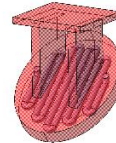
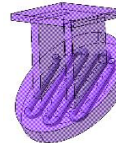
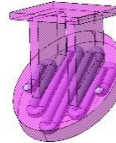
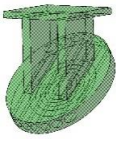
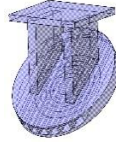
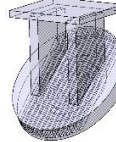
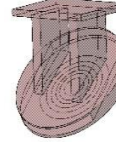
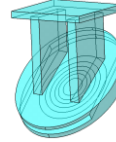


Figure 28 - Emissivity as a function of the temperature for unpolished (Blankets) and polished (Antenna) components made of SS 316L(N)-IG [30].

Based on the assumption that a cooling system is required, the next step is to assemble the FEA for 10 different cooling system channel geometries, see Table 3, considering as design variables the convection area, the convection coefficients and the material volume of the mirror after the cooling system channel geometries are implemented.

Table 3 - CAD models of the launcher mirror with different cooling channel geometries.

				
SPIRAL_D_10MM	SPIRAL_D_14MM	ZIGZAG_D_10MM	ZIGZAG_D_10MM_ CURTO	ZIGZAG_D_14MM
				
7_D_14MM	7_14X14	13_14X5	1_RETAN_120X14	1_RETAN_120X10

Initially, one needs to import the CAD geometry from CATIA® into ANSYS®Workbench, by activating the “import body lines” in ANSYS®DesignModeler so that the centerline of the cooling channel is imported. Note that, in ANSYS®DesignModeler, the channel geometry is defined recurring to the centerline of the channel for which, FLUID116 FE is considered.

Some of the boundary conditions assumed in this analysis are similar to those used in

the previous one (see initial thermal FEA of the mirror without a cooling system conducted to verify that cooling is required). However, for the fluid flow modelling, the following new boundary conditions need to be defined: mass flow rate; water initial temperature and; convection coefficient.

According to [16], the maximum mass flow rate of water available for the ITER-CTS components is $1.5 \left[\frac{Kg}{s} \right]$ and this mass flow rate can be used in series or in parallel, meaning that the same cooling fluid can be used in all the cooling systems implemented in this CTS system or it can be divided by each cooling system, respectively. Also, the mean water temperature inside of the tokamak is considered to be $\sim 70^{\circ}C$, which is considered to be the initial water temperature. As the water must always be in liquid state and knowing that the water pressure is $4.0 MPa$, the maximum water temperature achieved shall not exceed $150^{\circ}C$, according to [34]. Additionally, the maximum pressure drop in the channels shall not exceed $1.35 MPa$, as mentioned in [35].

To assure that the pressure drop inside the channels, due to the friction losses and local losses in the elbows, is not greater than the aforementioned value ($\sim 1.35 MPa$), simple estimations, see § 2.3.3, may be conducted in order to verify the cooling channel geometries.

Knowing the mass flow rate and the hydraulic diameter, defined by equation (10), the Reynolds number may be computed using equation (9). With the Reynolds number, the Nusselt number, given by equation (19), and Prandtl number², the convection coefficient may be obtained using equation (20), for each different cooling channel geometry.

The goal of this analysis is not just to make a comparison between different channel geometries but also to understand the effect of having different mass flow rates, in each arrangement and for the case of using parallel flow distribution. Therefore, for the last one a parametric analysis in ANSYS®Workbench is conducted where the parameters considered are the mass flow rate and the convection coefficient.

3.2.3.3. Other Materials Considered for the Mirror

The methodology described above also applies to the cases in which the mirror is made of one of two other materials, i.e., copper and tungsten. When considering these materials, one has to consider the respective surfaces emissivity and power absorbed fraction³ of the mirror. Furthermore, according to [36], it is considered that the material operation temperature for copper is between $77^{\circ}C$ and $87^{\circ}C$ and for tungsten is between $825^{\circ}C$ and $1210^{\circ}C$.

Although the power absorbed fraction has different values for each material, the values considered here are estimated using the highest known electrical resistivity of the materials, leading to a conservative approach.

With this analysis, a performance comparison of the different channel geometries for each

² Related with water properties and calculated for average water temperature inside the channel.

³ A is dependent of ρ (electrical resistivity) which is a material property.

material is conducted. In addition, a comparison between SS 316 L(N)-IG and these two materials is performed to assess their suitability as alternative materials, with respect to the maximum body temperature achieved under similar conditions and/or to avoid some of the problems manifested with the use of SS 316 L(N)-IG, like the low thermal diffusivity capering to copper and tungsten.

3.2.4. Transient Thermal FEA

A transient thermal FEA is performed using one of the optimum channel geometries (according to the steady state FEA) for the SS 316L(N)-IG mirror, in order to establish when steady state is achieved, considering the duration of burn phase (when the plasma emits radiation) and the dwell time. This permits to verify if the mirror is subjected to better temperature conditions during a real situation comparing with the ones where steady state conditions are assumed.

Additionally, the cooling time of the mirror during the dwell time having the cooling system shut off is compared to the one when it is turned on.

This analysis accounts for the same boundary conditions and mesh as those considered for the steady state analysis.

Step Controls	
Number Of Steps	1,
Current Step Number	1,
Step End Time	2200, s
Auto Time Stepping	Off
Define By	Time
Time Step	10, s
Time Integration	On
Solver Controls	
Solver Type	Program Controlled
Radiosity Controls	
Nonlinear Controls	
Output Controls	
Analysis Data Management	
Visibility	

Figure 29 - Step controls for the transient FEA in ANSYS®Mechanical.

The differences are the actuation time of the microwave beam, internal heat generation and plasma radiation, due to the dwell time phase, and the analysis setting in ANSYS®Mechanical, see Figure 29.

3.3. Receiver Mirror

The receiver mirror is developed in CATIA® and it has the following position in the drawer 3 of the tokamak equatorial port 12 [9], see Figure 30.

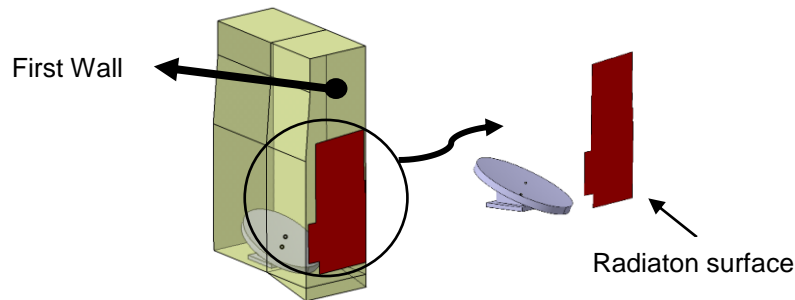


Figure 30 - CAD model and localization of the receiver mirror and of the surface (in red) used to model the plasma radiation and stray radiation emission.

For the receiver mirror, the dimensions considered are the thickness at the reflective surface lowest point (since this surface is concave) that has the value of 20 mm and; the mirror outline defined by an ellipse with the largest and smallest radius equal to 190 mm and 140 mm, respectively. Also, SS 316 L(N)-IG is the material required by ITER for the mirrors.

Similar approaches, methodologies, assumptions and simplifications are used here as those used for the launcher mirror. The main difference, in terms of boundary conditions, is that the receiver mirror does not have any incident microwave beam.

3.4. Steady State Fluid Flow Thermal Analysis

A steady state fluid flow thermal analysis is performed to verify the convective coefficients used for the thermal FEA performed in this dissertation. In addition, it is conducted a study related to the pressure drop inside the cooling channels that should be lower than 1.35 MPa. It is expected to verify the results tendency obtained with the analytically calculations of the pressure drop presented in § 3.2.3.

Note that not all cooling channels geometries are studied. For the launcher mirror are considered ZIZAG_D_10MM and 1_RETAN_120x14 and for the receiver mirror are considered ZIZAG_D_14MM and 1_RETAN_240x14. The flow rates previously mentioned in § 3.2.3, are considered and with those it is possible to estimate one of the inputs required for this analysis, i.e., the inlet fluid velocity u_m computed with equations (9) and (10), being the other the outlet gauge pressure.

The turbulence model considered, see § 2.3, is the RNG k_ϵ model. To accurately treat the flow near the wall, it is used a near-wall modeling method that combines a two-layer model with enhanced wall functions, i.e., combine enhanced wall treatment with the k_ϵ models. In short, it is used the RNG k_ϵ model with enhanced wall treatment.

In relation to the residual are considered value of 10^{-6} for the energy equation and 10^{-4} for the others, e.g. the continuity equation, as indicated in [24]. Relatively to the mesh, a refinement is conducted for each mirror and cooling channel geometry considering the mesh point

distribution, smoothness and skewness [24]. The mesh refinement is considered satisfactory when the deviations of the results between each refinement are $< 10^{-2}$ [MPa].

With this, an introduction to the methodologies developed and used in this dissertation has been presented. In the next chapter the main results are presented and discussed.

4. Results and Discussions

In this chapter the main results obtained are presented and discussed. Initially, the verification models results are presented, which are followed by the steady state and transient thermal FEA of the mirrors.

4.1. Verification Models

4.1.1. Convection Model

As mentioned in § 3.1.1, this first model verification is related to the study of heat transfer by convection. Consider a parallelepiped, of length L , with a center hole of diameter D see Figure 21. Table 4 presents the dimensions, flow properties and water properties considered.

Table 4 - Input data used for the heat transfer by convection verification model.

Required dimensions		Flow		Water properties	
L (m)	1	$T_{m,i}$ (°C)	69	ρ (bar)	4.4
D (m)	0.100	\dot{m} ($\frac{Kg}{s}$)	1	k ($\frac{W}{mK}$)	0.604
				ρ ($\frac{Kg}{m^3}$)	997.4
				c_p ($\frac{KJ}{KgK}$)	4.179
				μ ($\frac{Ns}{m^2}$)	289E-6

Considering a value of 236 KW for the power incident on the face of the parallelepiped, as well as a convection coefficient (estimated using equation (19), complemented by equations (9), (16) and (20)), h , of 951.4 ($\frac{W}{m^2K}$), and taking into account the values presented in Table 4, the analytically results for $T_{m,o}$ and T_s obtained are as follows:

- 125.5°C for $T_{m,o}$, resulting from equation (17);
- 886.6°C for T_s , computed using equation (8) where $T_\infty = T_m$, being T_m the representative mean temperature considering the inlet and outlet temperatures of the water.

The $T_{m,o}$ and T_s values obtained using ANSYS®, based on the data previously presented, and using the FEs SOLID90, SURF152 and FLUID116, see § 2.2.2, are as follows:

- 123.7°C for $T_{m,o}$;
- 886.3°C for T_s .

In Figure 31 the tube bore surface temperature distribution and the fluid temperature distribution obtained using ANSYS® considering a FE size of 40 mm are illustrated.

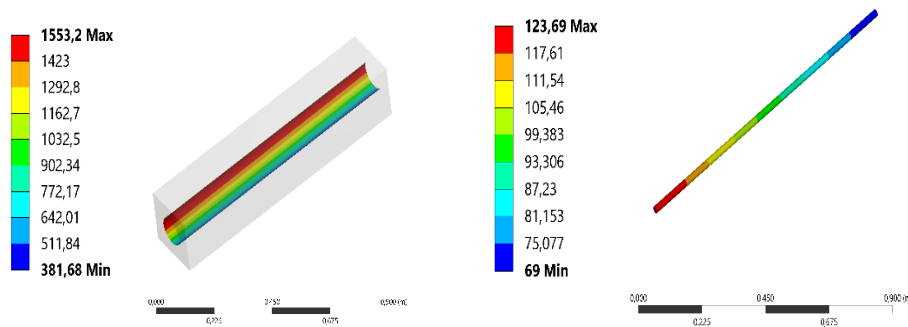


Figure 31 - Numerical results for the heat transfer by convection verification model: left) the tube bore surface temperature distribution and; right) the fluid temperature distribution. Temperature in °C.

From the analytical values and Figure 31, it is possible to verify that the results obtained with the ANSYS® are satisfactorily close to the results obtained analytically, being the maximum deviation approximately 1.4% considering the water outlet temperature computation ($T_{m,o}$).

4.1.2. Thermal Radiation Model

As mentioned in § 3.1.1, the second verification model is related to heat transfer by thermal radiation. For it, consider two surfaces irradiating with dissimilar temperatures (T_1 and T_2) and emissivity values (ε_1 and ε_2), and spaced by L , in an environment at temperature T_{amb} , see Figure 22. The necessary data for the required analysis are presented in Table 5.

Table 5 - Input data used for the heat transfer by thermal radiation verification model.

Surface data				Environment	
Surface 1		Surface 2		T_{amb} (°C)	400
T_1 (°C)	1500	T_2 (°C)	400	ε_1	1
ε_1	1	ε_2	0.80		
Surface dimensions and L distance between them					
L (m)		0.30			
X (m)		0.60			
Y (m)		0.18			

Considering that both surfaces are opaque and gray, thus following the relationship presented in equation (31), the view factor F_{12} may be estimated from Figure 12, registering the value $F_{12} = 0,2$. Hence, considering equation (34), as well as the fact that the area of the two surfaces is the same, one can conclude that $F_{21} = 0,2$. Furthermore, recurring to equation (35), it is possible to infer the value of $F_{13} = F_{23} = 0,8$.

Through the input data listed above, the results analytically obtained for the emissive power, irradiance and net power (surface energy balance in question) are obtained by taking into account equations (21), (37) and (26), respectively, are presented in Table 7.

Table 6 - Analytical results for the heat transfer by thermal radiation verification model.

Analytically					
	View factor	α	E (W)	G (W)	q_{net} (W)
Surface 1	0.108	1	60532.50	1731.55	58801
Surface 2		0.80	1005.88	13112.40	-9484.02

In Table 7 are presented the results obtained through ANSYS®. It is relevant to note that they are obtained using only one element per surface, as illustrated in Figure 32. This decision derives from the fact that the view factor, used in the analytical calculations, does not consider several divisions on the same surface.

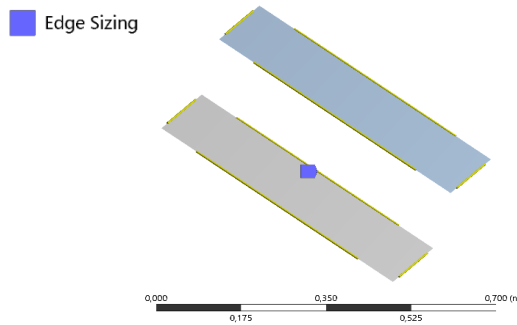


Figure 32 - Second verification model mesh, in ANSYS®MODEL.

Table 7 - Numerical results (ANSYS®) for the heat transfer by thermal radiation verification model.

ANSYS®				
	$F_{12} = F_{21}$	E (W)	G (W)	q_{net} (W)
Surface 1	0.196	60522.0	1860.7	58661.0
Surface 2		1005.7	14969.0	-10969.0

Comparing the results presented in Table 6 and Table 7, one can obtain the deviations between the analytical and the numerical (ANSYS®) results presented in Table 8.

Table 8 - Deviation between analytical and ANSYS® results for the heat transfer by thermal radiation verification model.

Deviations (%)				
	View factor	E	G	q_{net}
Surface 1	~2	~0.017	~7.516	~ 0.238
Surface 2		~0.018	~14.159	~15.658

From the deviations presented in Table 8, it is possible to verify that the view factor has a relevant contribution to the proximity of the solutions and it is important to take into account that the view factor used in the analytical computations is taken from a plot. Furthermore, it is verified that the view factor and the remaining values are satisfactorily close to the analytical ones.

4.2. Launcher Mirror

Next, the main results and respective discussion regarding the analyses of the launcher mirror of the ITER CTS system will be introduced.

4.2.1. Microwaves Radiation Beam Power Distribution

The need to divide the launcher mirror surface into areas that allow for correct representation of the microwave radiation power distribution, ended up in the development of a software routine developed in MATLAB® environment. This routine provides information on the shape of the isolines and the power that will be considered in the area delimited by two isolines.

Figure 33 illustrates the user interface that allows the user to select the inputs (left side of the figure) needed to solve equation (40) by defining the number of isolines. Note that the parameters related to the maximum value in cartesian coordinates represent the dimensions of the launcher mirror, which is the last isoline considered.

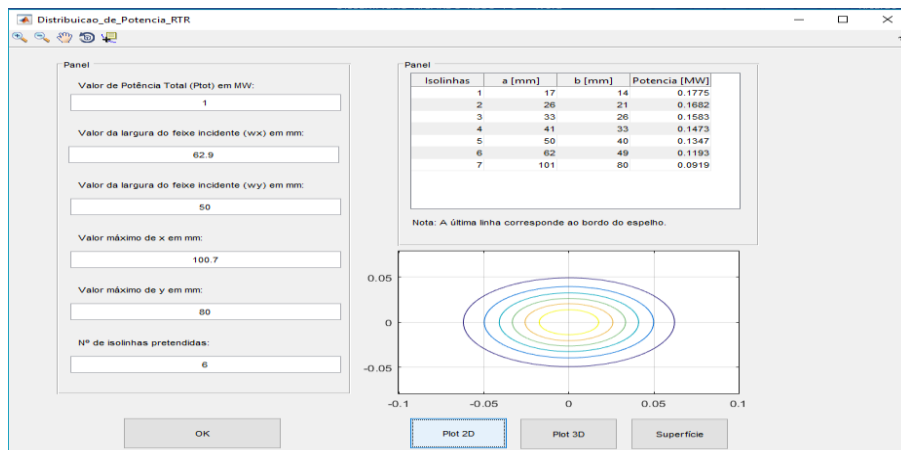


Figure 33 - MATLAB® user input interface to estimate the microwave radiation power distribution in the mirror.

The outputs provided by the routine in question, see Figure 34 and Figure 35, are graphic representation of the shape of the isolines (excluding the edge of the launcher mirror), in 2D and 3D and the surface defined by equation (40).

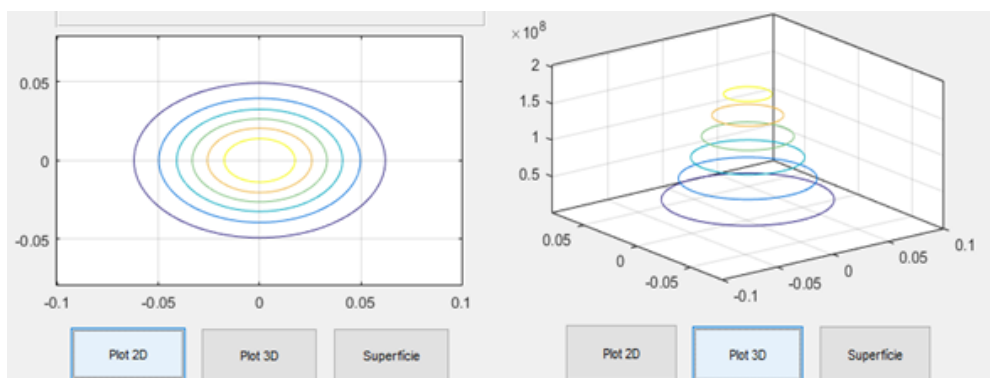


Figure 34 - Isolines representation in 2D and 3D.

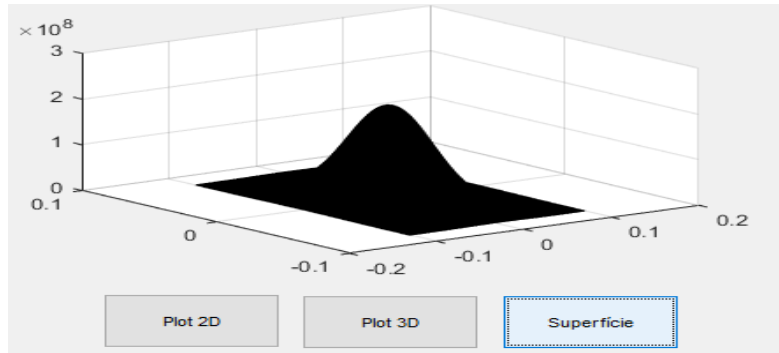


Figure 35 - Surface defined by equation (40).

As can be seen in Figure 34, the isolines are in the form of ellipses. Knowing that the equation of the ellipse is defined by two parameters, a and b , as is verified in equation (82), it is necessary to determine them. Thus, it is provided to the user the value, in millimeters, of the parameters a and b as well as the power between each isoline (in MW), as illustrated in Figure 36.

$$\left(\frac{x}{a}\right)^2 + \left(\frac{y}{b}\right)^2 = 1 \quad (82)$$

Isolinhas	a [mm]	b [mm]	Potencia [MW]
1	17	14	0.1775
2	26	21	0.1682
3	33	26	0.1583
4	41	33	0.1473
5	50	40	0.1347
6	62	49	0.1193
7	101	80	0.0919

Nota: A última linha corresponde ao bordo do espelho.

Figure 36 - Values of parameters "a" and "b" that define the representative ellipses isolines and the value of the power (beam intensity) between each isoline.

From Figure 36, one may observe that the power value is maximum in the center of the mirror and gradually decreases to its minimum value at the edge of the surface, as expected. This confirms an increased concern with the area in question (center area) as the cooling system must have a higher actuation on that exact area do to its larger power gain.

4.2.2. Steady State Thermal FEA

According to the methodology described in § 3.2.3.2, a steady state thermal FEA is carried out to verify the SS 316 L(N)-IG performance, as the material for the launcher mirror, with and without water cooling channels. Therefore, the main results are presented and discussed next, as well as some of other alternative materials considered that may be implemented to mitigate undesirable issues due to the use of the mentioned stainless steel, e.g., the low thermal diffusivity.

4.2.2.1. FE Mesh Convergence

Knowing that temperature values vary with respect to the FE mesh refinement, a convergence study is conducted. As an example, on how this study is performed, the results for the channel cooling geometry 7_D_14MM (see Figure 37) are illustrated in the Figure 38.

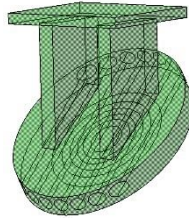


Figure 37 - FE mesh refinement for the cooling channel geometry 7_D_14MM.

Figure 38 illustrates the upper and lower deviation limit, being this deviation calculated relatively to the minimum value obtained for the maximum mirror temperature using different FE sizes, delimiting, in this way, an area in the plot where the deviation is less or equal than 1%.

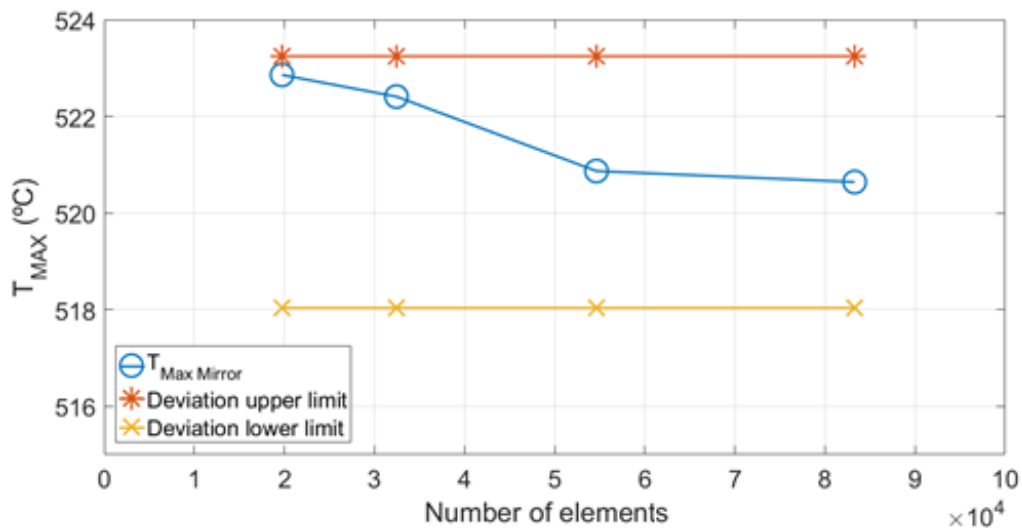


Figure 38 - FE mesh convergence result for the cooling channel geometry 7_D_14MM.

Note that in Figure 38 the number of elements are related to the FE size by the following relations: FE size of 2.5 mm corresponds to 19732 elements; FE size of 3.0 mm corresponds to 32434 elements; FE size of 4.0 mm corresponds to 54633 elements and; FE size of 5.0 mm corresponds to 83286 elements.

From Figure 38, it is possible to verify that all T_{max} points (blue line with circle marks) are in the bounded area. Hence, it is assumed that convergence is achieved with a FE size of 5 mm.

Note that convergence studies are performed for all the other cooling channel geometries, as presented in Table 30 of appendix A.6 in which, a FE size of the 2.5 mm is chosen for those cases.

4.2.2.2. Pressure Drop

Knowing that a cooling system is required, one must assure that it has an acceptable pressure drop in the cooling channels. Hence, it is developed a cooling channel geometry that has the characteristics to present the higher head loss value. Thus, recurring to equation (80) to understand the relation between each variable, one concludes that the chosen cooling channel geometry, from those presented in Table 3, is the ZIGZAG_D_10MM as it has the highest value of ΔL and consequently is more likely to have higher local losses due to its geometry and it has the smallest diameter.

The input data considered for this analysis is:

- Channel diameter ($d = 10 \text{ mm}$);
- Channel length ($\Delta L = 1308.9 \text{ mm}$);
- Channel wall roughness (0.005 mm), value used for commercial stainless steel, as mention in § 2.3.3;
- Number of 180° and 90° elbows (9 and 2 respectively);
- Elbow radius ($R_{180^\circ} = 7.5 \text{ mm}$ and $R_{90^\circ} = 10 \text{ mm}$).

With this information it is possible, using the Moody diagram and the plots concerning local losses on elbows presented in chapter 6 of [15], to determine the friction loss coefficient ($f = 0.03$) and the local loss coefficient ($K_{180^\circ} = 0.33$ and $K_{90^\circ} = 0.22$).

Table 9 presents the pressure drop results for the cooling channel geometry ZIGZAG_D_10MM estimated using equations (9), (80) and (81) complemented by the water properties see Table 13 presented next in § 4.2.2.3.

Table 9 - Pressure drop results for ZIGZAG_D_10MM.

Mass flow rate [Kg/s]	1.50	1.00	0.50	0.25
u_m [m/s]	19.10	12.73	6.37	3.18
Re_d	5.28E5	3.52E5	1.76E5	8.79E4
$p_1 - p_2$ [MPa]	1.33	0.59	0.15	0.04
p_2 [MPa]	2.67	3.41	3.85	3.96

From the results presented in Table 9, one verifies that the maximum pressure drop ($P_1 - P_2$) obtained for the chosen mass flow rates considered in this dissertation, is 1.33 MPa , which is lower than the maximum allowable of 1.35 MPa .

4.2.2.3. Mirror Made of SS 316 L(N)-IG

A first step in this study consists of verifying what is the most adequate method (from a computational effort point of view) to model the heat flux and stray radiation coming from the plasma. Note that it can be modeled directly as a heat flux (computationally heavier) or alternatively as a radiating surface at a specific temperature (computationally lighter). Therefore,

following the methodology presented in § 3.2.3.2, the input data considered follows:

- Heat flux coming from the plasma, $q''_{plasma+stray} = 525 \left[\frac{kW}{m^2} \right]$;
- First wall properties as:
 - $T_{first_wall} = T_{sur} = 450^\circ C$;
 - Black surface, $\varepsilon = \alpha = 1$.

Using equation (38), as mentioned in § 3.4.2, the surface temperature obtained is $T_s \sim 1484^\circ C$. Table 10 presents the incident radiation on the mirror and maximum mirror temperature obtained considering a heat flux and a radiating surface at $T_s \sim 1484^\circ C$.

Table 10 - Implementation of the heat flux and stray radiation from plasma.

	Incident radiation on the mirror [W]	Maximum mirror temperature [°C]
$q''_{plasma+stray} = 525 \left[\frac{kW}{m^2} \right]$	7273.30	2307.30
$T_s = 1484 [^\circ C]$	6997.50	2306.52

From the results presented in Table 10 it is possible to verify that the deviation produced, when considering the radiating surface at $T_s \sim 1484^\circ C$, presents a relative deviation of $\sim 3.79\%$ and a maximum mirror temperature deviation, without any cooling, of $\sim 0.03\%$. This means that to reduce computational effort, the use of a radiating surface at $1484^\circ C$ to model the heat flux due to plasma and stray radiation is a non-compromising approach and is adopted in the following studies.

To study the contribution of the different combinations of thermal loads on the maximum temperature of the launcher mirror, consider the following input data:

- Microwave radiation beam power distribution, presented in Figure 36;
- Mirror microwave power absorbed fraction, $A = 0.56\%$;
- Mirror surrounding surfaces and support base temperature, $150^\circ C$;
- Mirror reflective surface emissivity (polished surface), $\varepsilon = 0.1$;
- Other mirror surfaces emissivity (for $450^\circ C$), $\varepsilon = 0.5$;
- Internal heat generation value, $\dot{q} = 3 \left[\frac{MW}{m^3} \right]$;
- Surface temperature, = $1484^\circ C$, see Figure 27.

Note that the emissivity values (see Figure 28) present low variation (~ 0.01) with the temperature for unpolished surfaces, being 0.5 the value for these cases whereas, for polished surfaces, the emissivity values vary but for the range of temperatures achieved in the mirror reflective surface, the value is almost constant and is here assumed equal to 0.1.

Table 11 presents the maximum temperatures considering the different combinations of thermal loads.

Table 11 - T_{max} [°C] results for the launcher mirror achieved with different combinations of thermal loads.

	T_{max} [°C]
Microwave	1765.70
Stray + Plasma Radiation	887.25
All of the above	2306.52

From Table 11, it is possible to conclude that the microwave beam has more influence in the maximum temperature of the launcher mirror than the combination of the stray and thermal radiations coming from the plasma. Hence, one concludes that the launcher mirror requires a cooling system since $T_{max} = 2306.52$ °C is above the maximum operating temperature of ~450 °C.

The input data previously presented is considered for the analysis where the comparison of the maximum mirror temperature achieved for the 10 different channel geometries, see Table 3, is conducted.

First the results of the convective coefficient (see Table 12) estimated are presented, according the methodology described in § 3.2.3.2, using equation (20). The mean temperature considered for the water inside the channel is estimated as 77.5 °C (which is the average between 70 °C and 85 °C that is the water temperature range assumed in the simulations performed).

The water properties required to compute h , for a mean water temperature of 77.5 °C, are presented in Table 13 and the convective coefficient values for each of the different channel geometries and mass flow rates considered are presented in Table 12.

Table 12 - Convective coefficient for different cooling channel geometries and mass flow rates.

$\dot{m}_{total\ used}$ [$\frac{Kg}{s}$]	$\dot{m}_{each\ channel\ geometry}$ [$\frac{Kg}{s}$]	h [$\frac{W}{m^2k}$]				
		D_h [mm]				
		10	14	7.368	25.075	18.462
1.5	1.5	80706	44043		15427	26769
	0.214		9285			
	0.115			17967		
1	1	58349	31842		11154	19353
	0.143		6713			
	0.077			12990		
0.5	0.5	33513	18289		6406	11115
	0.071		3856			
	0.038			7461		

0.25	0.25	19248	10504		3679	6384
	0.036		2215			
	0.019			4285		

Table 13 - Water properties for $T=77.5 [^{\circ}C]$.

$k \left[\frac{W}{mK} \right]$	$\mu \left[\frac{Ns}{m^2} \right]$	Pr	$\rho \left[\frac{Kg}{m^3} \right]$
6.68E-1	3.62E-4	2.27	973.34

For visual comparison purposes, Figure 39 illustrates the convective coefficient values presented in Table 12.

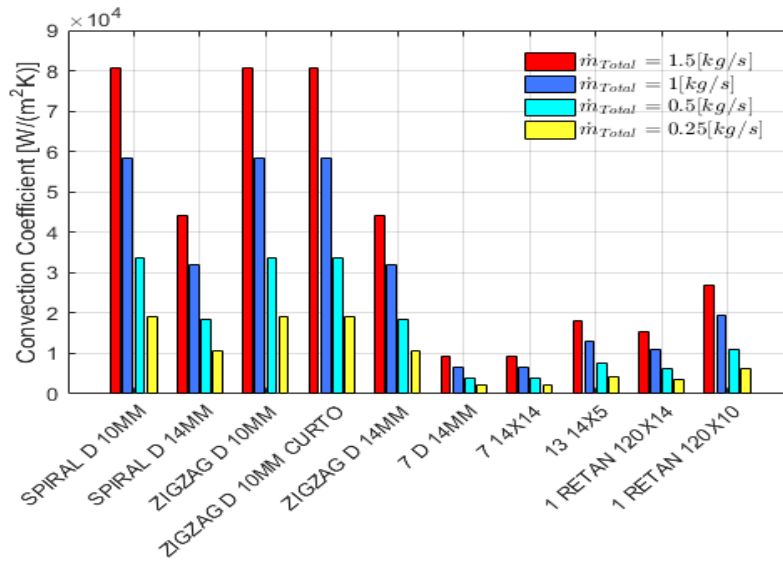
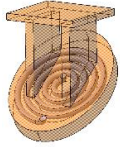
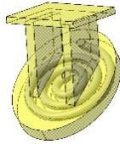
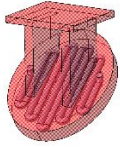
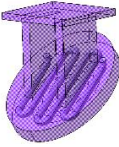
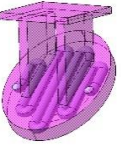
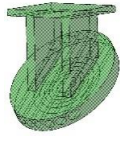
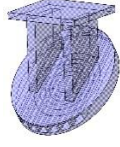
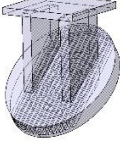
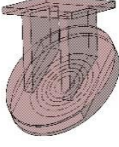
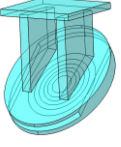


Figure 39 - Convective coefficient for the different cooling channel geometries and total mass flow rates considered.

Note that the convection area (A_c) and the volume of material remaining after incorporation of the channels or, more specifically, the volume of the mirror without accounting for the empty space where the cooling fluid flows are relevant and considered in this study see Table 14. Note that this volume is computed by subtracting to the total volume of the mirror the volume of water (V_{water}).

In the Appendix A.6 are presented the cooling channels geometries in more detail. Namely, cross sectional views and dimensions.

Table 14 - Values of A_c and V_{water} for each cooling channel geometry.

Geometry					
$A_c [m^2]$	3.82E-2	3.59E-2	4.10E-2	2.62E-2	4.25E-2
$V_{water} [dm^3]$	9.54E-3	1.26E-2	1.03E-2	6.58E-3	1.49E-2
Geometry					
$A_c [m^2]$	5.56E-2	7.08E-2	9.10E-2	4.70E-2	3.35E-2
$V_{water} [dm^3]$	1.94E-2	2.47E-2	1.69E-2	3.35E-2	2.39E-2

In the Figure 40 are illustrated the A_c and V_{water} values for each cooling channel geometry presented in the Table 14.

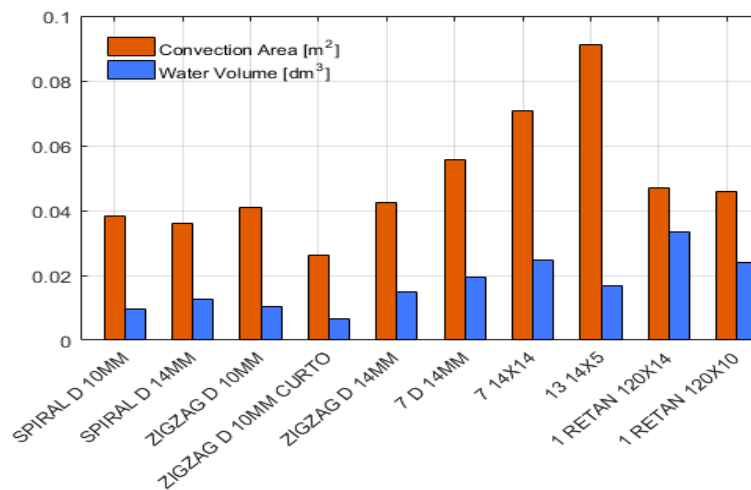


Figure 40 - Convection area A_c and water volume V_{water} values for the cooling channel geometries.

For comparison purposes, the cooling channel geometries are grouped according to channel configuration style (SPIRAL, ZIGZAG, 7 and 13 channel configuration and RETAN). The comparison is conducted considering the values of A_c , $V_{mirror_material}$, h and maximum mirror and water temperatures achieved.

The results obtained via the thermal FEA of each cooling channel geometry are presented in appendix A.6. From those results, one that has a common interpretation, for all cooling channel geometries, is the maximum outlet water temperature achieved. Considering equation (17) and being the total heat flux the same in all the simulations and knowing that to achieve steady state conditions the heat removed by the water should be the same for all cases, one may conclude that the main differences are due to the mass flow rates.

In Figure 41 are presented the maximum mirror temperatures obtained for the cooling channel geometries SPIRAL_D_10MM and SPIRAL_D_14MM.

From Figure 41, one may conclude that the most adequate cooling channel geometry (i.e., the one that presents the lowest maximum temperature) for high flow rates (i.e., above 0.5 Kg/s) is SPIRAL_D_14MM and for lower mass flow rates (i.e., below 0.5 Kg/s) is SPIRAL_D_10MM. Since the value of A_c is similar for both geometries, the only reason for SPIRAL_D_14MM to be considered the most adequate approach for high \dot{m} , despite lower convective coefficients, is the lower volume of the mirror (higher water volume) which leads to less heat storage. This conclusion is reflected in the remaining cases due to the SS 316L(N)-IG lower thermal diffusivity.

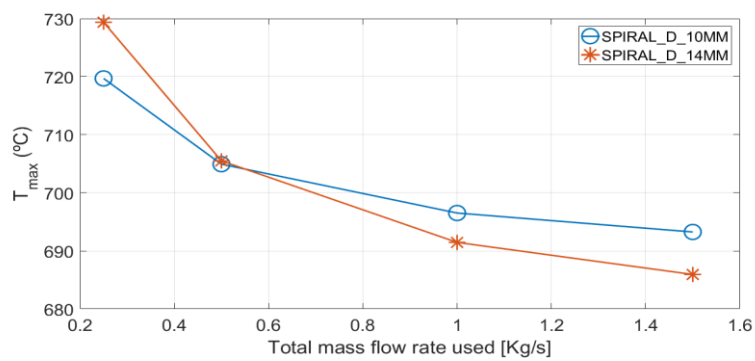


Figure 41 - Maximum mirror temperature vs total mass flow rate used for SPIRAL_D_10MM and SPIRAL_D_14MM.

Regarding the lower mass flow rates (i.e., below 0.5 Kg/s), SPIRAL_D_10MM is the most adequate cooling channel geometry of the two, as for this case the higher h values are more significant.

Figure 42 illustrates the maximum mirror temperature vs total mass flow rate used for cooling channel geometry ZIGZAG_D_10MM, ZIGZAG_D_10MM_CURTO and ZIGZAG_D_14MM.

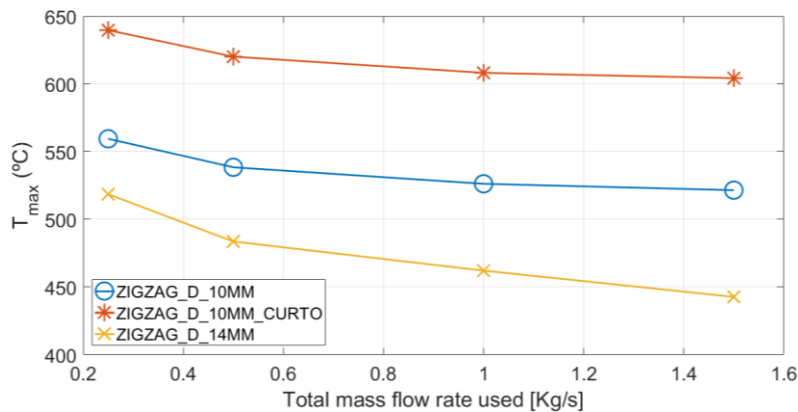


Figure 42 - Maximum mirror temperature vs total mass flow rate used for ZIGZAG_D_10MM, ZIGZAG_D_10MM_CURTO and ZIGZAG_D_14MM.

From Figure 42, one may conclude that the most adequate cooling channel geometry (i.e., the one that presents the lower maximum temperature) for the mass flow rates considered, is ZIGZAG_D_14MM. This further emphasizes the fact that, for the SS 316 L(N)-IG, the thermal diffusivity is more relevant than the convective coefficient as, even though h values are higher in the other two cooling channel geometry (ZIGZAG_D_10MM and ZIGZAG_D_10MM_CURTO), the volume of material present in the mirror is more relevant.

Moreover, the previous conclusion may also be obtained when comparing the A_c , even knowing that area is similar between ZIGZAG_14MM and ZIGZAG_10MM, as illustrated in Figure 40. This point will be more evident with the 7 and 13 cooling channel configuration results presented next.

Figure 43 illustrates the maximum mirror temperature vs total mass flow rate used for cooling channel geometry 7_D_14MM, 7_14x14 and 13_14x5.

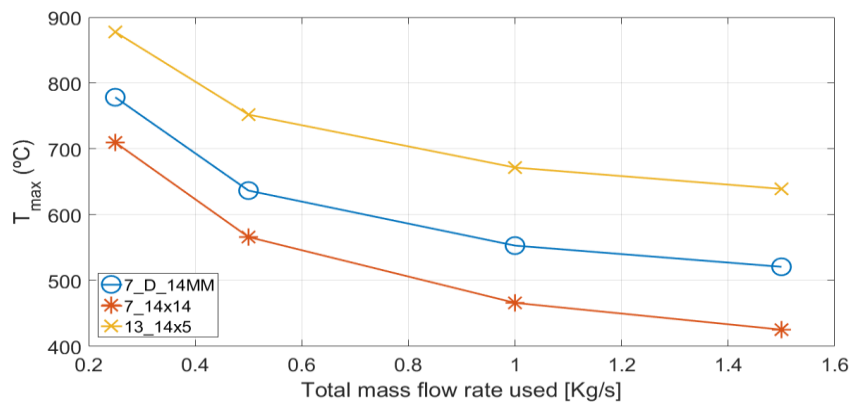


Figure 43 - Maximum mirror temperature vs total mass flow rate used for 7_D_14MM, 7_14x14 and 13_14x5.

According to Figure 43, the most adequate solution is the cooling channel geometry 7_14x14 as it is the geometry with the best combination of the two most relevant properties considered for present study (A_c and $V_{mirror_material}$).

Once more, the most adequate configuration is the one which has the lowest h value and, as previously mentioned, it becomes more evident that the thermal diffusivity is more relevant than the convection area and convection coefficient, especially when comparing 7_14x14 with 13_14x5.

Figure 44 presents the T_{max} [°C] results obtained for the cooling channel geometries 1_RETAN_120x14 and 1_RETAN_120x10. The goal of studying these cooling channel geometries is to present an approach that can lead to the achievement of the lowest mirror temperature by maximizing the volume of mirror material removed and to reinforce the fact that thermal diffusivity is the most significant property for the comparison of these two geometries.

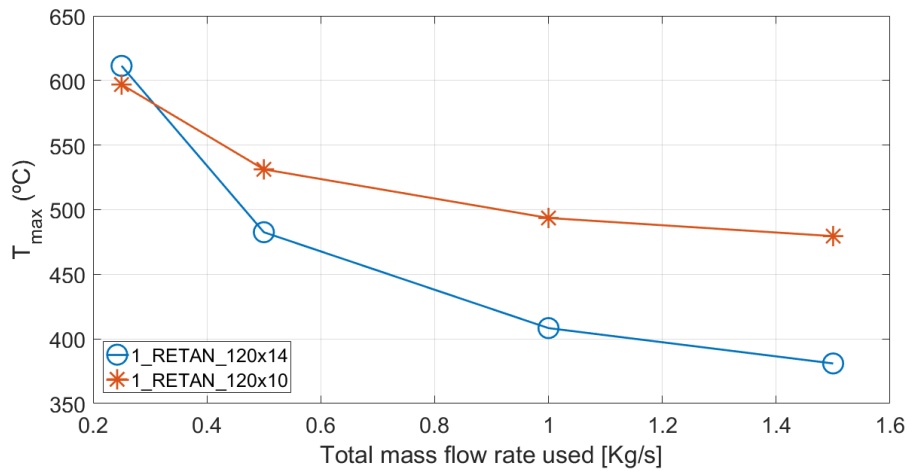


Figure 44 - Maximum mirror temperature vs total mass flow rate used for 1_RETAN_120x10 and 1_RETAN_120x14.

From Figure 44, as expected, it is with these geometries that the lowest mirror temperatures are achieved, obtaining with 1_RETAN_120x14 the lowest of all mirror temperature, more specifically ~381 °C and ~408 °C with a mass flow rate of 1.5 K_g/s and 1 K_g/s , respectively, see Figure 46.

From this analysis, one may conclude that using SS 316L(N)-IG as the mirror material implies that conduction is the most relevant of the heat transfer mechanisms.

Figure 45 illustrates the maximum temperatures results for the three most adequate for the channel geometries, i.e., 1_RETAN_120x14, ZIZAG_D_14MM and 7_14x14.

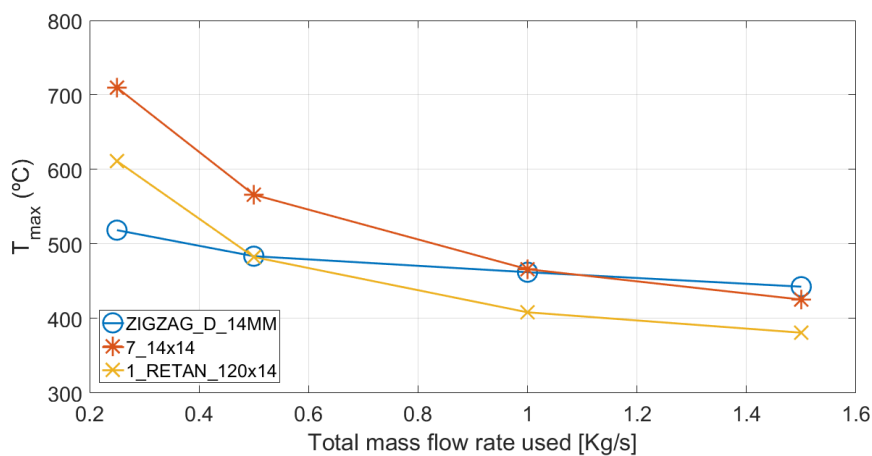


Figure 45 - Maximum mirror temperature vs total mass flow rate used for 1_RETAN_120x14, ZIZAG_D_14MM and 7_14x14.

These three cooling channel geometries should be chosen according to the operation

conditions namely, the type of mass flow rate arrangement used (in parallel or in series) and to the mirror manufacturing processes. However, considering the maximum mirror operation temperature requirement (~450°C), cooling channel geometry 1_RETAN_120x14 is the one that presents the most potential to be implemented for mass flow rates above 0.5 Kg/s.

4.2.2.4. Other Materials Considered for the Mirror

As previously mentioned in § 3.2.3.3, the methodology used for the SS 316L(N)-IG mirror is here applied considering that the mirror may be made of tungsten or copper. This is motivated by the fact that the thermal resistivity of tungsten and copper is lower than that of SS 316L(N)-IG. Note that the mirror microwave power absorbed fraction is the same as the one adopted for SS 316L(N)-IG ($A = 0.56\%$).

Relatively to the emissivity values, for tungsten are considered those presented in appendix A.5 (see Table 29), which are extracted from [37]. For copper are considered those of SS 316L(N)-IG, which are extracted from [38], and due to lack of more precise data, an average value of 0.50 is considered as the reference value for unpolished copper, as it varies between 0.20 – 0.80. However, for polished copper an emissivity value of 0.1 is considered [38].

The maximum mirror temperatures obtained for the launcher mirror without a cooling channel are 977.52°C and 1608.55°C for the copper and tungsten, respectively.

For mirrors made of copper or tungsten with a cooling channel, the maximum mirror temperature obtained is, in most cases, due to the temperature imposed as boundary condition in the support base of the mirror, as illustrated in Figure 46 (left). To perform a results comparison with the temperatures obtained for the SS 316L(N)-IG, the maximum mirror's reflective surface temperature data is estimated, see Figure 46 (right). The results obtained for this analysis are presented in the appendix A.7 and A.8.

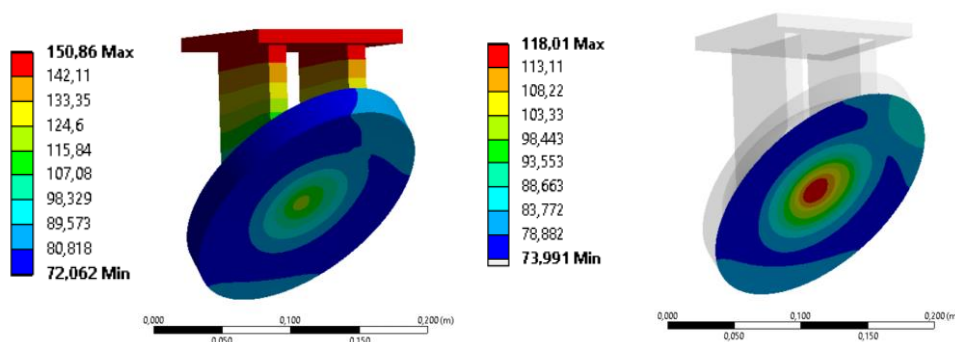


Figure 46 - Temperature distribution for cooling channel geometry SPIRAL_D_14MM with a mass flow rate of 1.5 Kg/s, element size of 0.0025 mm and copper as the mirror material: left) temperature of the mirror and; right) temperature of the reflective surface of the mirror.

To compare these results with those obtained for SS 316L(N)-IG, in Figure 47 and Figure 48 are presented the values for the maximum temperature of the reflective mirror surface for tungsten and copper, respectively, considering the most adequate cooling channel geometries for the case of SS 316 L(N)-IG, i.e., ZIGZAG_D_14MM, 7_14x14 and 1_RETAN_120x14. In addition, the cooling channel geometry with the best results achieved for copper and tungsten, ZIGZAG_D_10MM, is also represented in the same figures.

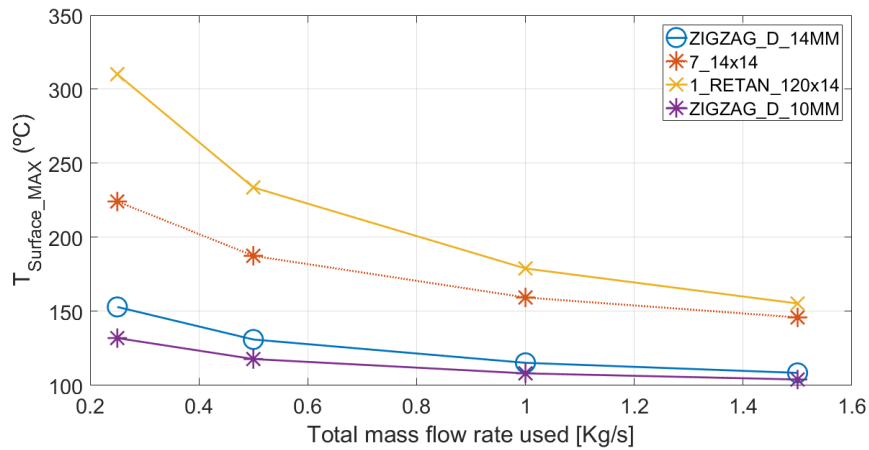


Figure 47 - Maximum reflective mirror surface temperature vs total used mass flow rate for copper.

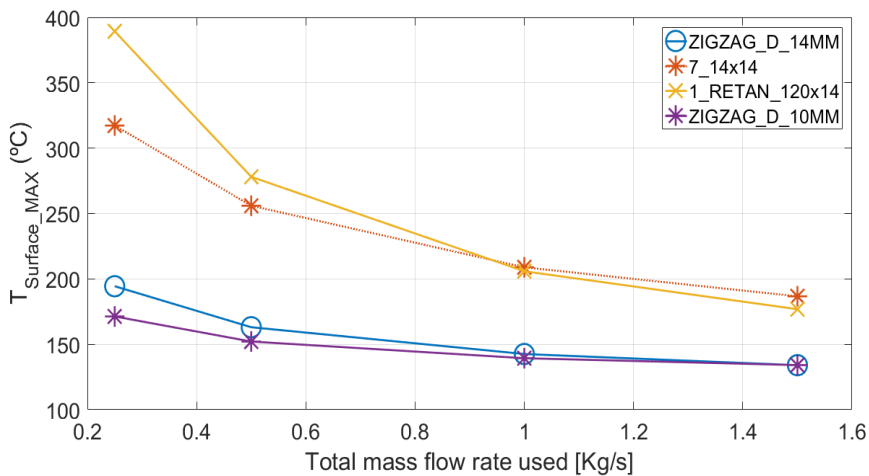


Figure 48 - Maximum reflective mirror surface temperature vs total used mass flow rate for tungsten.

Analyzing the results presented in the two previous figures (Figure 47 and Figure 48), one may conclude that the most suitable cooling channel geometries for the SS 316 L(N)-IG are not the same as those obtained for copper or tungsten.

In contrast with SS 316L(N)-IG, one verifies that for copper and tungsten the most relevant heat transfer mechanism is convection rather than conduction as one obtains better results (i.e., lower temperatures of the reflective mirror surface) with a cooling channel geometry that provides a more efficient combination of convection parameters like A_c and h and not for those that present lower $V_{mirror_material}$. This is further supported by the fact that the copper and tungsten thermal diffusivity values are significantly higher than those of SS 316 L(N)-IG, as illustrated in Figure 49.

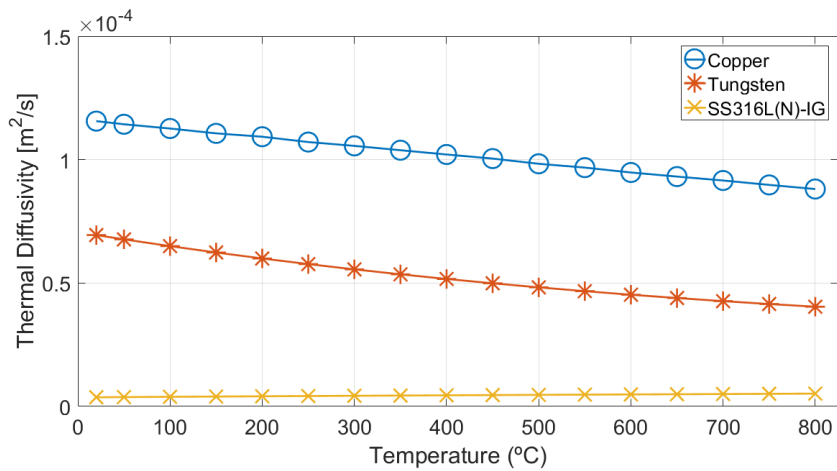


Figure 49 - Thermal diffusivity vs temperature for SS316L(N)-IG, Tungsten and Copper.

To further substantiate the previous comment, in Figure 50 are illustrated the maximum surface temperature obtained for different mass flow rates of cooling channel geometries ZIGZAG_D_10MM, ZIGZAG_D_10MM_CURTO and 13_14x5, considering tungsten as the mirror material.

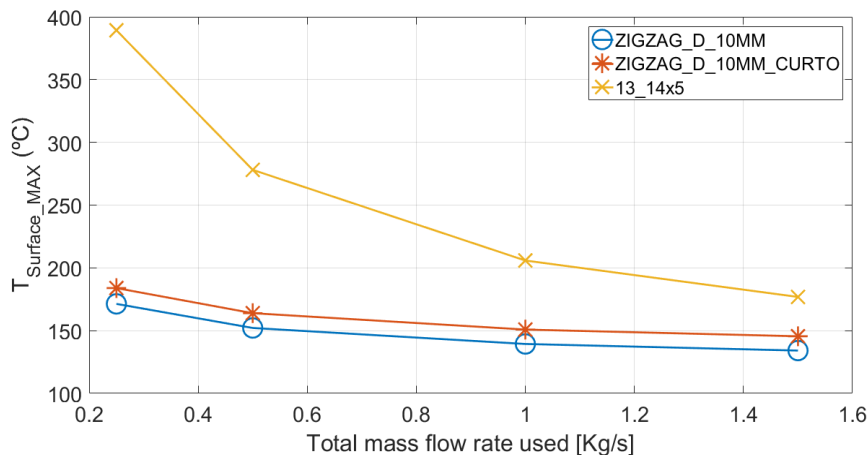


Figure 50 - Maximum surface temperature vs the total mass flow rate for ZIGZAG_D_10MM, ZIGZAG_D_10MM_CURTO and 13_14x5 for Tungsten.

According to Table 12 and Figure 40, ZIGZAG_D_10MM_CURTO has the same h and a smaller A_c whereas 13_14x5 has a greater A_c but has a lower h and $V_{mirror_material}$ in comparison with ZIGZAG_D_10MM. However ZIGZAG_D_10MM has a better performance than the others, emphasizing, in this way, the relevance of the parameters that interfere with the convection and

their importance over those that influence conduction.

Note that with the use of copper and tungsten, the maximum mirror temperatures are lower than those obtained for SS 316L(N)-IG and are below the operation temperature range. On the other hand, for copper this is not the case as the maximum temperature exceeds the operation temperature. Hence, tungsten is, from a thermal point of view, more adequate than SS 316L(N)-IG or copper.

4.2.3. Transient Thermal FEA

The transient thermal FEA considers SS 316L(N)-IG as the mirror material and the most adequate cooling channel geometry studied is ZIGZAG_D_14MM, see § 4.2.2.3 .

As mentioned in § 3.2.4, there are two different phases, the burn and dwell time phases with a duration of 400 s and 1400 s, respectively [37]. These phases have influence on the actuation time of some boundary conditions, more precisely the microwave beam power, the plasma radiation and the internal heat generation. Furthermore, some changes must be made on the way that these inputs are implemented in ANSYS®Mechanical, as illustrated in Figure 51 and Figure 52.

Figure 51 illustrates one of the six heat flows (result of the approach studied in § 4.2.1), as excluding the beam power, the implementation of each heat flow is the similar.

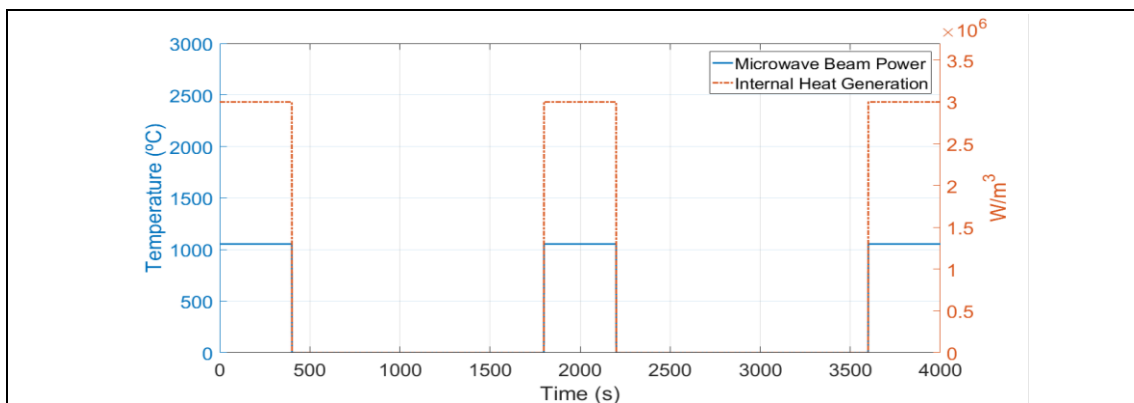


Figure 51 - Representation, for the transient thermal FE analysis, of internal heat generation, microwave beam power (1054.6 W).

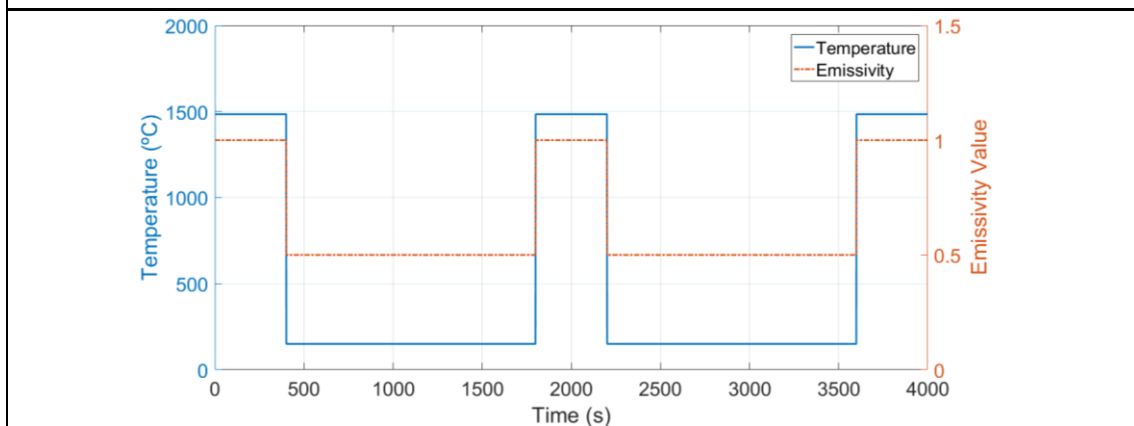


Figure 52 - Representation, for the transient thermal analysis, of the boundary conditions used to model the plasma.

Figure 53 and Figure 54 illustrates the results obtained for the transient thermal FEA using the cooling channel geometry ZIGZAG_D_14MM with a mass flow rate of 1.5Kg/s considering that fluid flow is in series.

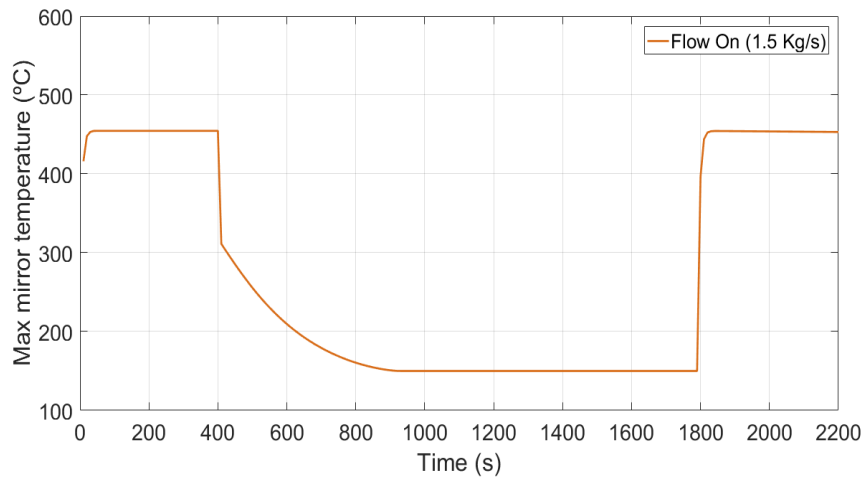


Figure 53 - Maximum mirror temperature considering a mass flow rate of 1.5 Kg/s (in series) with flow on during the dwell time phase.

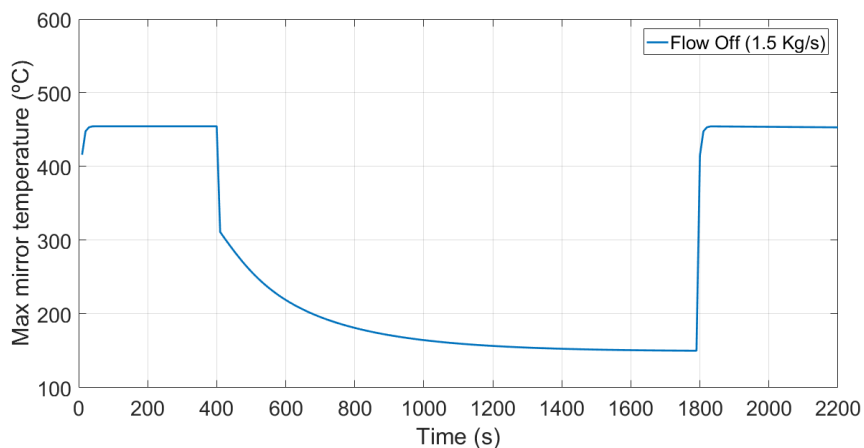


Figure 54 - Maximum mirror temperature considering a mass flow rate of 1.5 Kg/s (in series) with flow off during the dwell time phase.

According to Figure 53 and Figure 54, in the first 400s (burn time phase) steady state conditions are achieved presenting a maximum temperature of approximately 450°C (see, Figure 45). Similarly, the same is verified for the second burn time phase (at 1800s).

Furthermore, comparing the flow on and flow off plots, see Figure 53 and Figure 54, respectively, one observes that even with the cooling system turned off, the dwell time phase of 1400s is enough to cool down the mirror until 150°C. However, maintaining the cooling system on, this condition is achieved earlier.

In Figure 55 and Figure 56 are illustrated the results obtained for the transient thermal FEA using the cooling channel geometry ZIGZAG_D_14MM with a mass flow rate of 0.25Kg/s considering that fluid flow is in parallel.

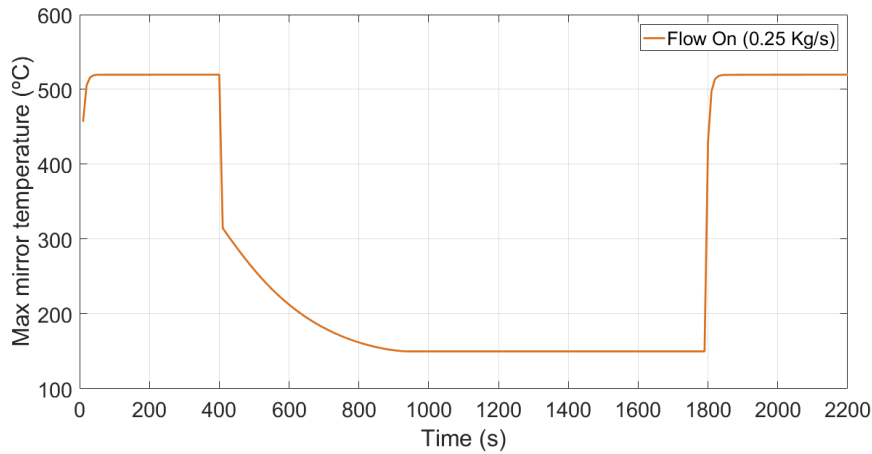


Figure 55 - Maximum mirror temperature considering a mass flow rate of 0.25 Kg/s (in parallel) with flow on during the dwell time.

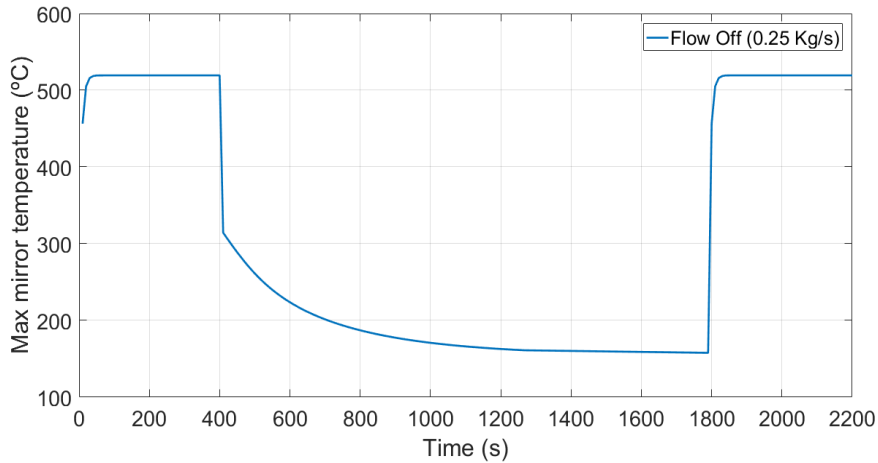


Figure 56 - Maximum mirror temperature considering a mass flow rate of 0.25 Kg/s (in parallel) with flow off during the dwell time.

If the paralleled flow configuration is considered for the cooling system, a mass flow equal to 0.25 Kg/s, the maximum temperature of the mirror increases, as expected. Never the less, the steady state conditions are achieved, see Figure 55 and Figure 56, as higher maximum temperatures are achieved due to a lower convection coefficient and the minimum mirror temperature (150 °C) is also achieved during the dwell time phase whether the flow is on or off.


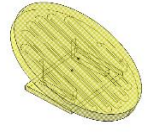
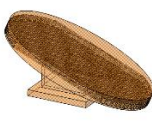
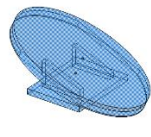
Although the operation temperature, for the SS 316L(N)-IG, is not respected under the conditions assumed, it is possible to assure, for the all mass flow rates considered in this dissertation, the minimum mirror temperature is achieved during the dwell time.

4.3. Receiver Mirror

The receiver mirror is analyzed according the methodology previously presented and used for the launcher mirror and described in § 3.3 considering only four cooling channel geometries, see Table 15.

In the Appendix A.7 are presented the cooling channels geometries in more detail. Namely, cross sectional views and dimensions.

Table 15 - Chosen cooling channel geometries, respective areas, and water volume.

Geometry				
	ZIGZAG_D_10MM	ZIGZAG_D_14MM	27_14X5	1_RETAN_240 X14
$A_c [m^2]$	1.47E-1	1.56E-1	3.47E-1	1.62E-1
$V_{water} [dm^3]$	2.78E-1	5.45E-1	6.39E-1	1.28

The cooling channel geometries are selected based in the tendency of being more favorable to present the highest convective coefficient, highest convective area, lowest volume of material and best combination of the three. This tendency is noted in the study previously conducted for the launcher mirror.

4.3.1. Mesh Convergence

Similarly to § 4.2.2.1, a mesh convergence study is conducted for the four geometries (see, Table 39 in appendix A.1). However, only one is presented next for exemplification purposes.

Figure 57 illustrates the maximum temperatures obtained and the upper and lower temperature deviation limits that are less or equal than 1% or less for cooling channel geometry 1_RETAN_240x14.

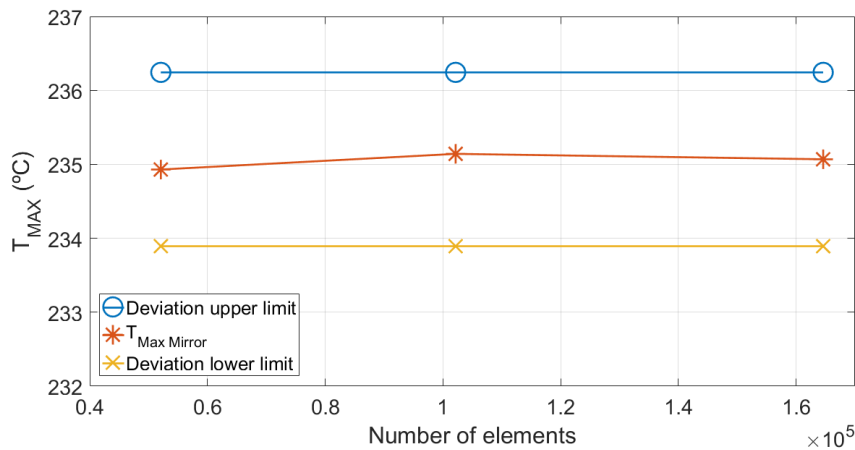


Figure 57 - Mesh convergence of the maximum temperature for channel 1_RETAN_240x14.

From Figure 57 one can observe that the maximum temperature points are bounded by the upper and lower deviation limits as one may assume that convergence is successfully achieved for an element mesh size of 2.5 mm, which is the one used in the following analyses.

4.3.2. Pressure Drop

The pressure drop analysis is conducted considering that the mirror is made of commercial stainless steel and the cooling channel geometry ZIGZAG_D_10MM, as it has the characteristics to provide the higher head loss value.

The main differences, in comparison with the geometry selected for the study of the pressure drop of the launcher mirror, see § 4.2.2.2, are the ΔL ($\Delta L = 4670.4 \text{ mm}$) and the number of 180° elbows (*number of 180° elbows* = 17). The other relevant input data assumed is the same as that considered for the launcher mirror, see § 4.2.2.2.

Table 16 presents the results for the pressure drop of the mass flow rates below 0.50 Kg/s , as the maximum pressure drop should be lower than 1.35 MPa .

Table 16 - Pressure drop for cooling channel geometry ZIGZAG_D_10MM.

Mass flow rate [Kg/s]	1.50	1.00	0.50	0.25
u_m [m/s]	19.10	12.73	6.37	3.18
Re_d	5.28E5	3.52E5	1.76E5	8.79E4
$p_1 - p_2$ [MPa]	3.65	1.62	0.41	0.10
p_2 [MPa]	0.35	2.38	3.59	3.90

Having the previous results in mind, see Table 16, one can conclude that the ZIGZAG_D_10MM configuration is not an adequate solution for the flow in series, since the pressure drop for 1.50 Kg/s is higher than 1.35 MPa but can be so when the parallel approach with a mass flow rate lower than 1.00 Kg/s is considered.

Table 17 presents the results for the pressure drop considering the cooling channel geometry ZIGZAG_D_14MM considering $\Delta L = 3537.7 \text{ mm}$ and *number of 180° elbows* = 13. The remaining data is the same as that for ZIGZAG_D_10MM.

Table 17 - Pressure drop for cooling channel geometry ZIGZAG_D_14MM.

Mass flow rate [Kg/s]	1.50	1	0.50	0.25
V [m/s]	9.74	6.50	3.25	1.62
Re_d	3.77E5	2.51E5	1.26E5	6.28E4
$P_1 - P_2$ [MPa]	0.58	0.26	0.06	0.02
P_2 [MPa]	3.42	3.74	3.94	3.98

For ZIGZAG_D_14MM which, is the next cooling channel geometry considered it presents similar characteristics to ZIGZAG_D_10MM as it has a higher head loss value. Note that it is not possible to have a pressure drop higher than 1.35 MPa for whatever is the fluid flow, see [35]

4.3.3. Steady State Thermal FEA

Regarding the steady state thermal FEA of the receiver mirror, it is considered SS 316L(N)-IG as the material for the mirror and similarly to the launcher mirror, the plasma in the simulations is modeled as a radiating surface at 1484 °C, see Figure 30. Note that the receiver mirror is not exposed to a microwave beam.

The input data to introduce in ANSYS®Mechanical is:

- Mirror surrounding surfaces and support base temperature, 150 °C;
- Mirror reflective surface emissivity (polished surface), $\varepsilon = 0.1$;
- Other mirror surfaces emissivity (for 450 °C), $\varepsilon = 0.5$;
- Internal heat generation value, $\dot{q} = 3 \left[\frac{MW}{m^3} \right]$;
- Surface temperature (see Figure 30), 1484 °C.

Following the methodology described in § 3.2.3.2, the maximum mirror temperature achieved for the receiver mirror without a cooling system, is 1063.80 °C. Thus, it is verified that it is necessary to design a cooling system as the maximum operation temperature for a mirror made of SS 316L(N)-IG is ~450 °C.

Knowing the chosen cooling channel geometries, see Table 15, and that a cooling system is needed, in Table 18 are presented the convective coefficients for different cooling channels geometries and mass flow rates.

Table 18 - Convective coefficient for the different cooling channel geometries and mass flow rates.

$\dot{m}_{total\ used}$ $\left[\frac{Kg}{s} \right]$	$\dot{m}_{each\ channel\ geometry}$ $\left[\frac{Kg}{s} \right]$	$h \left[\frac{W}{m^2k} \right]$			
		$D_h [mm]$			
		10	14	7.368	26.457
1.5	1.5	80706	44043		14006
	0.056			10012	
1	1	58349	31842		10127
	0.037			7238	
0.5	0.5	33513	18289		5816
	0.019			4158	
0.25	0.25	19248	10504		3341
	0.009			2388	

In Figure 58 and Figure 59 are illustrated the data from Table 15 and Table 18, respectively, for a better visualization and comparison of the values considered for each cooling channel geometry.

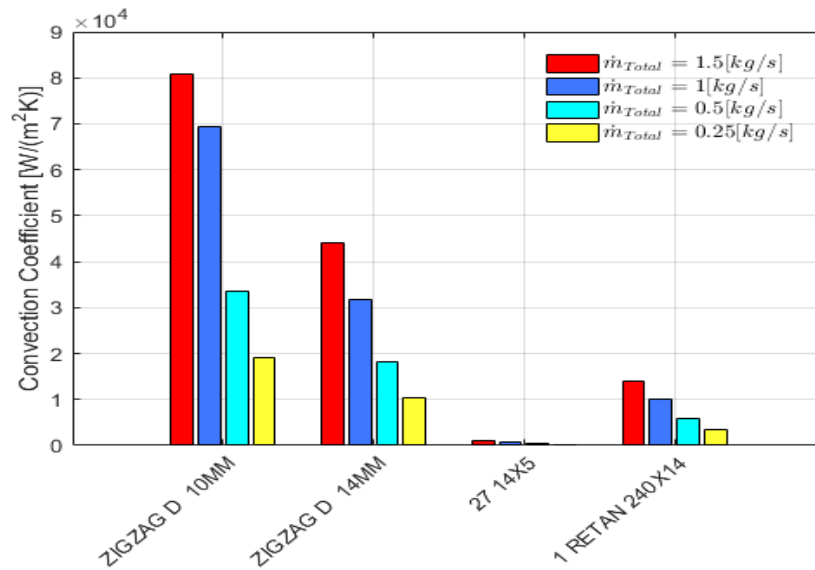


Figure 58 - Graphical representation of the convection coefficient for each channel geometry.

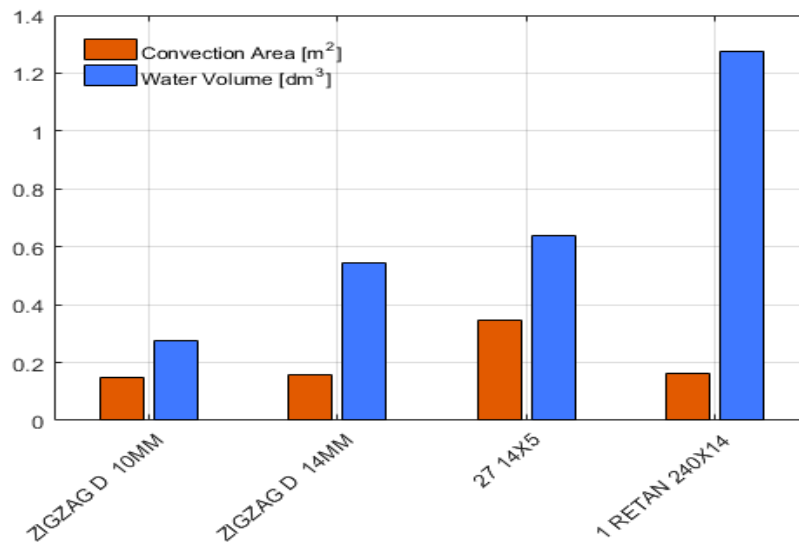


Figure 59 - Graphical representation of the convection area and the water volume for each channel geometry.

Following the methodology described in § 3.3 and § 3.2.3.2, the maximum temperature results for the steady state thermal FEA of the receiver mirror considering four cooling channel geometries are illustrated in Figure 60.

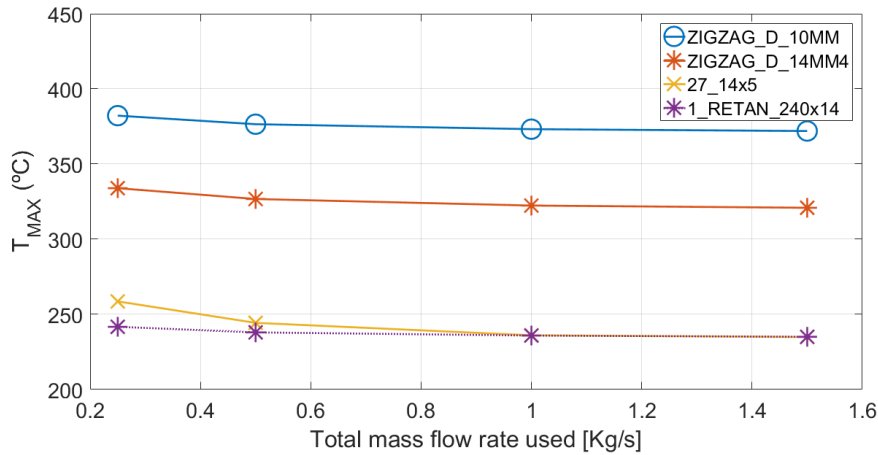


Figure 60 - Maximum mirror temperature vs total mass flow rate for different channel geometries.

According to Figure 60, the most adequate geometries are the 27_14x5 and 1_RETAN_240x14 as they present the lowest maximum temperatures. However, all cooling channel geometries present a satisfactory performance in the sense that the operation temperature restriction is satisfied. Hence, a study considering other materials is not required.

From Figure 60, by comparing ZIGZAG_D_10MM with ZIGZAG_D_14MM, it is noted that a similar tendency is verified, as convection has lower influence than conduction. This is supported by the comparison of the h value with the material volume in the mirror, assuming a relatively approximate convection area between both geometries.

Additionally, by comparing the ZIGZAG_D_14MM with the 27_14x5 configurations, it is possible to verify that the convection coefficient, which is related to the flow, is the less influencing parameter of those studied.

As expected, the lowest mirror temperature is achieved with the cooling channel geometry that allows a design with less solid material (1_RETAN_240x14), as convection has lower influence than conduction.

A similar performance to 1_RETAN_240x14 is achieved with the 27_14x5 geometry, revealing that the parameters related with convection can be tuned in order to obtain satisfactory results. However, if the parallel flow approach is considered, this cooling channel geometry is not the most adequate, as one can see in Figure 60.

4.3.4. Transient Thermal FEA

A transient thermal FEA of the receiver mirror is conducted following the methodology described in § 3.2.4, considering the mirror made of SS 316L(N)-IG and the geometry that achieved the most adequate results in steady state analysis, i.e., 1_RETAN_240x14.

The transient thermal FEA considers the burn and the dwell time phases, with a duration of 400s and 1400s, respectively. Thus, the boundary conditions are treated in the same way as the ones for the launcher mirror, see Figure 52, apart from the microwave beam that in non-

existent.

Similarly to the launcher mirror, it is necessary to verify: if the receiver mirror achieves the maximum operation temperature without a cooling system; if steady state conditions are achieved during the 400s of the burn time phase with a cooling system; and if there is the need of having the cooling system turned on during the dwell time phase.

In Figure 61 and Figure 62 are illustrated the maximum mirror temperature results of the transient thermal FEA for the cooling channel geometry 1_RETAN_240x14 with a mass flow rate of 1.5 Kg/s turned on and off, respectively.

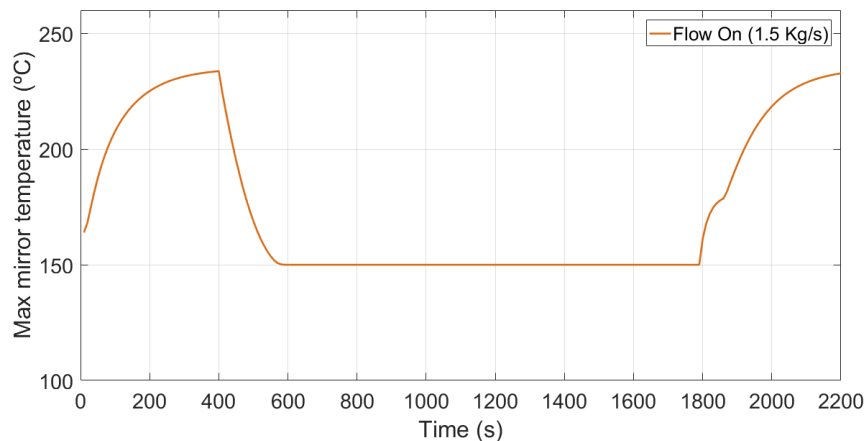


Figure 61 - Maximum mirror temperature considering a mass flow rate of 1.5 Kg/s with flow on during the dwell time.

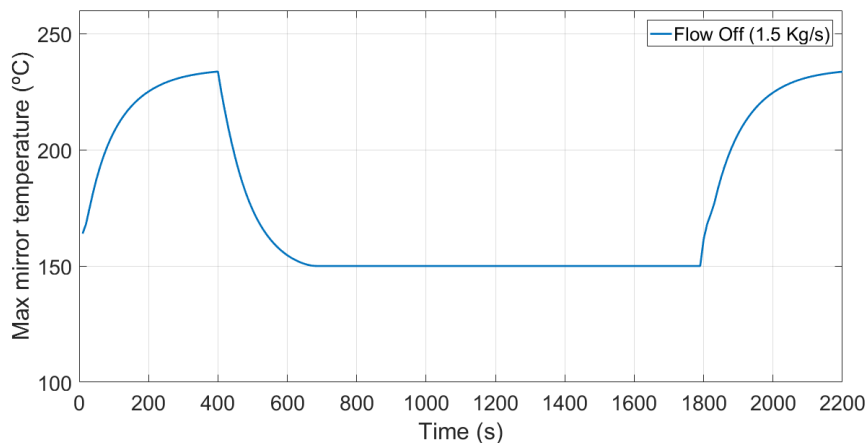


Figure 62 - Maximum mirror temperature considering a mass flow rate of 1.5 Kg/s with flow off during the dwell time phase.

According to Figure 61 and Figure 62, in the first 400s (burn time phase) steady state conditions are achieved, being the maximum temperature achieved ~ 235°C.

By comparing the flow on and flow off plot, Figure 61 and Figure 62, respectively, one observes that even with the cooling system turned off, during the 1400s of dwell time phase, it is enough to cool down the mirror until its lower temperature (150°C) is achieved. Nevertheless,

maintaining the cooling system turned on this condition is achieved earlier. However, the difference between flow on and flow off for the receiver mirror is not so pronounced as for the launcher mirror, comparing Figure 61 and Figure 62 to Figure 53 and Figure 54 presented in § 4.2.3.

In Figure 63 and Figure 64 are illustrated the maximum mirror temperature results of the transient thermal FEA for the cooling channel geometry 1_RETAN_240x14 with a mass flow rate of 0.25 Kg/s turned on and off, respectively.

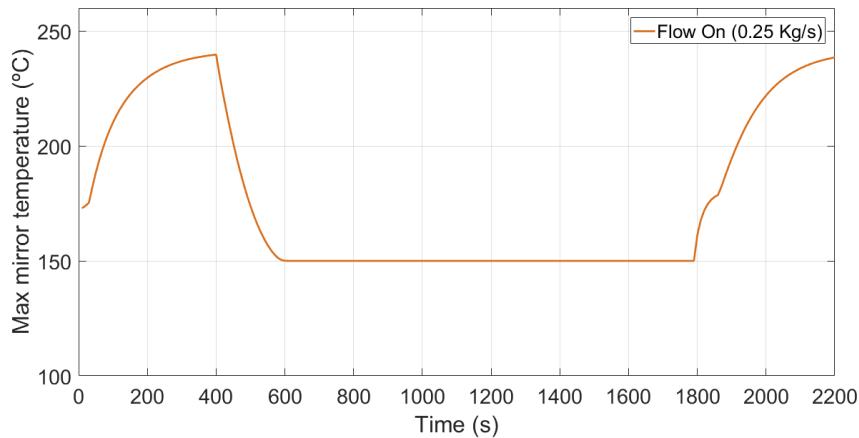


Figure 63 - Maximum mirror temperature considering a mass flow rate of 0.25 Kg/s with flow off during the dwell time.

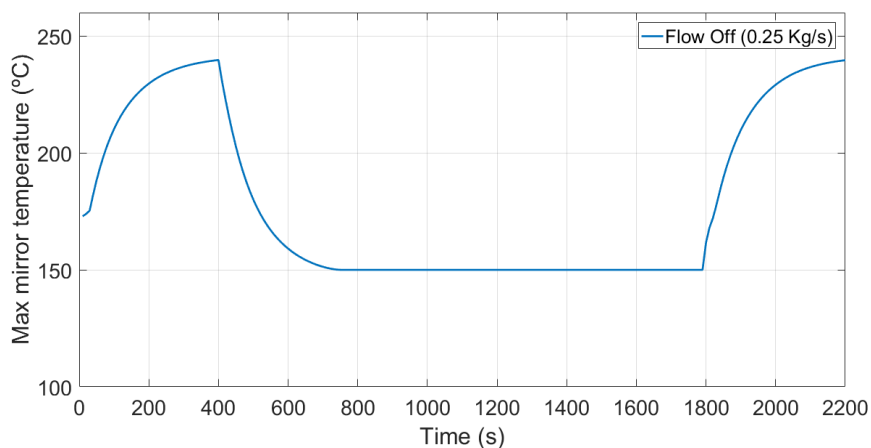


Figure 64 - Maximum mirror temperature considering a mass flow rate of 0.25 Kg/s with flow off during the dwell time phase.

According to the Figure 60, the maximum temperature achieved for 1_RETAN_240x14 does not vary significantly with the mass flow rate, which implies that it does not change with the convection coefficient. Hence, it is expected that the results for a mass flow rate of 0.25 Kg/s, in case of a paralleled flow configuration for the cooling system, are very similar to the ones obtained for a series flow (1.5 Kg/s) as one can see in Figure 63 and Figure 64.

4.4. Steady State Fluid Flow Thermal Analysis

The steady state fluid flow thermal analysis is performed in order to verify the convective coefficient and the pressure drop inside the cooling channels used for the thermal FEA performed in this dissertation, as mentioned and described in § 3.4.

The considered cooling channel geometries for study in ANSYS®Fluent are:

- For the launcher mirror (see Table 3 in § 3.2.3.2):
 - ZIZAG_D_10MM;
 - 1_RETAN_120x14;
- For the receiver mirror (see Table 15 in § 4.3):
 - ZIZAG_D_14MM;
 - 1_RETAN_240x14.

The RETAN cooling channels geometries are chosen as they are the most suitable, from those here studied, presenting the lowest maximum temperatures, see § 4.2.2.3 and § 4.3.3 for the launcher and receiver mirrors, respectively.

The ZIZAG cooling channels geometries are chosen as they present high pressure drops values, see § 4.2.2.2 and § 4.3.2 for the launcher and the receiver respectively, leading to conservative estimations.

As input to ANSYS®Fluent, apart from the turbulence model, it is defined the inlet velocity of the flow and the outlet gauge pressure. The outlet gauge pressure is set to zero so that the inlet pressure is the required pressure drop value.

To obtain the convective coefficient in ANSYS®Fluent, it is necessary to implement the same boundary conditions as those implemented for the thermal FEA, i.e., radiation coming from the plasma, the stray radiation, internal heat generation due to the neutrons flux, the microwave beam power absorbed (in case of the launcher) and the inlet temperature of the cooling fluid (70 °C), see § 4.2.2. Nevertheless, the radiation coming from plasma and the stray radiation are considered as a heat flow that corresponds to the outgoing net radiation from the mirror surfaces, see Table 19. These values are obtained from the thermal FEA, conducted in ANSYS®, using a radiation probe for all the mirror surfaces. This approach is adopted so that there is no need for introducing the surrounding surfaces and the first wall, see Figure 27 and Figure 30.

Table 19 - Outgoing net radiation from the launcher and receiver mirrors surfaces.

	Launcher	Receiver
Outgoing net radiation $\left[\frac{W}{m^2}\right]$	-11364.65	-16214.73

In Table 20 and Figure 65, are presented the analytical and ANSYS®Fluent results for the ZIGZAG_D_10MM and 1_RETAN_120x14 cooling channel geometries considered the launcher mirror. Note that in ANSYS®Fluent, the results for the convection coefficient are local values. In order to compute the h , so that its value can be compared with the analytical ones, an

average of the local values is made. Furthermore, note that the analytical results for the pressure drop of 1_RETAN_120x14 are not presented in § 4.2.2.2. However, these results are presented in Table 20 and are computed using the same methodology that lead to those presented in Table 9 (§ 4.2.2.2) whereas, the analytical results regarding h are presented in Table 12 (§ 4.2.2.3).

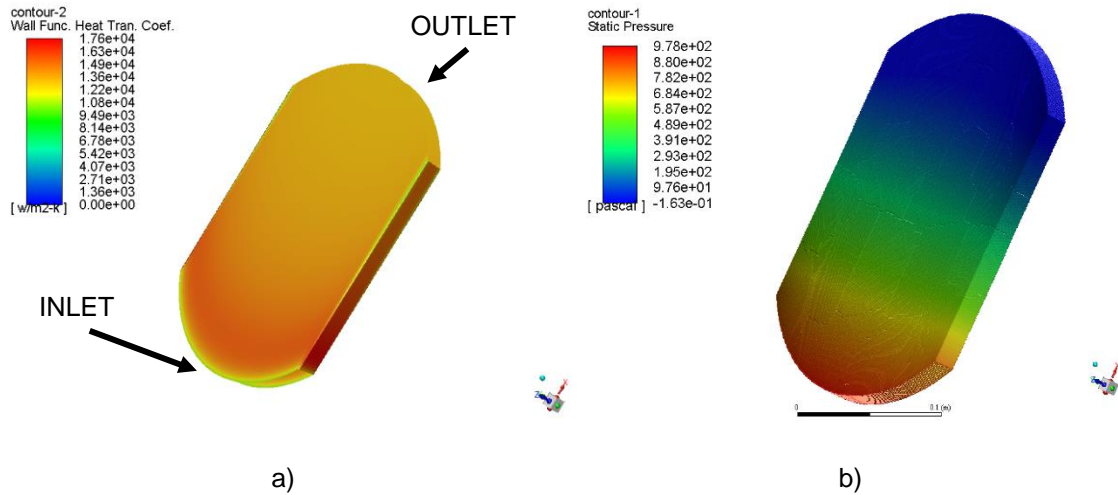


Figure 65 - Launcher mirror1_RETAN_120x14 cooling channel geometry: a) Local convection coefficient and; b) Pressure values.

Table 20 - Analytical results and FLUENT results for the ZIGZAG_D_10MM and 1_RETAN_120x14, launcher mirror.

		ZIGZAG_D_10MM				1_RETAN_120x14			
$\dot{m} \left[\frac{Kg}{s} \right]$		1.50	1.00	0.50	0.25	1.50	1.00	0.50	0.25
$u_m \left[\frac{m}{s} \right]$		19.10	12.73	6.37	3.18	3.04	2.03	1.01	0.51
Analytically	$\Delta p [MPa]$	1.33	0.59	0.15	0.04	1.11E-3	4.94E-4	1.24E-4	3.09E-5
	$h \left[\frac{W}{m^2K} \right]$	80706	58349	33513	19248	15427	11154	6406	3679
FLUENT	$\Delta p [MPa]$	1.65	0.88	0.31	0.10	9.78E-4	4.90E-4	1.48E-4	4.93E-5
	$h \left[\frac{W}{m^2K} \right]$	115651	73223	39247	25431	13663	10377	6025	5814

From Table 20, one can conclude that the results achieved for the h with ANSYS®Fluent present some deviations but are in the same order of magnitude. Recalling that for the SS 316L(N)-IG the most relevant heat transfer mechanism is conduction, see § 4.2.2.3 and § 4.3.3,

these deviations are not significant as they do not influence the maximum temperatures obtained in the mirrors. Regarding the results of the pressure drop presented in Table 20, one verifies that higher values are obtained for ZIZAG_D_10MM, one of which is higher than the limit pressure drop of 1.35 MPa and when comparing with the analytical values, these show a similar trend.

Considering 1_RETAN_120x14 cooling channel geometry, from Table 20 one verifies that the pressure drop values are all similar to the analytical ones which are lower than the limit of 1.35 MPa. Therefore, the values for the pressure drop are verified for 1_RETAN_120x14 and it can be selected as the most adequate cooling channel geometry for the launcher mirror.

In Table 21 and Figure 66 are presented the analytical and ANSYS®Fluent results for the ZIGZAG_D_14MM and 1_RETAN_240x14 cooling channel geometries for the receiver mirror.

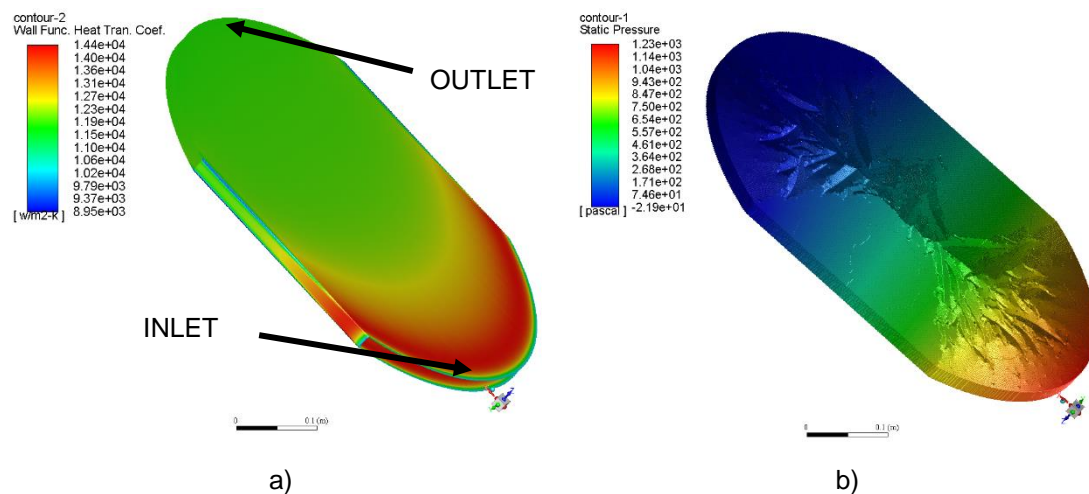


Figure 66 - Receiver mirror with 1_RETAN_240x14 cooling channel geometry: a) Local convection coefficient and; b) Pressure values.

Table 21 - Analytical results and FLUENT results for the ZIGZAG_D_14MM and 1_RETAN_240x14, receiver mirror.

		ZIGZAG_D_14MM				1_RETAN_240x14			
$\dot{m} \left[\frac{Kg}{s} \right]$		1.50	1.00	0.50	0.25	1.50	1.00	0.50	0.25
$u_m \left[\frac{m}{s} \right]$		9.74	6.50	3.25	1.62	2.73	1.82	0.91	0.45
Analytically	$\Delta p [MPa]$	0.58	0.26	0.06	0.02	1.60E-3	7.13E-4	1.78E-4	4.46E-5
	$h \left[\frac{W}{m^2K} \right]$	44043	31842	18289	10504	14006	10127	5816	3341
FLUENT	$\Delta p [MPa]$	1.08	0.27	0.14	-	1.23E-3	6.18E-4	1.86E-4	5.94E-5
	$h \left[\frac{W}{m^2K} \right]$	48887	40566	31846	-	12088	9260	5375	3262

From Table 21, one can verify that the values of the pressure drop are slightly higher than the analytical values but are still lower than the limit pressure drop of 1.35 MPa. Relatively to h , it is possible to verify that the analytical values are lower than those computed using

ANSYS®Fluent, meaning that the heat removal by convection is higher. However, recalling that for the SS 316L(N)-IG the most relevant heat transfer mechanism is conduction, see § 4.2.2.3 and § 4.3.3, these deviations are not significant as they do not influence the maximum temperatures obtained in the mirrors.

Regarding the 1_RETAN_240x14 cooling channel geometry the conclusions are the same as the ones obtained for the 1_RETAN_120x14 cooling channel geometry used for the launcher in this analysis, i.e.: the h values are in the same order of magnitude; and the pressure drop values are similar to the analytical values and lower than the limit value of 1.35 MPa . Hence, this cooling channel geometry is the selected cooling channel geometry for the receiver mirror.

5. Conclusions and Future Works

This dissertation presents a study on the development of a cooling system for the launcher and receiver mirrors of the ITER CTS diagnostics system that exceed the maximum required operational temperature of $\sim 450^{\circ}\text{C}$. For it, Computer Aided Design (CAD) models of the mirrors with different cooling channel geometries are developed and steady state and transient thermal FEA are conducted for the assessment of the feasible solutions.

A steady state thermal FEA of the launcher and receiver mirrors, made of SS 316L(N)-IG, without cooling verifies that in fact a cooling system is required, as they achieved the maximum temperature of 2306.52°C and 1063.80°C , respectively.

This motivated the development of ten cooling channel geometries that are analyzed and compared, leading to the following conclusions:

- Thermal diffusivity indicates which heat transfer mechanism (conduction or convection) and consequently which parameters are more relevant;
- Hence, for the SS 316L(N)-IG mirrors (lower thermal diffusivity), parameters related with conduction are more relevant than those related with convection, e.g., volume of material;
- For the tungsten and copper mirrors (higher thermal diffusivity), the parameters related to convection are more relevant than those related with conduction, e.g., convection area and coefficient.

Thus, the selected cooling channel geometry for the SS 316L(N)-IG launcher mirror is 1_RETAN_120x14, for mass flow rate of 1.5 Kg/s (in series) obtaining a maximum temperature of $\sim 381^{\circ}\text{C}$. The use of tungsten as the material for the launcher mirror with the cooling channel geometry of ZIGZAG_D_10MM, for mass flow rate of 1.5 Kg/s (in series) leads to a maximum temperature of $\sim 151^{\circ}\text{C}$. This corresponds to a temperature decrease $\sim 83.5\%$ for SS 316L(N)-IG and $\sim 90.6\%$ for tungsten, considering that for this last one the temperature achieved without a cooling channel is 1608.55°C .

Regarding the receiver mirror, the use of SS 316L(N)-IG is not an issue as the maximum temperature obtained is below the operational temperature for all studied cooling channel geometries, being 1_RETAN_240x14 the most adequate whether the flow is set up in parallel or in series, being the maximum temperature achieved $\sim 240^{\circ}\text{C}$.

From the transient thermal FEA both mirrors and independently of the mass flow rate one concludes that are achieved:

- Steady state conditions, during the burn time phase;
- The minimum mirror temperature ($\sim 150^{\circ}\text{C}$) during the dwell time whether the fluid flow is on or off.

The steady state fluid flow analyses verified that the convection coefficients used and the

press drop values obtained in this dissertation are satisfactorily acceptable specially for the two chosen cooling channels geometries, 1_RETAN_140x14 and 1_RETAN_240x14 for the launcher and receiver mirror, respectively, considering the mirrors made of SS 316 L(N)-IG.

From this dissertation, it is worth mentioning the following original contributions:

- The methodology developed and used in this dissertation to study the CTS mirrors may applied to other be components of the ITER project under similar conditions;
- The MATLAB routine developed and used to compute the power distribution on the surface of the launcher mirror;
- Cooling channel geometries for the launcher and receiver mirrors that can effectively decrease the maximum temperatures by $\sim 80.5\%$ and $\sim 93.5\%$ respectively, putting it in the operating temperature range.

As future works, it is suggested to focus on the neutron-structure interaction, that leads to internal heat generation, with special emphasis on the use of different materials. Furthermore, a study on the manufacturing process of the mirrors should be considered as it may define the cooling channel geometry and the material used.

Additionally, from a structural point of view, one should contemplate the thermal gradient imposed in the launcher mirror due to the microwave beam as well as the dead weight and the effect that an earthquake may induce on the mirrors.

References

- [1] Song, Y., Wu, W., & Du, S. (2014). *Tokamak Engineering Mechanics*. Springer Berlin Heidelberg.
- [2] International Energy Agency. (2016). *Key World Energy Statistics*. International Energy Agency.
- [3] Weisz, P. B. (2004). Basic choices and constraints on long-term energy supplies. *Physics Today*, 57(7), 47-52.
- [4] Wesson, J. (1987). *Tokamaks*. Oxford: Clarendon Press.
- [5] Iter. (2017). *The Iter Organization*. Accessed on 02nd March 2017 at: <https://www.iter.org/org>.
- [6] Iter. (2017). *What is Iter?*. Accessed on 02nd March 2017 at: <https://www.iter.org/proj/inafewlines>.
- [7] Iter. (2017). *Disgnostics*. Accessed on 06nd March 2017 at: <https://www.iter.org/mach/diagnostics>.
- [8] Dulon, K. (2009). *Tracking The Fast Ion*. Accessed on 07nd March 2017 at: <https://www.iter.org/newsline/102/1396>.
- [9] Korsholm, S. B. (2016). *CTS System Design Description Document. F4E_D_33NQC3 (Project Report)*.
- [10] Moseev, D., Korsholm, S. B., Meo, F. (2011). *Fast Ion Dynamics in ASDEX Upgrade and TEXTOR Measured by Collective Thomson Scattering*. Technical University of Denmark, Association Euratom-Risø National Laboratory for Sustainable Energy, Denmark.
- [11] Korsholm, S. B., Bindslev, H., Furtula, V., Leipold, F., Meo, F., Michelsen, P. K., & Stejner, M. (2010). Collective Thomson scattering capabilities to diagnose fusion plasmas. *Nuclear Instruments and Methods in Physics Research Section A: Accelerators, Spectrometers, Detectors and Associated Equipment*, 623(2), 677-680.
- [12] Cheng, K. C., & Fujii, T. (1998). Heat in history Isaac Newton and Heat Transfer. *Heat Transfer Engineering*, 19(4), 9-21.
- [13] Narasimhan, T. N. (1999). Fourier's heat conduction equation: History, influence, and connections. *Reviews of Geophysics*, 37(1), 151-172.
- [14] Bergman, T. L., & Incropera, F. P. (2011). *Fundamentals of Heat and Mass Transfer*. John Wiley & Sons.
- [15] White, F. (2010). *Fluid Mechanics*. McGraw-Hill: New York.

- [16] Korsholm, S. B. (2017). *Deliverable D09 Low Field Side Collective Thomson Scattering – Load Specification*. F4E-FPA-393 SG04 (Project Report).
- [17] Huang, H. C., & Usmani, A. S. (1994). *Finite Element Analysis for Heat Transfer: Theory and Software*. Springer: Verlag.
- [18] ANSYS, B. (2013). ANSYS mechanical APDL theory reference. *Documentation for Ansys*.
- [19] Santos, R., Policarpo, H., Gonçalves, B., Varela, P., Nonb, E., Klinkby, E., & Vaz, P. (2015, April). Material assessment for ITER's collective Thomson Scattering first mirror. In *Advancements in Nuclear Instrumentation Measurement Methods and their Applications (ANIMMA), 2015 4th International Conference on* (pp. 1-4). IEEE.
- [20] McKinney G.W., Brown F. B., et al. MCNP 6.1.1 new features demonstrated. IEEE 2014 Nuclear Science Symposium, Seattle, 8-15 November 2014, LA-UR-14-23108.
- [21] Cook, R. D., Malkus, D. S., Plesha, M. E., & Witt, R. J. (1974). *Concepts and Applications of Finite Element Analysis* (Vol. 4). New York: Wiley.
- [22] Nikishkov, G. P. (2004). *Introduction to the Finite Element Method*. University of Aizu, Japan.
- [23] ANSYS, Inc. (2012). Ansys Mechanical APDL Element Reference. *Documentation for Ansys*.
- [24] Brederode, V. D. (2015). *Aerodinâmica Incompressível: Fundamentos*. IST: Lisboa.
- [25] Icepak, A. N. S. Y. S. (2013). ANSYS Icepak User's Guide. *ANSYS Inc*.
- [26] Fluent, A. N. S. Y. S. (2013). ANSYS Fluent User's Guide. *ANSYS Inc*.
- [27] Vajjha, R. S., Das, D. K., & Ray, D. R. (2015). Development of new correlations for the Nusselt number and the friction factor under turbulent flow of nanofluids in flat tubes. *International Journal of Heat and Mass Transfer*, 80, 353-367.
- [28] Saysroy, A., & Eiamsa-ard, S. (2017). Periodically fully-developed heat and fluid flow behaviors in a turbulent tube flow with square-cut twisted tape inserts. *Applied Thermal Engineering*, 112, 895-910.
- [29] Oliveira, L. A., & Lopes, A. G. (2012). *Mecânica dos Fluidos*. Lidel: Lisboa.
- [30] Quental, P. B., Policarpo, H., Luís, R., & Varela, P. (2016). Thermal analysis of the in-vessel components of the ITER plasma-position reflectometry. *Review of Scientific Instruments*, 87(11), 11E720.
- [31] Silva, A., Policarpo, H., & Varela, P. (2016). *Assessment of stray-radiation protection needs for the PPR in-vessel components*. F4E_D_24LLE8 (Project Report).

- [32] Van Osch, E. V., Horsten, M. G., & De Vries, M. I. (1998). Irradiation testing of 316L (N)-IG austenitic stainless steel for ITER. *Journal of Nuclear Materials*, 258, 301-307.
- [33] Luís, R., R. Moutinho, L. Prior, P. B. Quental, A. Lopes, H. Policarpo, N. Velez, A. Vale, A. Silva, A. Malaquias. (2017). *Nuclear and Thermal Analysis of a Reflectometry Diagnostics Concept for Demo*. Submitted to *IEEE Transactions on Plasma Science*.
- [34] Moran, M. J., Shapiro, H. N., Boettner, D. D., & Bailey, M. B. (2010). *Fundamentals of Engineering Thermodynamics*. John Wiley & Sons.
- [35] Qinqsheng, H. (2016). *Mass Flow Allotment for EQ12 Proposed by PI*. ITER_D_U3HUCQ (Project Report).
- [36] CES Edupak 2013 [CD-ROM]. Granta Design Limited, 2013.
- [37] Davis, J. W., & Barabash, V. (2011). *Iter Material Properties Handbook*. ITER-AM01-3111.
- [38] Optotherm Thermal Imaging (2017). Emissivity in the Infrared: Emissivity Values. Accessed on 25th April 2017 at: <http://www.optotherm.com/emiss-table.htm>.
- [39] Barabash V. (2013). *Appendix A, Materials Design Limit Data*. ITER_D_222RLN (Project Report).
- [40] ITER Material Properties Handbook. ITER-AK01-3202.

Appendixes

A.1. MATLAB® Routine A1

The calculations, related to the microwave radiation from the gyrotron incident on the launcher mirror with a distribution expressed by equation (40), of the shape of the isolines and the power between each one, are conducted using the following MATLAB® routine:

```
function [X,Y,Z,T] = isolinhas_function(Ptot,wx,wy,xmax,ymax,N)
pace=0.001;
x=-xmax:pace:xmax;
racao=xmax/ymax;
y=x./racao;
[X,Y] = meshgrid(x,y);
Z=Ptot*(2/(pi*wx*wy)).*exp(-2*((X/wx).^2+(Y/wy).^2));
[C,h]=contour(X,Y,Z,N,'ShowText','on');
set(gcf,'Visible','off')
tamanho=length(C(1,:));
CC=C;
for j=1:N
    MAX(1,j)=max(CC(1,:));
    index= find(CC(1,:)==MAX(1,j),1);
    MAX(2,j)=index;
    CC(1,index:end)=0;
end
MAX2=[0:length(C)];
MAX=[MAX2 MAX];
clear CC MAX2
ab=zeros(7,N+1);
for i=1:length(MAX)-1
    limite_inf=MAX(2,i+1)+1;
    limite_sup=MAX(2,i)-1;
    ab(1,i)=max(C(1,limite_inf:limite_sup));
    ab(2,i)=max(C(2,limite_inf:limite_sup));
end
ab(1,i+1)=xmax;
ab(2,i+1)=ymax;
fun = @(x,y) Ptot*(2/(pi*wx*wy)).*exp(-2*((x/wx).^2+(y/wy).^2));
for i=1:length(ab(1,:))
    ab(3,i)=4*(integral2(fun,0,ab(1,i),0,ab(2,i)));
end
ab(4,1)=ab(3,1);
for i=2:length(ab(1,:))
    ab(4,i)=ab(3,i)-ab(3,i-1);
end
ab(5,:)=100*(ab(4,:)/ab(3,length(ab(1,:)))));
ab(6,:)=100*(ab(4,:)/Ptot);
ab(7,:)=100*(ab(5,:)-ab(6,:));
[m,n]=size(ab);
Isolinhas=(1:n)';
a=10^3*round(ab(1,:),3)';
b=10^3*round(ab(2,:),3)';
Potencia=10^-6*round(ab(4,:),3)';
T=table(Isolinhas,a,b,Potencia);
End
```


A.2. Data for Microwave Power Absorbed Fraction Calculation

This appendix contains data for the calculation of microwave power absorbed fraction calculation presented in [39], [40].

Table 22 - Data for equation (41).

$Z_0 (\Omega)$	$f(\text{GHz})$	$\mu_0 \left(\frac{\Omega s}{m}\right)$
376.73	60.00	1.26E-6

Table 23 - Electrical Resistivity for SS316L(N)-IG.

$T, ^\circ\text{C}$	20	50	100	150	200	250
$\rho, \mu\Omega * cm$	75.00	76	80	83	87	90
$T, ^\circ\text{C}$	300	350	400	450	500	550
$\rho, \mu\Omega * cm$	94	97	100	103	106	109
$T, ^\circ\text{C}$	600	650	700	1127	1227	1371
$\rho, \mu\Omega * cm$	112	114	116	126.8	129.2	132.2

Table 24- Electrical Resistivity for tungsten.

$T, ^\circ\text{C}$	20	27	227	427	627	827
$\rho, \mu\Omega * cm$	5.5	5.6	10	15	21	27
$T, ^\circ\text{C}$	1000	1027	1227	1500	1527	2000
$\rho, \mu\Omega * cm$	33	33	40	48	51	66
$T, ^\circ\text{C}$	2500	3000				
$\rho, \mu\Omega * cm$	84	105				

Table 25 - Electrical Resistivity for copper.

$T, ^\circ\text{C}$	20	50	100	150	200	250
$\rho, \mu\Omega * cm$	1.68	1.88	2.21	2.55	2.89	3.23
$T, ^\circ\text{C}$	300	350	400	450	500	550
$\rho, \mu\Omega * cm$	3.58	3.93	4.29	4.65	5.01	5.38
$T, ^\circ\text{C}$	600	650	700	900	950	1000
$\rho, \mu\Omega * cm$	5.76	6.15	6.55	8.23	8.68	9.14

A.3. SS316 L(N)-IG Properties

This appendix contains information regarding the material properties of TYPE 316L(N)-IG Stainless Steel and their variations with temperature presented in [39].

Table 26 - Values of thermal conductivity, specific heat, density and thermal conductivity and diffusivity from room temperature to 800 °C for type 316L(N)-IG stainless steel.

SS316L(N)-IG				
T (°C)	Specific Heat (J/(KgK))	k W/(mK)	Density (Kg/m3)	Thermal Diffusivity (m2/s)
20.00	470.00	13.94	7966.00	3.72327E-06
50.00	476.00	14.37	7949.00	3.79785E-06
100.00	486.00	15.08	7932.00	3.91185E-06
150.00	497.00	15.80	7910.00	4.01906E-06
200.00	508.00	16.52	7889.00	4.12216E-06
250.00	518.00	17.24	7867.00	4.23056E-06
300.00	529.00	17.95	7846.00	4.32474E-06
350.00	539.00	18.67	7824.00	4.42718E-06
400.00	550.00	19.39	7803.00	4.51808E-06
450.00	560.00	20.10	7781.00	4.61288E-06
500.00	571.00	20.82	7760.00	4.69876E-06
550.00	582.00	21.54	7739.00	4.78231E-06
600.00	592.00	22.25	7717.00	4.87035E-06
650.00	603.00	22.97	7696.00	4.9497E-06
700.00	613.00	23.69	7674.00	5.03597E-06
800.00	634.00	25.12	7624.00	5.19694E-06

A.4. Copper Properties

This appendix contains information regarding the material properties of pure copper and their variations with temperature presented in [39].

Table 27 - Values of thermal conductivity, specific heat, density and thermal conductivity and diffusivity from room temperature to 800 °C for pure copper.

Copper				
T (°C)	Specific Heat (J/(KgK))	k W/(mK)	Density (Kg/m3)	Thermal Diffusivity (m2/s)
20.00	388.00	401.00	8940.00	0.000115605
50.00	390.00	398.00	8926.00	0.00011433
100.00	394.00	395.00	8903.00	0.000112607
150.00	398.00	391.00	8879.00	0.000110644
200.00	401.00	388.00	8854.00	0.000109282
250.00	406.00	384.00	8829.00	0.000107126
300.00	410.00	381.00	8802.00	0.000105575
350.00	415.00	378.00	8774.00	0.000103812
400.00	419.00	374.00	8744.00	0.000102082
450.00	424.00	371.00	8713.00	0.000100425
500.00	430.00	367.00	8681.00	9.83168E-05
550.00	435.00	364.00	8647.00	9.67713E-05
600.00	441.00	360.00	8612.00	9.47894E-05
650.00	447.00	357.00	8575.00	9.31379E-05
700.00	453.00	354.00	8536.00	9.15484E-05
750.00	459.00	350.00	8495.00	8.97619E-05
800.00	466.00	347.00	8453.00	8.80912E-05

A.5. Tungsten Properties

This appendix contains information regarding the material properties of tungsten and their variations with temperature presented in [39].

Table 28 - Values of thermal conductivity, specific heat, density and thermal conductivity and diffusivity from room temperature to 800 °C for tungsten.

Tungsten				
T (°C)	Specific Heat (J/(KgK))	k W/(mK)	Density (Kg/m3)	Thermal Diffusivity (m2/s)
20.00	128.96	172.81	19297.93	6.94389E-05
50.00	129.94	169.72	19290.75	6.77072E-05
100.00	131.55	164.75	19278.69	6.496E-05
150.00	133.15	160.02	19266.52	6.23784E-05
200.00	134.73	155.53	19254.23	5.99533E-05
250.00	136.29	151.26	19241.83	5.76764E-05
300.00	137.84	147.21	19229.32	5.55396E-05
350.00	139.37	143.38	19216.70	5.35355E-05
400.00	140.88	139.76	19203.96	5.16569E-05
450.00	142.38	136.34	19191.12	4.98972E-05
500.00	143.85	133.11	19178.16	4.825E-05
550.00	145.31	130.08	19165.09	4.67093E-05
600.00	146.76	127.24	19151.90	4.52694E-05
650.00	148.19	124.57	19138.61	4.3925E-05
700.00	149.60	122.08	19125.20	4.26708E-05
750.00	150.99	119.76	19111.68	4.15021E-05
800.00	152.36	117.60	19098.05	4.04141E-05

Table 29 - Emissivity values for tungsten.

T, K	300	400	500	600	700	800	900
ϵ	0.0104	0.0276	0.0443	0.0607	0.0767	0.0923	0.1075
T, K	800	900	1000	1100	1200	1300	1400
ϵ	0.1223	0.1367	0.1508	0.1644	0.1776	0.1905	0.2030
T, K	1500	1600	1700	1800	1900	2000	2100
ϵ	0.2150	0.2267	0.2380	0.2489	0.2594	0.2696	0.2793
T, K	2200	2300	2400	2500	2600	2700	2800
ϵ	0.2886	0.2976	0.3061	0.3143	0.3221	0.3295	0.3365

A.6. Launcher cooling channel geometries

In this appendix are presented the launcher cooling channels geometries in more detail. Namely, cross sectional views and dimensions.

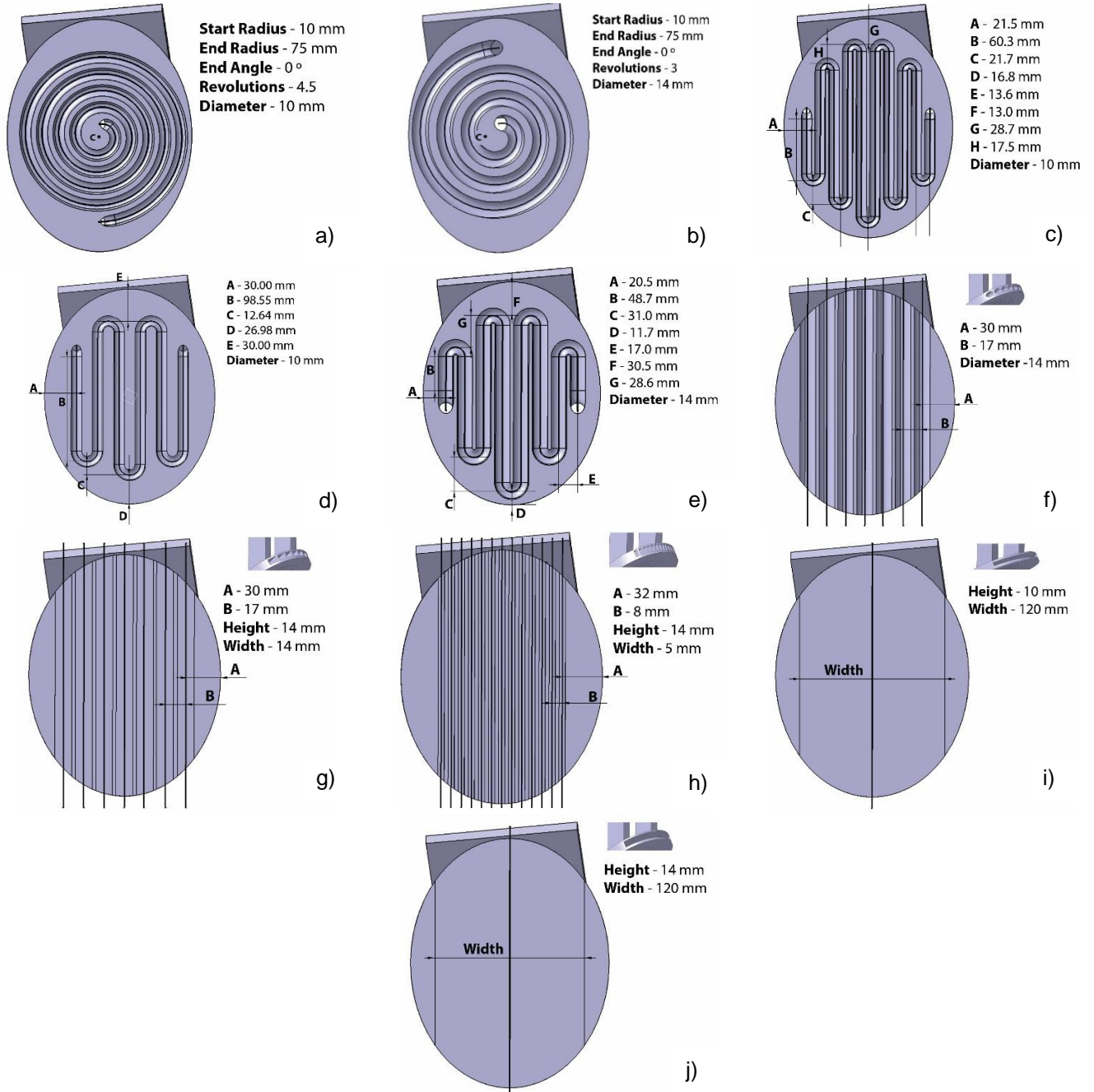


Figure 67 - Launcher mirror cooling channel geometries: a) SPIRAL_D_10MM; b) SPIRAL_D_14MM; c) ZIGZAG_D_10MM; d) ZIGZAG_D_10MM_CURTO; e) ZIGZAG_D_14MM; f) 7_D_14MM; g) 7_14X14; h) 13_14X5; i) 1_RETAN_120X10 and; j) 1_RETAN_120X14.

A.7. Receiver cooling channel geometries

In this appendix are presented the receiver cooling channels geometries in more detail. Namely, cross sectional views and dimensions.

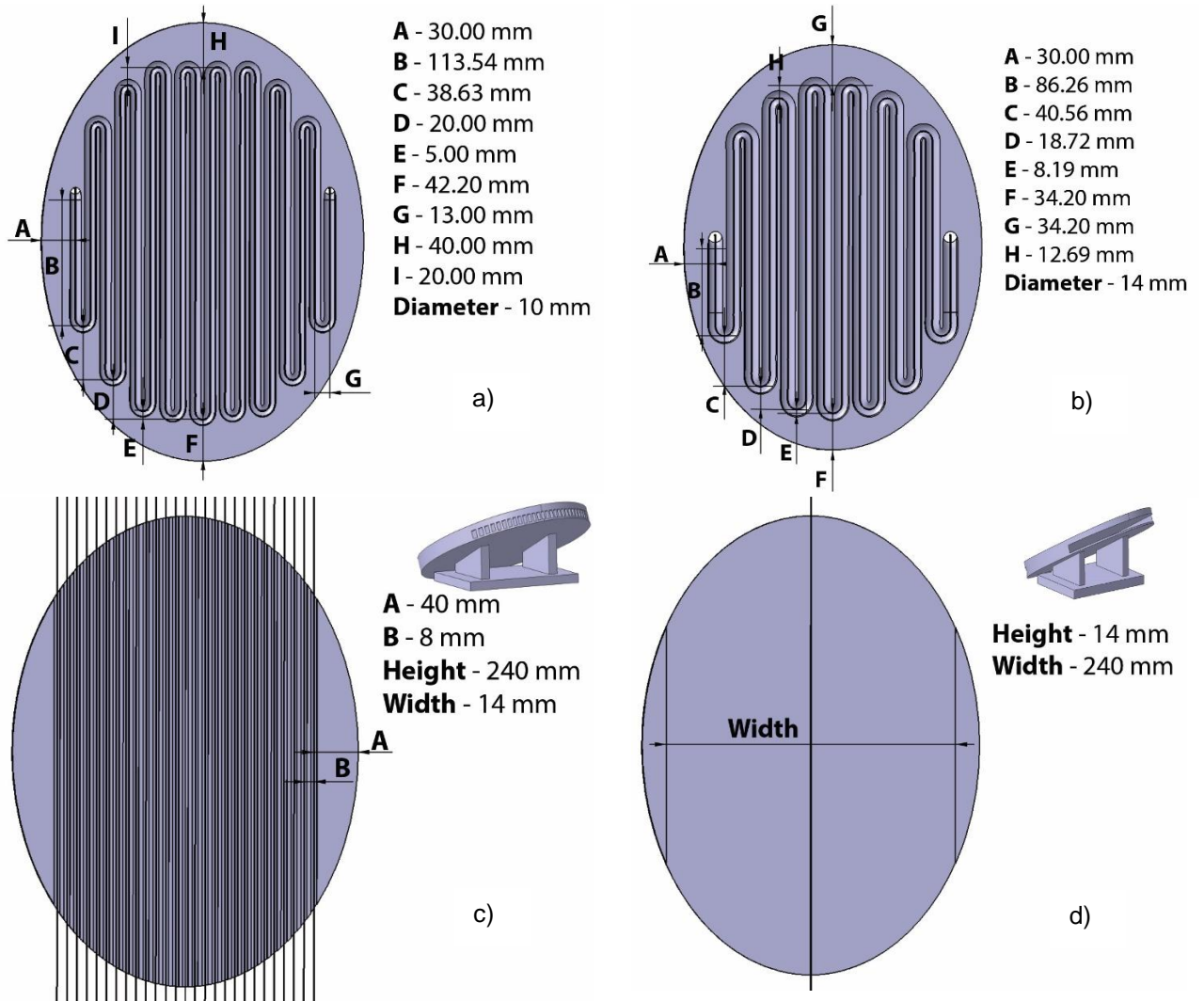


Figure 68 - Receiver mirror cooling channel geometries: a) ZIGZAG_D_10MM; b) ZIGZAG_D_14MM; c) 13_14X5 and; d) 1_RETAN_240X14.

A.8. SS316 L(N)-IG Launcher Mirror Results

Table 30 - Mesh convergence for SS316L(N)-IG.

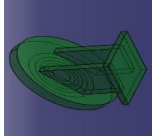
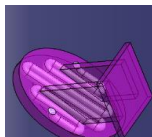
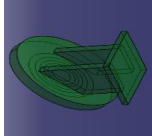
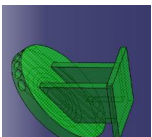
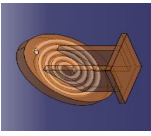
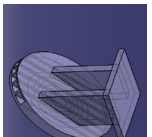
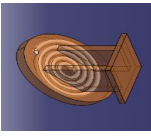
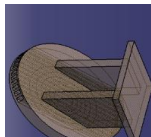
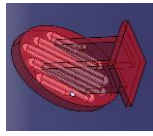
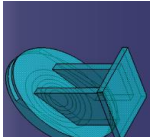
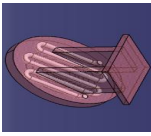

Description	Geometry	Mesh Size [mm]	Mass Flow Rate [kg/s]	Convection Coef [W/(m²·K)]	Mirror		Water		Description	Geometry	Mesh Size [mm]	Mass Flow Rate [kg/s]	Convection Coef [W/(m²·K)]	Max Mirror Temperature [°C]	
					Min Temperature [°C]	Max Temperature [°C]	Min Temperature [°C]	Max Temperature [°C]							
Solid Geometry (Microwaves)		0.015	N/A	N/A	150.00	1762.70	N/A	N/A	Channel_ZIGZAG_D_14MM		0.0040	1.5000	44043.0000	459.9797	
		0.004			150.00	1763.70					N/A			N/A	N/A
		0.003			150.00	1764.70					N/A			N/A	N/A
		0.0025			150.00	1765.70					N/A			N/A	N/A
		0.005			150.00	886.51					N/A			N/A	N/A
Solid Geometry (Radiation)		0.004	N/A	N/A	150.00	885.34	N/A	N/A	Channel_Z_D_14 MM		0.0030	0.2140	9285.330	522.8565	
		0.003			150.00	885.36					N/A			N/A	N/A
		0.0025			150.00	887.25					N/A			N/A	N/A
		0.005			150.00	2306.06					N/A			N/A	N/A
		0.004			150.00	2305.28					N/A			N/A	N/A
Solid Geometry (Mk)		0.0025	N/A	N/A	150.00	2306.56	N/A	N/A	Channel_7_14X14		0.0025	0.1150	17967.0800	425.6976	
		0.003			150.00	2306.52					N/A			N/A	N/A
		0.004			150.00	694.0121					70.0000			71.2796	424.4612
		0.0030			70.8816	694.1835					70.0000			71.2783	642.3361
		0.0025			70.8827	693.0796					70.0000			71.2786	636.5922
Channel_SPIRAL_D_10MM		0.0020	1.5000	80706.0861	70.8600	693.1839	70.0000	71.2788	Channel_13_14X5		0.0020	0.1150	15427.0975	637.2913	
		0.0040			70.2783	687.4296	70.0000	71.2850			380.9843				
		0.0030			70.5133	697.1170	70.0000	71.2847			380.5440				
		0.0025			70.3109	688.2677	70.0000	71.2848			380.8047				
		0.0020			70.5015	685.6782	70.0000	71.2856			380.7603				
Channel_ZIGZAG_D_10MM		0.0040	1.5000	80706.0900	69.5470	524.6833	70.0000	71.2770	Channel_1_120X10		0.0040	1.5000	26768.5000	480.8150	
		0.0030			68.8038	521.4188	70.0000	71.2759			480.4262				
		0.0025			N/A	N/A	N/A	N/A			479.6054				
		0.0020			70.1139	521.5562	70.0000	71.2756			479.7773				
		0.0040			70.4116	603.7681	70.0000	71.2913							
Channel_ZIGZAG_D_10MM_CURTO		0.0030	1.5000	80706.0900	70.4647	605.3480	70.0000	71.2920	Channel_1_120X10		0.0030	1.5000	26768.5000	480.4262	
		0.0025			70.6595	603.7256	70.0000	71.2911			479.6054				
		0.0020			70.4770	603.5156	70.0000	71.2915			479.7773				
		0.0040			70.4116	603.7681	70.0000	71.2913							
		0.0030			70.4647	605.3480	70.0000	71.2920							

Table 31- Flow variation results for SS316L(N)-IG.

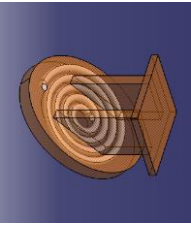
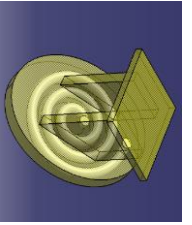
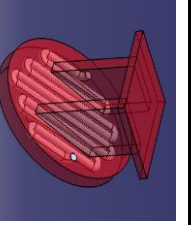
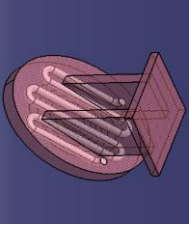
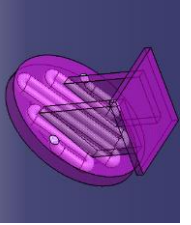
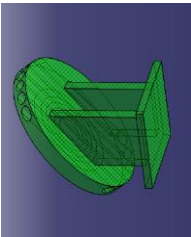
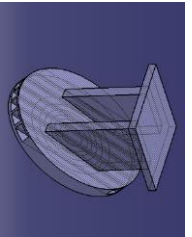
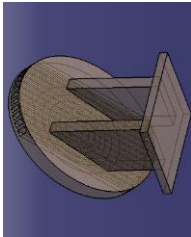
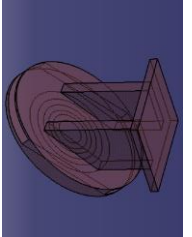
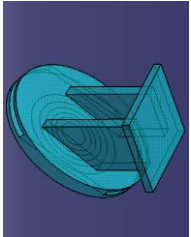
Description	Geometry	Mesh Size [m]	Mass Flow Rate [kg/s]	Convection Coef [W/(m²K)]	Flow Variation		Water	
					Mirror		Min Temperature [°C]	Max Temperature [°C]
					Min Temperature [°C]	Max Temperature [°C]	Min Temperature [°C]	Max Temperature [°C]
SPIRAL_D_10MM		0.0025	1.500	80706	70.283	693.258	70.000	71.278
			1.000	58349	70.404	696.521	70.000	71.918
			0.500	33513	70.800	704.933	70.000	73.834
			0.250	19248	71.713	719.697	70.000	77.662
SPIRAL_D_14MM		0.0025	1.500	44043	70.304	685.940	70.000	71.265
			1.000	31842	70.441	691.461	70.000	71.897
			0.500	18289	71.019	705.501	70.000	73.792
			0.250	10504	72.548	729.377	70.000	77.576
ZIGZAG_D_10MM		0.0025	1.500	80706	70.117	521.542	70.000	71.276
			1.000	58349	70.173	526.264	70.000	71.914
			0.500	33513	70.349	538.457	70.000	73.827
			0.250	19248	70.759	559.505	70.000	77.652
ZIGZAG_D_10MM_CURTO		0.0025	1.500	80706	70.468	604.274	70.000	71.291
			1.000	58349	70.673	608.190	70.000	71.936
			0.500	33513	71.315	620.138	70.000	73.871
			0.250	19248	72.575	639.694	70.000	77.737
ZIGZAG_D_14MM		0.0025	1.500	44043	63.844	442.752	70.000	71.283
			1.000	31842	70.191	462.156	70.000	71.883
			0.500	18289	70.446	483.659	70.000	73.764
			0.250	10504	71.018	518.607	70.000	77.522

Table 32- Flow variation results for SS316L(N)-IG (continuation).

Description	Geometry	Mesh Size [m]	Mass Flow Rate [kg/s]	Convection Coef [W/(m ² *K)]	Flow Variation (continuation)			
					Mirror		Water	
					Min Temperature [°C]	Max Temperature [°C]	Min Temperature [°C]	Max Temperature [°C]
7_D_14MM		0.0025	0.214	9285	71.234	520.919	70.000	72.005
			0.143	6713	71.872	553.149	70.000	72.985
			0.071	3856	73.863	636.738	70.000	75.928
			0.036	2215	77.924	778.493	70.000	81.438
7_14X14		0.0025	0.214	9285	70.487	425.460	70.000	71.628
			0.143	6713	70.726	466.179	70.000	72.421
			0.071	3856	71.520	566.139	70.000	74.800
			0.036	2215	73.311	709.848	70.000	79.252
13_14X5		0.0025	0.115	17967	69.978	639.278	70.000	72.527
			0.077	12990	70.388	671.758	70.000	73.759
			0.038	7461	70.758	752.132	70.000	77.528
			0.019	4285	71.597	877.684	70.000	84.794
1_RETAN_120X14		0.0025	1.500	15427	70.595	381.001	70.000	71.182
			1.000	11154	70.920	408.359	70.000	71.773
			0.500	6406	71.793	482.571	70.000	73.542
			0.250	3679	73.126	611.317	70.000	77.074
1_RETAN_120X10		0.0025	1.500	26769	70.338	479.543	70.000	71.223
			1.000	19353	70.499	493.585	70.000	71.835
			0.500	11115	71.109	531.241	70.000	73.667
			0.250	6384	72.632	596.874	70.000	77.327

A.9. Copper Launcher Mirror Results

Table 33 - Mesh convergence for copper.

Description	Geometry	Convergence				Max Mirror Temperature [°C]	Description	Geometry	Convergence (continuation)				Max Mirror Temperature [°C]
		Mesh Size [mm]	Mass Flow Rate [kg/s]	Convection Coef [W/(m²·K)]	Temperature [°C]				Mesh Size [mm]	Mass Flow Rate [kg/s]	Convection Coef [W/(m²·K)]	Temperature [°C]	
Solid Geometry (Microwaves)		0.005	N/A	N/A	958.95	ZIGZAG_D_14MM		0.0050	1.5000	44043.0000	N/A	151.0566	
		0.004			958.52			0.0040			151.0374		
		0.003			958.78			0.0030			N/A		
		0.0025			958.06			0.0025			N/A		
		0.005			405.22			0.0050			156.0688		
Solid Geometry (Radiation)		0.004	N/A	N/A	405.42	7_D_14MM		0.0040	0.2140	9285.3300	156.2353		
		0.003			405.56			0.0030			156.1862		
		0.0025			405.61			0.0025			156.2502		
		0.005			976.76			0.0050			151.1319		
		0.004			977.08			0.0040			151.1850		
Solid Geometry (Mik)		0.003	N/A	N/A	977.35	7_14X14		0.0030	0.2140	9285.3300	151.2214		
		0.0025			977.52			0.0025			151.1794		
		0.0050			151.0653			0.0050			155.8414		
		0.0040			151.0234			0.0040			156.1090		
		0.0030			151.0269			0.0030			155.8785		
SPRAL_D_10MM		0.0025	1.5000	80706.0861	151.0514	13_14X5		0.0025	0.1150	17967.0800	156.2844		
		0.0050			N/A			0.0050			155.3864		
		0.0040			150.8512			0.0040			155.3894		
		0.0030			150.8512			0.0030			155.3488		
		0.0025			150.8457			0.0025			155.3337		
SPRAL_D_14MM		0.0040	1.5000	44042.8900	151.0754	1_RETAN_120X14		0.0050	1.5000	15427.0975	151.1805		
		0.0030			151.0475			0.0040			151.1758		
		0.0025			N/A			0.0030			151.1446		
		0.0020			151.0832			0.0025			151.1863		
		0.0050			151.0818			0.0050			151.1863		
ZIGZAG_D_10MM_CURTO		0.0040	1.5000	80706.0900	151.0395	1_RETAN_120X10		0.0040	1.5000	26768.5000	151.1758		
		0.0030			151.0752			0.0030			151.1446		
		0.0025			151.0694			0.0025			151.1863		
		0.0050			151.0818			0.0050			151.1863		
		0.0040			151.0395			0.0040			151.1758		

Table 34 - Flow variation results for copper.

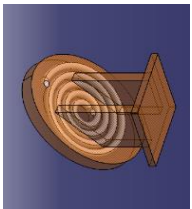
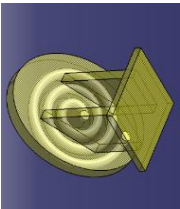
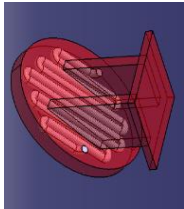
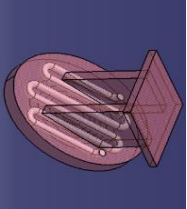
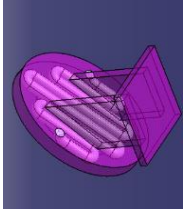
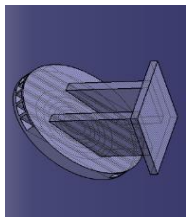
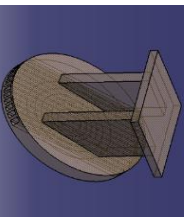
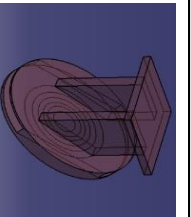
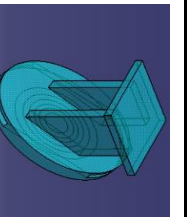
Description	Geometry	Mesh Size [m]	Mass Flow Rate [Kg/s]	Convection Coef [W/(m ² *K)]	Mittor			Water	
					Min Temperature [°C]	Max Temperature [°C]	Max reflective Surface Temperature [°C]	Min Temperature [°C]	Max Temperature [°C]
					Flow Variation				
SPRAL_D_10MM		0.0025	1.500	80706	71.531	151.046	111.650	70.000	71.390
			1.000	58349	72.434	151.054	115.120	70.000	72.081
			0.500	33513	75.102	151.043	123.410	70.000	74.145
			0.250	19248	80.454	151.046	135.830	70.000	78.219
SPRAL_D_14MM		0.0025	1.500	44043	72.062	150.863	117.990	70.000	71.372
			1.000	31842	73.161	150.866	123.740	70.000	72.052
			0.500	18289	76.605	150.874	134.400	70.000	74.072
			0.250	10504	83.815	157.657	157.610	70.000	78.043
ZIGZAG_D_10MM		0.0025	1.500	80706	70.489	151.049	104.030	70.000	71.388
			1.000	58349	70.841	151.053	108.160	70.000	72.079
			0.500	33513	72.067	151.071	117.840	70.000	74.141
			0.250	19248	74.894	151.070	131.990	70.000	78.225
ZIGZAG_D_10MM_CURTO		0.0025	1.500	80706	71.147	151.051	108.870	70.000	71.402
			1.000	58349	71.863	151.043	113.180	70.000	72.098
			0.500	33513	74.250	151.037	123.430	70.000	74.174
			0.250	19248	79.499	151.088	138.850	70.000	78.263
ZIGZAG_D_14MM		0.0025	1.500	44043	71.390	151.080	108.500	70.000	71.364
			1.000	31842	72.042	151.062	115.290	70.000	71.786
			0.500	18289	74.060	151.073	131.040	70.000	74.299
			0.250	10504	78.037	153.024	153.024	70.000	79.793

Table 35 - Flow variation results for copper (continuation).

Description	Geometry	Mesh Size [m]	Mass Flow Rate [kg/s]	Convection Coef [W/(m ² K)]	Mirror			Water	
					Min Temperature [°C]	Max Temperature [°C]	Max reflective Surface Temperature [°C]	Min Temperature [°C]	Max Temperature [°C]
7_D_14MM		0.0025	0.214	9285	73.383	156.246	156.246	70.000	71.791
			0.143	6713	75.563	172.026	172.026	70.000	72.606
			0.071	3856	83.268	205.524	205.524	70.000	74.959
			0.036	2215	100.837	249.734	249.734	70.000	79.144
7_14X14		0.0025	0.214	9285	71.723	151.171	145.940	70.000	71.469
			0.143	6713	72.805	159.411	159.411	70.000	72.158
			0.071	3856	76.761	187.558	187.558	70.000	74.181
			0.036	2215	86.413	224.239	224.239	70.000	77.851
13_14X5		0.0025	0.115	17967	70.682	155.843	155.843	70.000	72.289
			0.077	12990	71.057	168.701	168.701	70.000	73.343
			0.038	7461	72.303	195.260	195.260	70.000	76.460
			0.019	4285	75.334	229.640	229.640	70.000	82.182
1_RETAN_120X14		0.0025	1.500	15427	70.774	155.334	155.334	70.000	71.280
			1.000	11154	71.104	178.997	178.997	70.000	71.912
			0.500	6406	72.142	233.724	233.724	70.000	73.791
			0.250	3679	74.767	310.179	310.179	70.000	77.479
1_RETAN_120X10		0.0025	1.500	26769	70.685	151.189	129.660	70.000	71.327
			1.000	19353	70.970	151.191	143.390	70.000	71.986
			0.500	11115	71.831	175.617	175.617	70.000	73.948
			0.250	6384	73.827	221.599	221.599	70.000	77.817

A.10. Tungsten Launcher Mirror Results

Table 36 - Mesh convergence for tungsten.

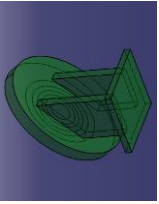
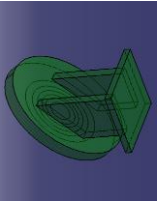
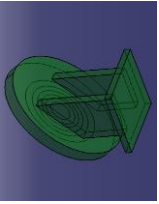
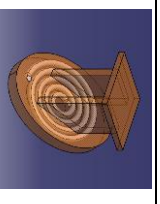
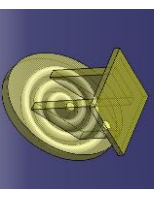
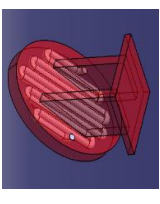
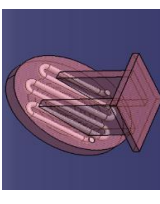
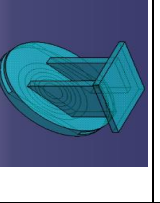
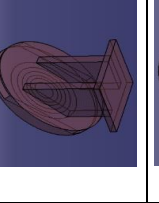
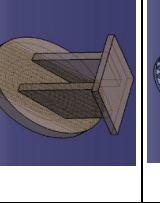
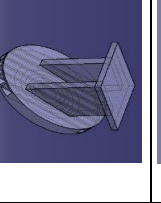
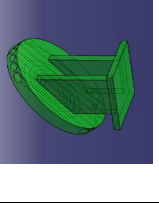
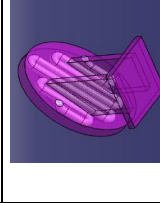
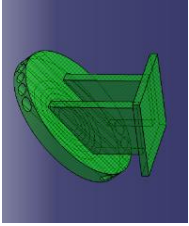
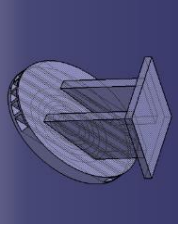
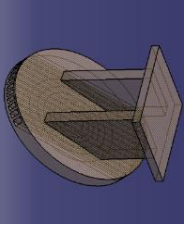
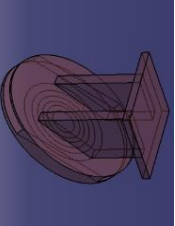
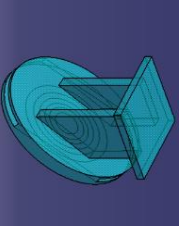
Description	Geometry	Convergence				Max Mirror Temperature [°C]
		Mesh Size [mm]	Mass Flow Rate [kg/s]	Convection Coef [W/(m ² K)]	Temperature [°C]	
Solid Geometry (Microwaves)		0.005	N/A	N/A	3653.02	
		0.004			3656.97	
		0.003			3659.32	
		0.0025			3660.09	
		0.005			781.87	
Solid Geometry (Radiation)		0.004	N/A	N/A	781.87	
		0.003			781.87	
		0.0025			781.87	
		0.005			1610.92	
		0.004			1609.83	
Solid Geometry (Mix)		0.003	N/A	N/A	1608.77	
		0.0025			1608.55	
		0.0050			156.1981	
		0.0040			155.7128	
		0.0030			155.8233	
SPIRAL_D_10MM		0.0025	1.5000	80706.0961	155.8273	
		0.0050			N/A	
		0.0040			161.7861	
		0.0030			161.9176	
		0.0025			161.8663	
SPIRAL_D_14MM		0.0050	1.5000	44042.8900	151.2825	
		0.0040			151.2829	
		0.0030			151.2935	
		0.0020			151.2984	
		0.0050			151.4866	
ZIGZAG_D_10MM		0.0040	1.5000	80706.0900	151.4984	
		0.0030			151.5011	
		0.0025			151.5064	
		0.0050			151.2273	
		0.0040			157.1551	
ZIGZAG_D_10MM_CURTO		0.0030	1.5000	80706.0900	157.1633	
		0.0025			157.1775	
		0.0050			176.5070	
		0.0040			176.5330	
		0.0030			176.5094	
1_RETN_120X10		0.0050	1.5000	26768.5000	157.2273	
		0.0040			157.1551	
		0.0030			157.1633	
		0.0025			157.1775	
		0.0050			176.4805	
1_RETN_120X14		0.0050	1.5000	15427.0975	176.4805	
		0.0040			176.5330	
		0.0030			176.5094	
		0.0025			176.4805	
		0.0050			213.8389	
13_14X5		0.0050	0.1150	17967.0800	213.8389	
		0.0040			213.8788	
		0.0030			214.2423	
		0.0025			213.8389	
		0.0050			186.1520	
7_14X14		0.0050	0.2140	9285.3300	186.1520	
		0.0040			186.4652	
		0.0030			186.5668	
		0.0025			186.7037	
		0.0050			201.6229	
7_D_14MM		0.0050	0.2140	9285.3300	201.6229	
		0.0040			201.6884	
		0.0030			201.5518	
		0.0025			201.6229	
		0.0050			202.0026	
ZIGZAG_D_14MM		0.0050	1.5000	44043.0000	151.3060	
		0.0040			151.2938	
		0.0030			N/A	
		0.0025			N/A	
		0.0050			N/A	

Table 37 - Flow variation results for tungsten.


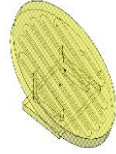
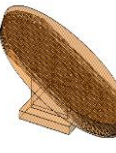

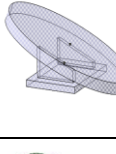




Description	Geometry	Mesh Size [m]	Mass Flow Rate [kg/s]	Convection Coef [W/(m ² *K)]	Flow Variation			Water	
					Min Temperature [°C]	Max Temperature [°C]	Max reflective Surface Temperature [°C]	Min Temperature [°C]	Max Temperature [°C]
SPIRAL_D_10MM		0.0025	1.500	80706	70.684	155.800	155.800	70.000	71.264
			1.000	58349	71.258	160.125	160.125	70.000	71.896
			0.500	33513	73.557	170.675	170.675	70.000	73.787
			0.250	19248	78.435	186.806	186.806	70.000	77.552
SPIRAL_D_14MM		0.0025	1.500	44043	71.355	161.874	161.874	70.000	71.249
			1.000	31842	72.454	168.933	168.933	70.000	71.872
			0.500	18289	74.993	186.291	186.291	70.000	73.734
			0.250	10504	80.313	212.758	212.758	70.000	77.437
ZIGZAG_D_10MM		0.0025	1.500	80706	70.247	151.298	134.110	70.000	71.262
			1.000	58349	70.423	151.411	139.370	70.000	71.892
			0.500	33513	71.078	152.119	152.119	70.000	73.780
			0.250	19248	72.701	171.310	171.310	70.000	77.545
ZIGZAG_D_10MM_CURTO		0.0025	1.500	80706	70.713	151.506	145.500	70.000	71.278
			1.000	58349	71.135	151.696	150.840	70.000	71.916
			0.500	33513	72.600	163.901	163.901	70.000	73.825
			0.250	19248	75.963	183.907	183.907	70.000	77.626
ZIGZAG_D_14MM		0.0025	1.500	44043	70.565	151.310	134.040	70.000	71.240
			1.000	31842	70.726	151.466	142.580	70.000	71.858
			0.500	18289	71.991	163.070	163.070	70.000	73.711
			0.250	10504	75.125	194.423	194.423	70.000	77.400

Table 38 - Flow variation results for tungsten (continuation).

Description	Geometry	Mesh Size [m]	Mass Flow Rate [kg/s]	Convection Coef [W/(m ² *K)]	Mirror			Water	
					Min Temperature [°C]	Max Temperature [°C]	Max reflective Surface Temperature [°C]	Min Temperature [°C]	Max Temperature [°C]
					Flow Variation (continuation)				
7_D_14MM		0.0025	0.214	9285	72.022	201.626	201.626	70.000	71.831
			0.143	6713	73.186	226.846	226.846	70.000	72.687
			0.071	3856	77.328	281.458	281.458	70.000	75.183
			0.036	2215	87.599	354.010	354.010	70.000	79.676
7_14X14		0.0025	0.214	9285	71.000	186.694	186.694	70.000	71.473
			0.143	6713	71.601	208.878	208.878	70.000	72.169
			0.071	3856	73.541	255.942	255.942	70.000	74.232
			0.036	2215	78.611	317.260	317.260	70.000	78.024
13_14X5		0.0025	0.115	17967	70.438	213.931	213.931	70.000	72.351
			0.077	12990	70.683	235.928	235.928	70.000	73.457
			0.038	7461	71.450	283.168	283.168	70.000	76.776
			0.019	4285	73.122	343.775	343.775	70.000	82.972
1_RETAN_120X14		0.0025	1.500	15427	70.596	176.842	176.842	70.000	71.165
			1.000	11154	70.827	205.851	205.851	70.000	71.745
			0.500	6406	71.460	278.076	278.076	70.000	73.482
			0.250	3679	72.687	389.273	389.273	70.000	76.942
1_RETAN_120X10		0.0025	1.500	26769	70.571	157.175	157.175	70.000	71.207
			1.000	19353	70.792	173.799	173.799	70.000	71.809
			0.500	11115	71.396	215.123	215.123	70.000	73.613
			0.250	6384	72.533	279.331	279.331	70.000	77.207

A.11. SS316 L(N)-IG Receiver Mirror Results

Table 39 - Convergence and Flow Variation results for SS316 L(N)-IG receiver mirror.

Description	Channel length [m]	Convection Area [m ²]	Volume [dm ³]	Geometry	Mesh Size [m]	Mass Flow Rate [Kg/s]	Convection Coef [W/(m ² *K)]	Flow Variation			
								Mirror		Water	
								Max Temperature [°C]	Min Temperature [°C]	Min Temperature [°C]	Max Temperature [°C]
ZIGZAG_D_10MM	4.6704	1.47E-01	2.78E-01		0.0025	1.5000	80706	371.9810	69.7019	70.0000	71.0928
								373.2176	69.7716	70.0000	71.6388
								376.5168	69.9820	70.0000	73.2756
								382.2114	70.4554	70.0000	76.5441
ZIGZAG_D_14MM	3.5377	1.56E-01	5.45E-01		0.0025	1.5000	44043	320.9232	69.9442	70.0000	70.9915
								322.3948	70.0957	70.0000	71.4862
								326.7535	70.3180	70.0000	72.9667
								333.9583	70.8475	70.0000	75.9148
27_14XS	9.1256	3.47E-01	6.39E-01		0.0025	0.0560	1003	234.9220	70.5620	70.0000	72.6354
								236.0702	70.8926	70.0000	73.8706
								244.3529	71.8252	70.0000	77.2499
								258.6184	73.7673	70.0000	84.4013
1_RETAN_240X14	0.3800	1.62E-01	1.28E+00		0.0025	1.5000	14007	235.0684	70.7891	70.0000	70.7138
								235.9071	71.1089	70.0000	71.0696
								238.0091	71.9593	70.0000	72.1323
								241.7285	73.5047	70.0000	74.2541
								Convergence			
Description	Channel length [m]	Convection Area [m ²]	Volume [dm ³]	Geometry	Mesh Size [mm]	Mass Flow Rate [Kg/s]	Convection Coef [W/m ² *K]	Mirror		Water	
								Max Temperature [°C]	Min Temperature [°C]	Min Temperature [°C]	Max Temperature [°C]
Solid Geometry	N/A	N/A	N/A		0.004	N/A	N/A	1064.13	150.00		
					0.003			1063.83	150.00	N/A	N/A
					0.0025			1063.80	150.00		
ZIGZAG_D_10MM	4.6704	1.47E-01	2.78E-01		0.004	1.5000	80706	371.9811	69.7024	70.0000	71.0921
					0.003			371.9808	69.7022	70.0000	71.0922
					0.0025			371.9810	69.7019	70.0000	71.0928
ZIGZAG_D_14MM	3.5377	1.56E-01	5.45E-01		0.004	1.5000	44043	320.5441	70.0744	70.0000	70.9881
					0.003			320.3704	69.9605	70.0000	70.9911
					0.0025			320.9232	69.9442	70.0000	70.9915
27_14XS	9.1256	3.47E-01	6.39E-01		0.004	0.0560	17967	234.8523	70.5682	70.0000	72.6278
					0.003			234.9350	70.5672	70.0000	72.6359
					0.0025			234.9220	70.5620	70.0000	72.6354
1_RETAN_240X14	0.3800	1.62E-01	1.28E+00		0.004	1.5000	15427	234.9299	70.7941	70.0000	70.7140
					0.003			235.1417	70.7766	70.0000	70.7138
					0.0025			235.0684	70.7891	70.0000	70.7138